

12-2017

Biophysics of DNA based Nanosystems Probed by Optical Nanoscopy

Jing Pan
Purdue University

Follow this and additional works at: https://docs.lib.purdue.edu/open_access_dissertations

Recommended Citation

Pan, Jing, "Biophysics of DNA based Nanosystems Probed by Optical Nanoscopy" (2017). *Open Access Dissertations*. 1612.
https://docs.lib.purdue.edu/open_access_dissertations/1612

This document has been made available through Purdue e-Pubs, a service of the Purdue University Libraries.
Please contact epubs@purdue.edu for additional information.

BIOPHYSICS OF DNA BASED NANOSYSTEMS
PROBED BY OPTICAL NANOSCOPY

A Dissertation

Submitted to the Faculty

of

Purdue University

by

Jing Pan

In Partial Fulfillment of the

Requirements for the Degree

of

Doctor of Philosophy

December 2017

Purdue University

West Lafayette, Indiana

THE PURDUE UNIVERSITY GRADUATE SCHOOL
STATEMENT OF DISSERTATION APPROVAL

Dr. Jong Hyun Choi, Chair

School of Mechanical Engineering

Dr. Chengde Mao

Department of Chemistry

Dr. Andrew Mugler

Department of Physics and Astronomy

Dr. Cagri A. Savran

School of Mechanical Engineering

Approved by:

Dr. Jay P. Gore

Head of Graduate Program

*I dedicate this thesis to my parents,
my wife Xiaoming, and my daughter Emma
for their unconditional love and support.*

ACKNOWLEDGMENTS

I would like to thank my advisor Prof. Jong Hyun Choi for his continuous support and guidance on my research. Choi lab offers the most up-to-date experimental facilities I could ask for. Prof. Choi not only taught me how to conduct experiments, but also shared his expertise on how to effectively collaborate with colleagues and how to become a successful researcher in my future career. I hope I could continue performing high quality research in my future as prof. Choi has taught me to. I would like to thank the Office of Naval Research and National Science Foundation for their financial support. I would also like to thank all other members in my academic committee for their insightful advice.

Besides my academic committee members, I thank my fellow labmates Dr. Haorong Chen, Dr. Tae-Gon Cha, Dr. Hanyu Zhang, Feiran Li, Yancheng Du and Luke Upton for their help during my research. They shared many of the insights in their respective fields, which greatly helped my project. Many of the discussions we had also led to new inspirations for my research.

Last but not least, I would like to thank my family for the continuous support throughout my PhD. My parents and my wife took most of the burdens raising my daughter and supporting my life. I couldn't have accomplished what I have now without their help.

TABLE OF CONTENTS

	Page
LIST OF TABLES	viii
LIST OF FIGURES	ix
ABBREVIATIONS	xxii
NOMENCLATURE	xxiii
ABSTRACT	xxiv
1. INTRODUCTION	1
1.1 DNA Nanosystems and Optical Nanomaterials	1
1.1.1 Dynamic DNA Nanotechnology and DNA Walkers	1
1.1.2 Characterization Techniques for DNA Nanosystems	6
1.1.2.1 Single Molecule Techniques	8
1.1.2.2 Super-resolution Microscopy	9
1.1.3 Nanomaterials with Unique Optical Properties	11
1.1.3.1 Photophysics of Carbon Nanotubes	11
1.1.3.2 Photophysics of Quantum Dot	14
1.2 Motivation	17
1.3 Scope of Study	18
1.3.1 Synthesis of DNA-based Nanosystems	18
1.3.2 Optical Nanoscopy	18
1.3.3 Biophysics of DNA Walkers	19
1.4 Organization	19
2. METHODS	20
2.1 Single-walled Carbon Nanotube Functionalization	20
2.1.1 Nanotube Solubilization	20
2.1.2 Length Fractionation by Molecular Crowding	21
2.2 DNA Assisted Nanocrystal Growth	21
2.3 Nanometric Characterization	23
2.3.1 AFM Imaging	23
2.3.2 Spectral Characterization	23
2.3.3 Fluorescence Imaging	25
3. PROBING MOLECULAR INTERACTIONS	28
3.1 Introduction	28
3.2 Scheme	30

	Page
3.3 Methods	32
3.3.1 Porphyrin Stock Preparation	32
3.3.2 Aptamer-SWCNTs Synthesis	32
3.3.3 Optical Measurements	33
3.3.4 Porphyrin Characterization	33
3.3.5 Porphyrin Mixture Quantification Procedure	34
3.3.6 Plasma Porphyrin Extraction Procedure	34
3.4 Results and Discussion	35
3.4.1 Optical Modulation of a-SWCNTs	35
3.4.2 Optical Transduction of Porphyrins	35
3.4.3 Quantification of Porphyrins from Mixture	40
3.4.4 Porphyrin Detection in Plasma	43
3.5 Conclusions	44
4. UNDERSTANDING DNAZYME WALKER KINETICS	46
4.1 Introduction	46
4.2 Scheme	47
4.2.1 Kinetic Model	47
4.2.2 Calculation of Reaction Rates	50
4.3 Methods	52
4.3.1 DNA Enzymes and RNA Substrates	52
4.3.2 Walker Synthesis	53
4.3.3 Flow Channel Assembly	55
4.3.4 Optical Platform	55
4.3.5 Calculation of Walker Step Length	58
4.3.6 Ensemble Single Turnover Rate Measurement	58
4.3.7 Photo-regulation	59
4.4 Results	60
4.4.1 Mechanistic Studies of Walker Translocation Kinetics	60
4.4.2 Photo-regulation of Walker Kinetics	66
4.5 Discussion	68
4.5.1 Catalytic DNA Enzyme Core	69
4.5.2 Recognition Arms	69
4.5.3 Environmental Effects	70
4.5.4 Motor Track	70
4.6 Conclusions	71
5. IMAGING STOCHASTIC WALKER BEHAVIOR	73
5.1 Introduction	73
5.2 Scheme and Methods	74
5.2.1 DNA/nanotube Walker System	74
5.2.2 Walker System Synthesis	77
5.2.3 Optical Platform	77

	Page
5.2.4 Walking Experiment Procedure	78
5.2.5 Subdiffraction Tracking of Walker	79
5.2.6 Subdiffraction Imaging of Nanotubes	82
5.2.7 Walker Data Analysis	82
5.2.8 Simulated Walking	83
5.3 Results	85
5.3.1 Visualizing Nanoscale Structure and Motion	85
5.3.2 Displacement and Velocity Distribution	88
5.4 Discussion	89
5.5 Conclusions	93
6. PROGRAMMING 2-D MOLECULAR TRANSPORT	95
6.1 Introduction	95
6.2 Scheme	95
6.3 Methods	98
6.3.1 Walker System Synthesis	98
6.3.2 Imaging DNA Walking and Data Analysis	101
6.3.3 Simulation of 2-D DNA Walking	101
6.3.4 Regulation of 2-D DNA Walking	102
6.4 Results	104
6.4.1 Nuclease Powered 2-D DNA Walking	104
6.4.2 Effect of Walker Valence	109
6.4.3 Effect of Walker Strand Length	109
6.4.4 Inhibition and Activation of Walking	112
6.5 Discussion	114
6.5.1 Energy Efficiency of DNA based Transport	114
6.5.2 Rate-limiting Step in Walker Translocation	115
6.6 Conclusions	117
7. CONCLUSIONS AND FUTURE WORKS	119
7.1 Conclusions	119
7.2 Future Works	120
REFERENCES	122
VITA	138
PUBLICATIONS	139

LIST OF TABLES

Table	Page
4.1 Sequence information for DNAzyme walkers with different enzymatic core.	54
4.2 Sequence information for DNAzyme walkers in solution measurement and photoregulation experiments.	55
4.3 Sequence information for DNAzyme walkers with different arm lengths. . .	56
4.4 Comparison of cleavage reaction rate k_1 values.	63
5.1 Sequence information for DNAzyme walker and RNA fuel.	76
6.1 Sequence information for DNA walkers and RNA fuels.	99
6.2 Criteria for categorizing different walking modes using MSD.	108

LIST OF FIGURES

Figure	Page
1.1 (a) Schematic representation of a DNA walker (upper) and its dynamics model (lower). The walker is immobilized on a track through complementary anchor binding (left). The track is decorated with anchor strands such that spontaneous branch migration to the next anchor lowers system free energy (G). Repetition of such processes enables a continuous walking (middle). Introduction of fuel strands displaces walker foot on the anchorage and recycles the walker to the high free energy state (right). (b) Presence of a toehold modulates the kinetics of strand displacement. Displacement through the toehold is much faster compared to blunt-end strand displacement. All toeholds are colored in orange (b/\bar{b}).	3
1.2 Walking mechanisms. (a) and (b) are hybridization powered walking [18, 39]. (a) Walker design based on base-pairing and toehold-mediated strand displacement [18]. (b) walking achieved through toehold exchange by hairpin fuel [39]. (c) DNAzyme walker translocation through hydrolysis of fuel strands hydrolysis and toehold-mediated strand displacement [21]. (d) Walker design based on photonic energy. Pyrene modified strand assists photolysis of a di-sulfur bond incorporated in fuel DNA [38]. (e) and (f) Walker powered by conformational transitions [27, 38]. (e) Walker conformational states change between duplex, i-motif, and T-Hg ²⁺ -T complex based on environmental signals. Each conformation has different stabilities under different environments. Cycling between different environments enables walking [40]. (f) Fusing azobenzene on DNA walker strands exploits its UV/VIS illumination induced isomerization to changes duplex stability. Asymmetric track design allows linear translation through repeated UV/VIS illumination [41].	5

Figure	Page
1.3 Characterization methods for DNA walker studies. (a) Upper: AFM image sequences showing a DNA spider walking on a DNA origami tile. Total measurement time is 30 mins [33]. Lower: AFM kymograph showing image slices collected at 0.1 Hz. Stepwise motion between 4 stators is observed. [45] (b) Single molecule ALEX-FRET [46]. FRET efficiency (E) and molecule stoichiometry (S) are plotted to construct a 2D plot. Statistical analysis of the data cluster in the plot reveals the system state and operation yield. (c) Fluorescence microscopy images of a DNA spider [33, 40]. Stage drifting due to mechanical and thermal relaxation is shown in the left panel. Drift corrected image shows a linear motion of 100 nm (middle). The walker trajectory and the predicted track position are overlaid in the right panel. (d) Fluorescence imaging of a DNAzyme walker constructed from oligonucleotides and fluorescent nanomaterials [35]. A walker-decorated CdS quantum dot serves as a probe for the walker position in the visible image, while the track structure is imaged by the near-infrared emission of a SWCNT.	7
1.4 Sub-diffraction fluorescence imaging techniques. (a) Typical image of a single fluorophore is a pixelated PSF with around 200 nm diameter. Fitting the PSF with a Gaussian function allows sub 10 nm localization of the fluorophore position [58]. (b) Single fluorophore tracking using Gaussian fitting resolves 7 nm step length [59]. (c) Super-resolution principle of STORM and PALM [60, 61]. The spacially overlapping fluorophores are separated by randomly activating a subset of all fluorophores and localized by Gaussian fitting. The images shows microtubule (green) and mitochondria (magenta). (d) STED microscopy mechanism [61, 62]. Images are immunolabeled vimentin in a mammalian cell.	10
1.5 Optical properties of SWCNT. (a) Semiconducting SWCNT DOS. Sharp peaks shown in the plot are known as Van Hove singularities. The electronic transitions between DOS peaks (E_{ii}) show major optical absorption and emission energies calculated from an one-electron model [76]. The DOS for 2-D graphene (dotted line) is also shown. (b) 2-D PLE map of excitation and emission wavelengths of multiple SWCNT species in sodium cholate dispersed nanotubes. (c) Semiconducting SWCNT Kataura plot. Solid scatters are spectroscopic measurement data and open symbols are theoretical predictions of optical transition energies [75]. (d) Comparison of SWCNT and organic dyes photostability [77].	13
1.6 Optical properties of biological tissues and water in NIR. (a) Autofluorescence intensity [90]. (b) Scattering coefficient [91]. (c) Extinction coefficient [92]. (d) Water absorption [91].	15

Figure	Page
1.7 Optical properties of quantum dots. (a) Photograph and emission spectra of QD solution with different QD size. The change in emission wavelength is a result of quantum confinement effect [4]. (b) Top: emission intermittency (blinking) of a single QD. Bottom: addition of short thiol effectively suppress the blinking behavior by removing surface trapping state [96]. (c) TEM images of core/shell QD [97]. (d) QD emission wavelength tuning by lattice strain. The wavelength can be tuned from the visible to the NIR range [98].	16
2.1 AFM characterization of length sorted D/RNA-SWCNTs. (a) 4% PEG: 100 nm SWCNTs; (b) 3% PEG: 300 nm SWCNTs; (c) 2% PEG: 500 nm SWCNTs; (d) 1% PEG: 500 ~ 1500 nm SWCNTs.	22
2.2 Characterization of CdTe/CdS QD size and optical properties. (a) An AFM image of a large number of QDs deposited onto a flat Mica surface. (b) QD size distribution extracted from the hight profile of the AFM image. (c) Photostability of CdTe/CdS core/shell QD. The QDs are diluted with $1\times$ PBS and 20 mM DTT. Time trace of the emission is measured by a fluorometer with 0.1s integration time and 1s measurement interval. (d) Photon counts of the QDs obtained from a microscope image. The QDs are immobilized to the imaging surface in a flow channel with $1\times$ PBS and 20mM DTT. Typical emissions from QDs are ≈ 1000 photons at 1s integration time. The background intensity has a standard deviation of 50 photons.	24
2.3 Flow channel assembly and surface characterization. (a) Schematic of the flow channel. The channels are cut in adhesive tapes. Imaging surfaces are first treated with a layer of dimethyldichlorosilane (DSS) grafted onto its surface. The channel array is then sandwiched in-between coverslip and slide. Connector ports are attached to the slides to form inlets and outlets. (b) Surface passivation characterization. First column: QDs and SWCNTs uniformly adsorb onto the DSS surface without any blocking buffer. Second and Third column: Tween 20 and biotinylated BSA adsorbs onto the DSS surface and form a blocking layer to prevent non-specific adsorption of QDs and SWCNTs. Fourth column: with the presence of streptavidin, biotinylated RNA functionalized SWCNTs specifically adsorb onto the surface. QDs are still repelled by the surface. The scale bars are 5 μm for all images.	27

Figure	Page
3.1 Overview of porphyrin structures and sensing scheme. Top: chemical structures of porphyrins species in heme biosynthesis. Bottom: multiplexed optical quantification scheme for the 4 porphyrins species. The quenching of a-SWCNT fluorescence relates to FePP concentration. PP concentration is determined by fluorescence quenching of porphyrin mixture. CP and UP concentrations can be calculated from their Soret band absorption.	31
3.2 Nanotube emission quenching by porphyrins. (a) The emission of (7,5) SWCNTs (Excitation 658 nm) before (red) and after (black) the addition of porphyrin. The ratio between DNA and porphyrin is 5:1. (b) Selective a-SWCNT fluorescence (excitation 567nm) quenching by FePP. No significant decrease in the nanotube fluorescence intensity was observed with the addition of BSA, lysozyme, and phthalocyanine (analyte:DNA = 1:5). Upon FePP addition, nanotube fluorescence dropped immediately. All the experiments were carried out in 1X Tris buffer and the dilution effects are corrected.	36
3.3 Optical signature of porphyrins/aptamer/a-SWCNTs interaction. (a) Porphyrin absorption spectra before (black) and after aptamer (red) or a-SWCNTs (blue) addition. Only FePP and PP absorption show significant spectral change, which indicates stronger interaction between porphyrin and the aptamer strands. (b) Porphyrin fluorescence (black) spectra upon addition of aptamer (red) and a-SWCNTs (blue). Similar to the absorption, no detectable interactions are observed for CP and UP. In all measurements (except for PP), porphyrins and aptamer strands are kept at equal molar ratio. For PP, additional aptamer strands (pink) and a-SWCNTs (green) were added (porphyrin:DNA = 1:5) due to lower binding affinity.	38
3.4 Optical signatures for porphyrin/human telomere DNA-functionalized SWCNTs interaction. Compared to FePP-binding aptamer DNA, a 24-nt human telomere DNA (5'-AGG GTT AGGGTT AGG GTT AGG GTT-3') strand was used. The first row shows porphyrin absorption shift upon DNA (red) and DNA-SWCNTs (blue) addition. The second row shows porphyrin fluorescence change. In both absorption and fluorescence measurements, the ratios between porphyrin DNA were kept at 1:1. The third row shows SWCNT fluorescence upon addition of porphyrins (porphyrin/DNA = 1:5). Quenching is observed with FePP addition only.	39

- 3.5 Multiplexed porphyrin quantification scheme. **(a)** SWCNT emission quenching by FePP, from which the FePP concentration can be obtained. **(b)** Porphyrin mixture emission quenching upon a-SWCNTs addition. An excess amount of a-SWCNTs was added to ensure complete PP fluorescence quenching. **(c)** Difference spectrum constructed from **(b)** shows PP fluorescence, which can be used to quantify PP concentration. **(d)** Total absorption spectrum (blue) of CP (black) and UP (red) obtained by subtracting fractions of FePP and PP. **(e)** The experimental determination of the isosbestic point of CP and UP at 391nm. **(f)** Absorption peak shift with increasing UP concentration. The total concentration of CP and UP mixture can be determined from **(d)** at its isosbestic point, while individual fractions of CP and UP is determined by the absorption peak position. 42
- 3.6 Results of porphyrin mixture quantification. Top row: porphyrin optical absorption and emission, as well as a-SWCNT NIR emission quenching. Middle row: the estimated fraction of each porphyrin type compared to that of the experimentally measured mixture values. Bottom row: experimentally measured absorption and fluorescence spectra compared with the recovered spectra from calculation. 43
- 3.7 *In-situ* quantification of porphyrins in blood plasma. Porphyrins were added to human plasma sample with known concentrations. The sample was then subjected to solvent extraction and optical quantification. White bar shows the extracted values and the gray bar represents the calculated concentrations of each porphyrin species. Numbers above the columns also indicates the corresponding concentrations. 45

- 4.1 DNAzyme walking mechanisms. **(a)** A CdS quantum dot (yellow sphere) is decorated with DNAzyme. The walking process starts with the walker strand (E) associated to a fuel strand (S1) immobilized onto nanotube sidewall. The walker strand contains a catalytic core (green) and two recognition arms (red). The catalytic core E hydrolyze the RNA fuel at specific site (pink) at the presence of metal cations (Mg^{2+}), creating a nick site and a less stable duplex structure with two fragments (P1 and P2). The upper fragment will then be replaced by the next intact fuel strand (S2) at rate k_2 . As a full complementary binding with strand S2 is thermodynamically more favorable, the lower walker arm will spontaneously migrate to S2 at rate k_3 . The three steps completes a single enzymatic turnover. Repetition of this process leads to autonomous, processive and directional movement, which can be directly imaged using the fluorescence of quantum dot and nanotube. **(b)** Walker strand with four different types of DNAzymes core. Black triangles indicates azobenzene modification site in photo-regulation experiments. Yellow pentagram indicates FAM fluorophore for solution based reaction rate measurement. 49
- 4.2 Schematic of optical setup and image co-localization method. 57
- 4.3 Ensemble turnover rate measurement. **(a)** Schematic of the microfluidic reaction chamber for the DZ7 walker experiments to measure the single turnover reaction rate from an ensemble sample. The buffer is introduced from an inlet and flows through the microchannel to an outlet. **(b)** The single turnover reaction rates obtained from the fluorophore-attached ensemble sample (left bar) and from the single-particle/ single-tube spectroscopy of a single DNA walker (right bar). **(c)** The PL signature of P1-attached fluorophores was recorded in the presence of 50 mM Mg^{2+} , whereas no measurable PL signal was observed in the absence of Mg^{2+} (*i.e.* 0 mM metal cation). **(d)** A flow rate of 100 L hr^{-1} is used to collect the byproducts (cleaved RNA fragment P1) from the DNA walker operation at the outlet of the microchannel. No apparent effect of the buffer flow is observed on the DNA walker translocation. 60

Figure	Page
4.4 Walker motility as a function of DNAzyme type, recognition arm lengths, and environmental factors. Speed (scatter) and simulated single turnover rates (lines) are plotted in the first column. The cleavage reaction rates (k_1) at 100 mM Mg^{2+} , upper and lower arm replacement rates (k_2, k_3) are extracted from the kinetic model and plotted in the three bar charts on the right. (a-d) Effect of enzymatic core type. The DNAzyme walker is configured with 7/16-nt arm. (e-h) Effect of total arm length. 10-23 DNAzyme walkers with 4/4-nt, 7/7-nt, and 13/13-nt arm length are compared. (i-l) Effect of asymmetric arm lengths. 10-23 DNAzyme cleavage core is used for all the cases. (m-p) Effect of various metal cations (Mn^{2+} , Cd^{2+} , and Mg^{2+}) on 7/16-nt armed DZ7 DNAzyme walker motility. All experiments were performed in $1\times$ TAE buffer at room temperature.	62
4.5 DNAzyme walker with high motility and processivity. The time-lapse images show the movement of a DZ7 DNAzyme powered walker with 7/16-nt arm configuration. The walker position is shown as a red dot and emphasized with a yellow arrow. The walker propels itself for $\sim 5\ \mu\text{m}$ along the nanotube track with an average speed of $\sim 1\ \text{nm s}^{-1}$ in the presence of 100 mM Mn^{2+} at 25°C and pH 8.0. The blinking of CdS QD shown on the left confirms the single nanoparticle identity.	66
4.6 Photo-regulation of a DNAzyme walker using azobenzene moiety. (a) Schematic of DNA duplex formation controlled by photo-switchable <i>trans</i> - and <i>cis</i> - form of the azobenzene incorporated into the upper arm of the walker strand. (b) Displacement plot and (c) the corresponding speed plot of a 10-23 DNAzyme walker with alternating UV/visible illumination. Exposure of azobenzene under continuous UV light for 10 min transforms its structure from <i>trans</i> into <i>cis</i> form, inhibiting any walking due to dissociated upper arm. Walking activity can be restored after 10 min visible illumination. An average velocity of $\sim 200\ \text{nm hr}^{-1}$ is consistent for walkers with visible light or with no azobenzene moiety. The cation concentration in the TAE buffer is 100 mM Mg^{2+}	67
4.7 Motility of DZ7 and 8-17 DNAzyme walker with azobenzene incorporated in the enzymatic core after UV (red) and visible (blue) illumination for 10min. (a) and (c) show experimentally determined speed (scatter) and simulated single turnover rate (line). (b) and (d) presents rate k_1 of the DZ7 and 8-17 DNAzyme walker at 100 mM Mg^{2+} , respectively.	68

- 5.1 Schematic of the DNAzyme walker walking mechanism. **(a)** Scheme of a DNAzyme walker on a coverslip for imaging. Biotin-BSA is attached to the coverslip, serving as anchors for nanotube track. The coverslip is passivated by DDS-Tween 20 to prevent non-specific interaction with the walker strand. 3' biotinylated RNA and RNA fuel strands functionalized carbon nanotube binds to the surface through streptavidin. CdTe/CdS quantum dots with functionalized by DNAzyme walker strands conjugate to the immobilized nanotube track through complementary base-pairing. **(b)** An AFM image showing the walker system presented in **(a)**. **(c)** Reaction steps during DNAzyme single turnover. The walking process has similar principles as presented in Figure 4.1 with more detailed intermediate reactions for optical identification. 75
- 5.2 Experimental setup and imaging scheme. Optical image system setup. Output of two laser lines are passed through clean-up filters and directed into the backport of the microscope. A diaphragm in the reflected light channel is used to modulate the excitation intensity. The excitation beams are focused onto the sample stage through a $63\times$ objective lens. Emission light from the sample are separated into two light paths (NIR and VIS) and imaged using corresponding cameras. The emission spectra of both QD and SWCNT are shown above the camera image. A $2\times$ magnifier lens is placed in the NIR light path before the camera. Scale bars are 500 nm. 79
- 5.3 Characterization on the localization and drift correction precision. QDs and SWCNTs are fixed onto a non-passivated surface and imaged in $1\times$ PBS buffer and 20 mM DTT. The images are continuously acquired at 1 s integration time and 5 s measurement interval. A total of 500 images are acquired analyzed. **(a)** Precision of QD localization. Centroids of Gaussian fitting of 10 successive frames are shown. The precision of localization is measured by the standard deviation $\Delta d \approx 16$ nm from the mean position of the 10 fitting. **(b)** Precision of drift correction on QD image. The drifting of QD image due to stage relaxation is corrected by subtraction the drifting traces of the NIR images of the nanotube and the average drifting of other QDs. Centroids of Gaussian fitting of all the frames after drift correction are shown. A standard deviation of $\Delta d \approx 24$ nm is obtained. 81
- 5.4 Simulated translocation of DNA walker. 3 sets of (n, k) combinations are tested with 500 steps for each walker and 100 walkers for each case. Different cases are color coded as follows: red : $n = 1$; blue : $n = 2$; black : $n = 3$. **(a)** Averaged displacement. **(b)** Displacement variance of all walkers. 85

Figure	Page
5.5	Sub-diffraction imaging scheme for both VIS and NIR images. (a)-(b) Gaussian fitting of QD PSF is used to estimate its centroid. The average result from 10 localizations are used as the final position. (c)-(h) the intensity fluctuation of the pixel labeled #1 in a NIR nanotube image (c) is presented in intensity vs. time plot (e) . The reaction center of such intensity change is isolated by constructing difference image of successive frames ((f)-(h)) . The separated PSFs are localized to reconstruct the sub-diffraction nanotube image (d) . The localized VIS and NIR images are registered to produce the overlaid image (i) . The QD position is emphasized by a green arrow. Scale bars are 500 nm. 87
5.6	Raw and sub-diffraction images of a DZ-7 enzyme walker operation in $1 \times$ PBS with 10 mM Mg^{2+} and 20 mM DTT. The walker travels approximately 200 nm in 10 min. The images are taken at a 5 s interval and localized using the scheme shown in Figure 5.5. The walking trajectory is plotted in a $400 \text{ nm} \times 400 \text{ nm}$ grid for better visualization of the distance. The scale bar is 500 nm. 88
5.7	Quantitative evaluation of a 10-23 enzyme walker. (a) Displacement of the 3 walkers (blue scatter) as compared to control experiment (black scatter). The smoothed displacement from averaging successive 10 localizations is plotted as a solid curve. Control experiment is conducted without any Mg^{2+} . (b) Velocity distribution of DNAzyme walkers generated from data shown in Figure 5.8. The histogram is fitted to a Gaussian distribution with mean value $\sim 7.8 \text{ nm min}^{-1}$. (c) Walker MSD. Black lines are the time averaged MSD from a single walker trajectory. Black scatters are ensemble averaged data. The MSD is fitted to a power-law function with a scaling exponent $\alpha = 1.72$. The first 10 scatter points are linear fitted (blue line) and extended for better visualizing the deviation of walker MSD from diffusive motion. (d) Displacement variance of experimental (black scatter) and simulated data (line). 3 cases with different intermediate reaction numbers, $n=1$ (black), $n=2$ (red), $n=3$ (blue), are presented. Linear fitted (blue line) line was used to determine the slope of ~ 0.34 . . . 90

Figure	Page
5.8 Displacement plots of all datasets used in this study. All the traces are obtained from experiments of 10-23 DNA enzyme decorated QD moving along a carbon nanotube in $1\times$ PBS, 10 mM Mg^{2+} and 20 mM DTT. Localizations from a single frame is plotted as scatter points and the average position from 10 localizations are plotted as a smoothed curve. (a) Displacements showing processive walking. These datasets are used in the analysis for displacement variance, velocity distribution, and MSD. (b) Displacements showing stalling and back-stepping due to possible assembly defects on the nanotube surface. These datasets are excluded from our analysis.	91
6.1 Scheme for 2-D DNA transport system. Multiple walker strands (red) are attached to a fluorescent particle. The particle is immobilized onto the imaging surface through the complementary binding of DNA walker legs with RNA fuels (blue) on surface. Multiple legs on the particle can bind to surface fuel simultaneously. The RNA fuels are grafted onto the surface through biotin-streptavidin interaction (orange-blue). The surface is passivated by BSA and DDS/Tween 20 as described in Chapter 5. Nuclease (green) cleaves the formed walker/fuel duplex, driving the walker legs to associate with intact fuel strands.	96
6.2 2-D transport mechanism. (a) Mechanism for enzymatic DNA walker. Fluorescent particles decorated with DNA walker strands associate with RNA fuel strands on particle surface. RNase H then cleaves the RNA strands and frees part of the walker leg (state (i) to (ii)) for binding with the next available fuel (state (ii) to (iii)). After association with the next fuel, the walker detaches from the consumed fuel and gradually migrates to the intact fuel (state (iii) to (iv)). (b) Schematic and scaling feature of a 2-D self-avoiding walking. The walker avoids its own path, thus is biased away from random diffusion (dashed line), demonstrating super-diffusive behavior. The scaling of the walker MSD follows $t * \log(t)$ (green line). . . .	97
6.3 Characterization of RNA fuel density. (a) Schematic of surface characterization method. All anchoring sites for RNA fuels are labeled with SA-QDs for fluorescence measurement. (b) Fluorescence intensity of SA-QDs conjugated onto the surface over time. (c) The density increases as a function of time.	100

- 6.4 2-D DNA walker simulation. **(a)** Simulation of a single-legged walker. The walker determines length l and time τ during a single step based on a user defined probability distribution. The direction of walker stepping is determined by the smallest stepping time τ . The MSD of such single legged walker shows super-diffusive feature and follows the scaling of $t * \log(t)$. **(b)** simulation of a 4-legged walker. The four legs are shown in red and the centroid of the walker is shown in blue. Two types of leg behaviors (lead or follow) are randomly assigned to the four legs. If two legs are assigned as lead legs (L1 and L2), they step based on the same scheme as described in **(a)** and centroid position is recomputed based on the current positions of the four legs. The two remaining legs (L3 and L4) will be assigned a biased rate towards the position of the centroid when stepping, thus will have the tendency to follow the centroid. The centroid position will be updated again after all the legs are moved. The MSD of 4-legged walker shows diffusive behaviors but ultimately converges to the scaling feature of $t * \log(t)$ 103
- 6.5 DNA powered walking in 2-D surface. **(a)** Time-lapse images of a fPS particle powered by DNA walkers. The trajectories of the walker is plotted in red. The total time for the movement is 20 min. The scale bar is 1 μm . **(b)** Ensemble averaged MSD of 2-D walkers. The MSD (red) follows the expected behavior of a multi-legged walker traveling in a “self-avoiding” fashion. MSD of simulated 2-D walkers are also plotted in blue for comparison. Dashed lines represents diffusive (bottom) or drift (top) motions. **(c)** Velocity distribution of the walker shown in **(a)**. The average velocity of the walker is approximately 15 nm s^{-1} 105
- 6.6 Characteristics of different walking modes. **(a)** Time-lapse images of a 200 nm moving fPS particle. **(b)** The trajectory of the walker shown in **(a)**. Regions showing distinctly different motility characteristics from typical walking are labeled. **(c)**. Scheme of different walking modes. Tethered walkers have typically less than 100 nm total displacement. Active walkers follow the expected “self-avoiding” behavior and travel processively over long distance. Diffusive walkers are less processive compared to active walkers, thus traveling randomly. **(d)** The velocity distribution and walking yield of active and diffusive walkers. Diffusive walkers have a much wider distribution as compared to the processive active walkers. The yield of a DNA walker with 13/0 configuration is shown in the pie chart. . . . 106

Figure	Page
6.7 Negative control for enzymatic walking process. The Effects of Tween 20, RNA fuel and RNase H were examined. The plus and minus signs indicate whether certain molecules are present (+) or not (-). For the case of RNA fuel, the negative control was performed by replacing the RNA portion in the fuel to DNA with the same sequence.	108
6.8 Valence effect on DNA walking. (a) The velocity distribution (counts) of walkers with different valences. For low valence 20 nm walkers there is a much wider distribution as compared to 200 nm walkers. The velocity at the peak of the distribution is similar to that of the 200 nm walkers at ~ 15 nm s ⁻¹ . (b) The same distribution plotted in frequency and corresponding walker yields (pie chart). Low-valence 20 nm particles show a smaller portion of tethered walking, although they are less processive compared to high-valence 200-nm particle.	110
6.9 Walker length effect on 200 nm FPS. (a) Velocity distribution comparison of 13/7 and 13/0 configurations. Longer lower arm will ensure the walker travel more processively, thus having a narrower traveling velocity distribution. Both configurations have similar average velocity and yields. (b) Velocity distribution comparison of 8/0 and 13/0 configurations. Shorter upper arm increased the walking yield, but maintains a similar average velocity and processivity.	111
6.10 Walker length effect on 20 nm FPS. (a) Velocity distribution and yields of 13/7 and 13/0 configured walkers. Both walkers have similar motility and processivity, although the 13/7 walker appears to have a higher yield. (b) Velocity distribution and yields of 13/0 and 15/15 configured walkers. The 15/15 walker has a significantly lower yield compared to that of 13/0 walker, but the average velocity and distribution remain similar.	112
6.11 Scheme for motor function regulation. (a) Scheme showing the additional regulation region on the fuel strand. Green represents regulation region, blue represents motor function part and black represents anchor region. (b) Scheme showing the regulation of motor function using hairpin structured fuel and oligonucleotide signals. First step: the RNA fuel is sequestered in the hairpin conformation induced by the inhibitor strand, which turns off motor function; Second step: the addition of activator strand leads to the complete displacement of the inhibitor from the fuel strand, thus recovering the DNA walkers' motor function. (c) Summary of walking yields when motor functions are inhibited and activated.	113

- 6.12 Increased walker motility in high density fuel surface. **(a)** Velocity distribution of 13/0 configured walkers traveling on two surfaces with different fuel density. Walkers moving on a high density surface shows an average velocity of around 25 nm s^{-1} as compared to 15 nm s^{-1} of walkers on low fuel density surface. **(b)** Simulation results of walkers moving on a high density and low density surface. The scaling of walker MSD shows significant difference for walkers in different density conditions. The inset in **(b)** shows an enlarged image of the same medium and low density walker MSD.116

ABBREVIATIONS

CNT	Carbon nanotube
SWCNT	Single-walled carbon nanotube
a-SWCNT	Aptamer Single-walled carbon nanotube
QD	Quantum dot
SC	Sodium cholate
OD	Optical density
BSA	Bovine serum albumin
DDS	Dichlorodimethylsilane
NIR	Near infra red
MSD	Mean squared displacement
PSF	Point spread function
FRET	Föster resonance energy transfer
PL	Photoluminescence
MSD	Mean squared displacement
MW	Molecular Weight

NOMENCLATURE

TAE	Tris acetate EDTA buffer
TBS	Tris buffered saline buffer
EDTA	Ethylenediaminetetraacetic acid trisodium salt hydrate
Tween 20	Polyoxyethylene (20) sorbitan monolaurate
EMCCD	Electron multiplying charge coupled device
EDC	1-ethyl-3-(3-dimethylaminopropyl) carbodiimide hydrochloride
MES	2-(N-morpholino)ethanesulfonic acid

ABSTRACT

Pan, Jing PhD, Purdue University, December 2017. Biophysics of DNA based Nanosystems Probed by Optical Nanoscopy. Major Professor: Jong Hyun Choi, School of Mechanical Engineering.

A dynamic DNA nanosystem exploits the programmable structure and energy landscape of DNA self-assembly to encode designed processes in a fluctuating molecular environment. One type of such a dynamic system, DNA walker, is reminiscent of biological motor proteins that convert chemical energy into mechanical translocation. Typical DNA walker travels tens of nanometers at a speed orders of magnitude slower than motor proteins. Two major challenges limited the development of functional DNA walkers. First, there are no suitable characterization methods that offer adequate spatial and temporal resolution to extract walker kinetics. Second, no guidelines have been established for the design and development of DNA walkers with specified properties. In this work, an enzymatic DNA walker system that integrate oligonucleotides with nanomaterials is designed. This approach takes advantage of novel optical properties of nanomaterials and sub-diffraction imaging techniques to study the kinetics and biophysical nature of synthetic DNA walkers. Design principles are extracted from walker kinetics for constructing functional walkers that can rival motor proteins. Multiple schemes are explored to regulate the walker motility so that various behaviors can be encoded into the system. This work demonstrates novel methods to design and construct molecular systems with programmed functions, which will pave the road for creating synthetic systems with encoded behaviors from the bottom up.

1. INTRODUCTION

With the development of nanotechnology, human engineering capabilities have reached down to the molecular scale. The construction of such miniaturized systems requires novel materials and engineering approaches. Low dimensional nanomaterials with unique physical and chemical properties have been synthesized and characterized for applications in nanoscale systems [1–5]. Biomaterials such as deoxyribonucleic acid (DNA) also emerge as appealing building blocks for artificial systems with biological functionalities. The great structural and functional programmability of biomaterials enable researchers to build complex nano-structures and molecular machineries from bottom-up [6–8]. This thesis presents the engineering of nanosystems that consist of novel optical nanomaterials and synthetic short DNA strands. Such nanosystems provide a unique platform for optically revealing the biophysics of dynamic processes such as DNA enzymatic cleavage or strand displacement, holding great promise for building high performance DNA based dynamic systems.

This chapter introduces the recent development of dynamic DNA nanotechnology and the novel optical properties of nanomaterials. Our research efforts in using optical nanomaterials to study the biophysical nature of DNA based nanosystems are summarized in the scope of study. The organization of the entire thesis is also presented.

1.1 DNA Nanosystems and Optical Nanomaterials

1.1.1 Dynamic DNA Nanotechnology and DNA Walkers

Biomolecules present a distinct type of nanomaterial. Unlike solid phase materials whose periodic crystal structure give rise to specific physico-chemical properties, biomolecules excel at self-assembly into complex geometries through intra and inter

molecular non-covalent interactions for performing specific tasks in a biological environment. For example, the folding (intra molecular assembly) of polypeptide chains into the quaternary structure of proteins and the self-assembly of lipids into membranes are all critical biological processes [9]. DNA is one particularly important type of biomolecules that can self-assemble into antiparallel double helix structure for genetic information storage. The specificity of base-pairing makes it possible to program instructions for self-assembly into DNA molecules, which has led to various complicated nanoscale structures [6]. Biochemical reaction processes of DNA such as strands hybridization can also be controlled by designing specific DNA sequences, which has yielded different dynamic DNA nano-mechanical systems [8]. Such devices include DNA nanomotors [10, 11], switches [12], sensors [13, 14], logic gates [15, 16]. Notably, DNA walkers that mimic biological protein motors, such as kinesin and dynein, have been demonstrated to actuate nanoscale motion [17–28].

A DNA walker system is usually constructed by initially immobilizing a walker strand to a track through complementary base-pairing with fuel strands as shown in Figure 1.1. The walking process can be understood from both dynamics and kinetics. Dynamically, continuous walker locomotion is realized by designing a bi-state system. Spontaneous relaxation from a higher energy state to a lower energy state drives walking, while fuel molecule consumption ensures walker recovery. The rich chemistry of DNA, such as hybridization, enzymatic reactions, and conformational changes, enables the repetitions of such energy cascades. Kinetically, non-equilibrium oligonucleotide reaction cascades that are biased to one direction allows continuous walker operation. Such biased reactions can be achieved through modulation of strand association and dissociation kinetics by its sequence and length. For example, oligonucleotide “toehold”, a small dangling strand fragment at the end of a duplex facilitates strand replacement by an invasion strand (Figure 1.1b). Strand displacement results from the dynamic equilibrium of DNA duplex annealing and melting, where an unpaired single strand replaces an identical strand in a duplex. The strand displacement

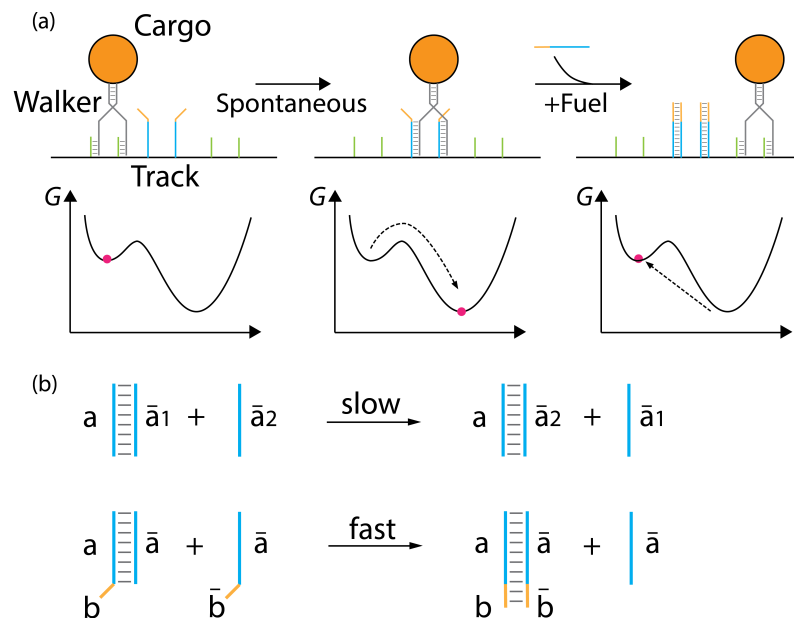


Figure 1.1. **(a)** Schematic representation of a DNA walker (upper) and its dynamics model (lower). The walker is immobilized on a track through complementary anchor binding (left). The track is decorated with anchor strands such that spontaneous branch migration to the next anchor lowers system free energy (G). Repetition of such processes enables a continuous walking (middle). Introduction of fuel strands displaces walker foot on the anchorage and recycles the walker to the high free energy state (right). **(b)** Presence of a toehold modulates the kinetics of strand displacement. Displacement through the toehold is much faster compared to blunt-end strand displacement. All toeholds are colored in orange (b/\bar{b}).

kinetics are length and position dependent over three orders of magnitude [29], which offers great flexibility in the design of DNA nanosystems.

The first few DNA walker systems were inspired by DNA nanomotors [10] by planting the motor substrates on the track. Seeman group [19] and Pierce group [18] designed bipedal walkers that used toehold-mediated strand displacement to replace walker foot on successive fuels along the track (Figure 1.2a and b). Such scheme use hybridization as the energy source to drive walking, which has later been demonstrated in multiple designs [25, 27, 28, 30, 31].

Various nucleotide reaction types and energy sources could be used to design more complex walking schemes [17, 20, 21, 24, 32–36]. Hydrolysis and ligation of the DNA phosphate backbone involve covalent modification instead of non-covalent base-pairing, thus providing additional energetic pathways for walker design (Figure 1.2c and d). For example, Yin et al. [17] demonstrated a system that transports DNA fragments through a series of cleavage and ligation reactions. Deoxyribozyme (DNAzyme) [21, 37] and restriction enzymes [20] were also used to extract chemical energy from anchored RNA fuels to power walking. In these schemes, enzymatic cleavage of fuel strands' phosphate backbone makes the duplex less stable. The dissociation of cleaved fuel fragments provides toehold on walker strand for faster association with the adjacent anchor (Figure 1.2c). Both biped [32] and multi-legged, enzymatic DNA walkers [33] that have each leg paired to an anchor strand on a track have been designed. In such designs, enzymatic cutting is used to release walker legs to allow translocation to the next available spot. Similar schemes using photonic energy for the hydrolysis of DNA backbone has also been demonstrated (Figure 1.2d) [38].

The free energy change associated with transitions between different DNA conformational isomers can also be used as walker energy source. Wang et al. [40] designed a biped walker system that changes conformation between thymine- Hg^{2+} -thymine (T) complex, double helix and i-motif (Figure 1.2e). When Hg^{2+} is present, the more stable thymine- Hg^{2+} -thymine complex drives one of the walker's two legs to the adjacent anchor position. In acidic environment, i-motif formation will move the walker's

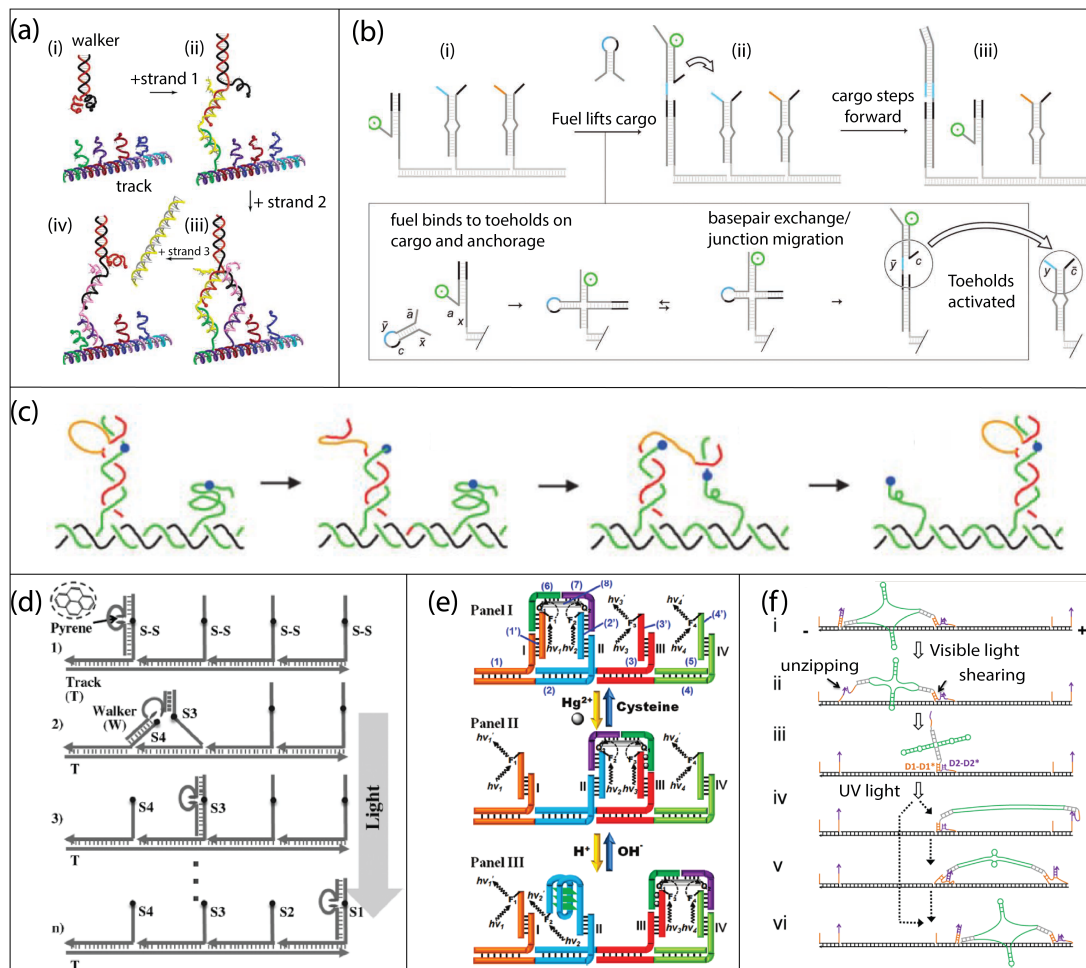


Figure 1.2. Walking mechanisms. (a) and (b) are hybridization powered walking [18, 39]. (a) Walker design based on base-pairing and toehold-mediated strand displacement [18]. (b) walking achieved through toehold exchange by hairpin fuel [39]. (c) DNAzyme walker translocation through hydrolysis of fuel strands hydrolysis and toehold-mediated strand displacement [21]. (d) Walker design based on photonic energy. Pyrene modified strand assists photolysis of a di-sulfur bond incorporated in fuel DNA [38]. (e) and (f) Walker powered by conformational transitions [27, 38]. (e) Walker conformational states change between duplex, i-motif, and T-Hg²⁺-T complex based on environmental signals. Each conformation has different stabilities under different environments. Cycling between different environments enables walking [40]. (f) Fusing azobenzene on DNA walker strands exploits its UV/VIS illumination induced isomerization to changes duplex stability. Asymmetric track design allows linear translation through repeated UV/VIS illumination [41].

trailing leg to adjacent fuel. The process is driven by the decrease in conformational free energy, which is estimated to be approximately $-11 \text{ kcal mol}^{-1}$ [42]. The incorporation of photosensitive molecules into walker strands has also been used to provide walker motility. Several walker designs [38, 41, 43, 44] utilized azobenzene to control walker duplex formation. Alternating UV/visible(VIS) illumination anneals/melts walker and fuel strands, thus driving the walker for processive walking(Figure 1.2f).

1.1.2 Characterization Techniques for DNA Nanosystems

The major characterization methods in DNA walker research are gel electrophoresis [39], atomic force microscopy (AFM) [33, 45], and optical methods. [35, 46] Each method sheds light onto different aspects of the walker system, but also has its own limitations. Gel electrophoresis and AFM provide rich structural information, but are limited when it comes to extracting kinetic information such as walker velocity and processivity statistics. Recent development of fast-scan AFM has greatly improved temporal resolution, and has been implemented for imaging molecular rotary motion [47] and linear translocation (Figure 1.3a) [33, 45, 48]. However, this method is instrumentally intensive and is invasive, which may potentially affect the walking process. Optical methods, such as föster resonance energy transfer (FRET) and fluorescence microscopy, are non-invasive and usually have desirable temporal resolution for probing walker kinetics. In fact, FRET has been widely used to measure various DNA based systems [28, 34]. In particular, the successful implementation of alternating laser excitation FRET (ALEX-FRET) in DNA walker study allows single molecule characterization [46, 49–51]. Single molecule measurements not only reveal the average value of walker translocation and velocity, but also provide important information on structural and kinetic multiplicity. Below we discuss optical methods that are capable of single molecule measurement.

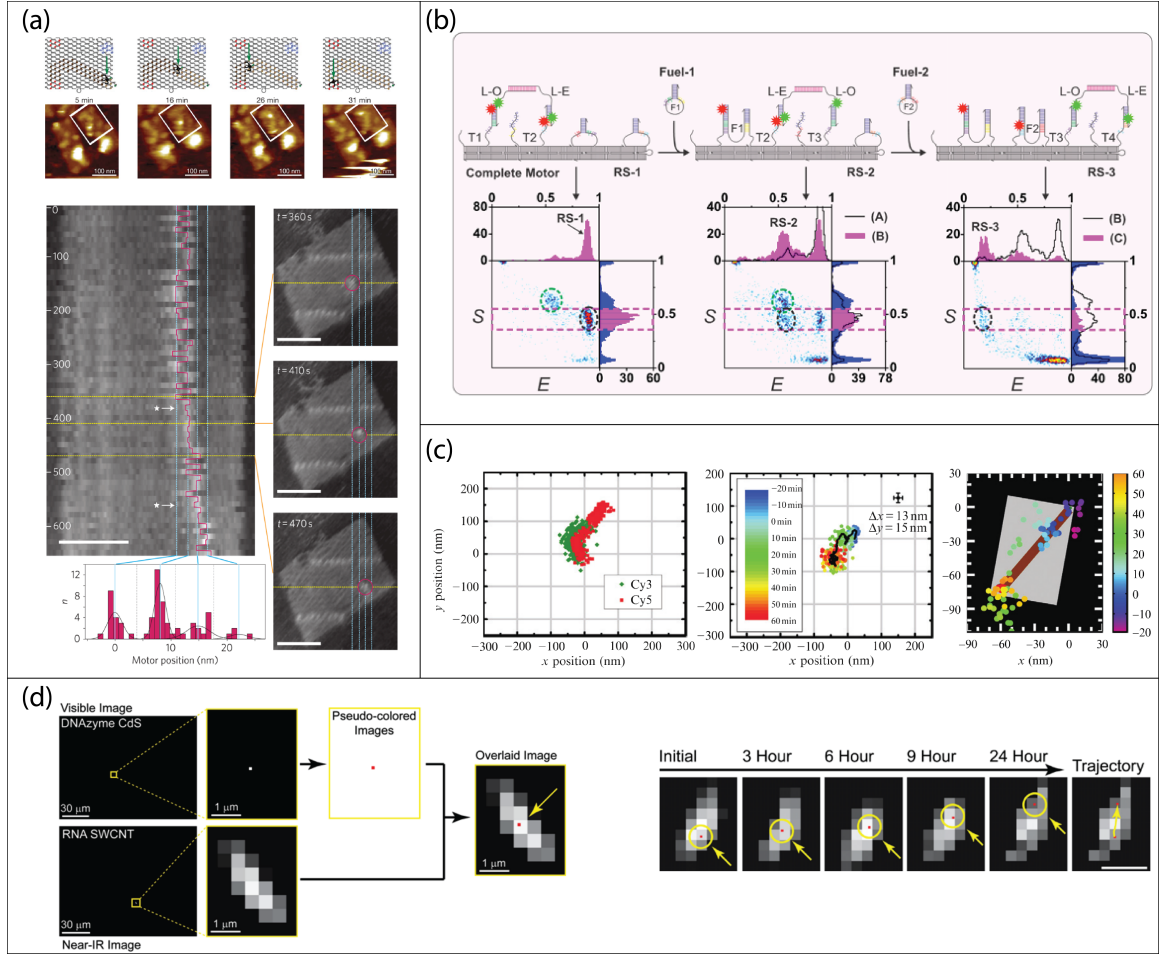


Figure 1.3. Characterization methods for DNA walker studies. **(a)** Upper: AFM image sequences showing a DNA spider walking on a DNA origami tile. Total measurement time is 30 mins [33]. Lower: AFM kymograph showing image slices collected at 0.1 Hz. Stepwise motion between 4 statoms is observed. [45] **(b)** Single molecule ALEX-FRET [46]. FRET efficiency (E) and molecule stoichiometry (S) are plotted to construct a 2D plot. Statistical analysis of the data cluster in the plot reveals the system state and operation yield. **(c)** Fluorescence microscopy images of a DNA spider [33, 40]. Stage drifting due to mechanical and thermal relaxation is shown in the left panel. Drift corrected image shows a linear motion of 100 nm (middle). The walker trajectory and the predicted track position are overlaid in the right panel. **(d)** Fluorescence imaging of a DNzyme walker constructed from oligonucleotides and fluorescent nanomaterials [35]. A walker-decorated CdS quantum dot serves as a probe for the walker position in the visible image, while the track structure is imaged by the near-infrared emission of a SWCNT.

1.1.2.1 Single Molecule Techniques

Solution based methods: Solution based FRET measurement on DNA walker systems typically extract ensemble averaged data such as walking kinetics. Recently implemented single molecule ALEX-FRET examines diffusive molecules in and out of excitation focal point. The intensity surge (*i.e.* photon bursts) in photodiode when a fluorophore attached walker moves into focus is then recorded for statistical analysis. The dispersion in molecular structures due to system complexity and mis-assembly is mapped after coupling molecular stoichiometry with FRET efficiency [46, 51]. As shown in Figure 1.3, the FRET efficiency gives an accurate estimation on the distance between the donor/acceptor pair while the stoichiometry value shows information on donor/acceptor ratio. DNA walker operation yield is derived from unwanted structures' percentage. Fuel design can also be improved by kinetic analysis [49, 50]. Since multiple diffusing molecules are imaged while the majority of the fluorophores remain protected from excitation light, photo-bleaching can be completely avoided. However, diffusion also makes it difficult to follow one single molecule for an extended time period, thus limiting its capability for probing variations in walker kinetics.

Surface based methods: Fluorescence microscopy imaging complements FRET by tracking long-term behavior of surface-bound molecules. Single particle tracking has been used to study various protein functions and intracellular processes, particularly the motion of protein motors [52–55]. However, DNA walkers have motility that is three orders of magnitude lower than protein motors. As a result, photo-bleaching of the optical probe and sample stage drifting become major issues for monitoring slow motion of DNA walkers. Various methods to prolong fluorophore photostability, such as using oxygen scavenger systems, have been used during the imaging of DNA walker operation. Fiduciary fluorescence markers such as a stationary micro-bead also has been used to compensate the stage drift (Figure 1.3c) [56]. A system containing semiconducting CdS nanocrystals, single-walled carbon nanotube (SWCNT) and DNA walkers have recently been demonstrated by our group, led by Dr. Tae-Gon

Cha [35]. CdS quantum dots (QD) with excellent photo-stability are used both as a cargo and optical probe for walker position. Carbon nanotubes, which fluoresce in the near-infrared (NIR) range (0.8~1.6 μm), serve as a walking track and marker for stage drift correction (Figure 1.3d). The walker displacement is imaged for over 30 hr, with an approximated total displacement of 3 μm .

1.1.2.2 Super-resolution Microscopy

Optical microscopy has been one of the most powerful and widely used platforms to study biological substances. However, its resolution is limited by optical diffraction, which is roughly $\lambda/2$ where λ is light wavelength [57]. As a result, one cannot optically distinguish any two light sources that are separated less than 200 nm.

Early research efforts to surpass the diffraction limit involve estimating centroid of the point spread function (PSF) of an individual fluorophore with Gaussian function (Figure 1.4a,b) [52, 53, 58, 59]. This method provides a high precision (<10 nm) for localizing an individual fluorophore and has been used for studying membrane protein diffusion and motor protein walking along cytoskeleton. However, it still cannot resolve the location of spatially overlapping fluorophores.

In the past decade, the so-termed super-resolution imaging technique has transformed the field of optical microscopy for biological research by providing new ways to visualize biological materials which is impossible with traditional light microscopes due to the optical diffraction limit. The method separates spatially overlapping fluorophores temporally by using phenomena known as reversible saturable/switchable optically linear fluorescence transitions (RESOLFT). A number of super-resolution microscopy strategies, including stochastic optical reconstruction microscopy (STORM) [60,63], stimulated emission depletion (STED) [62,64], and photo-activated localization microscopy (PALM) [61,65], have been demonstrated thus far (Figure 1.4). These methods enable researchers to probe intracellular structures and functionalities with unprecedented resolution. For studying dynamic biological pro-

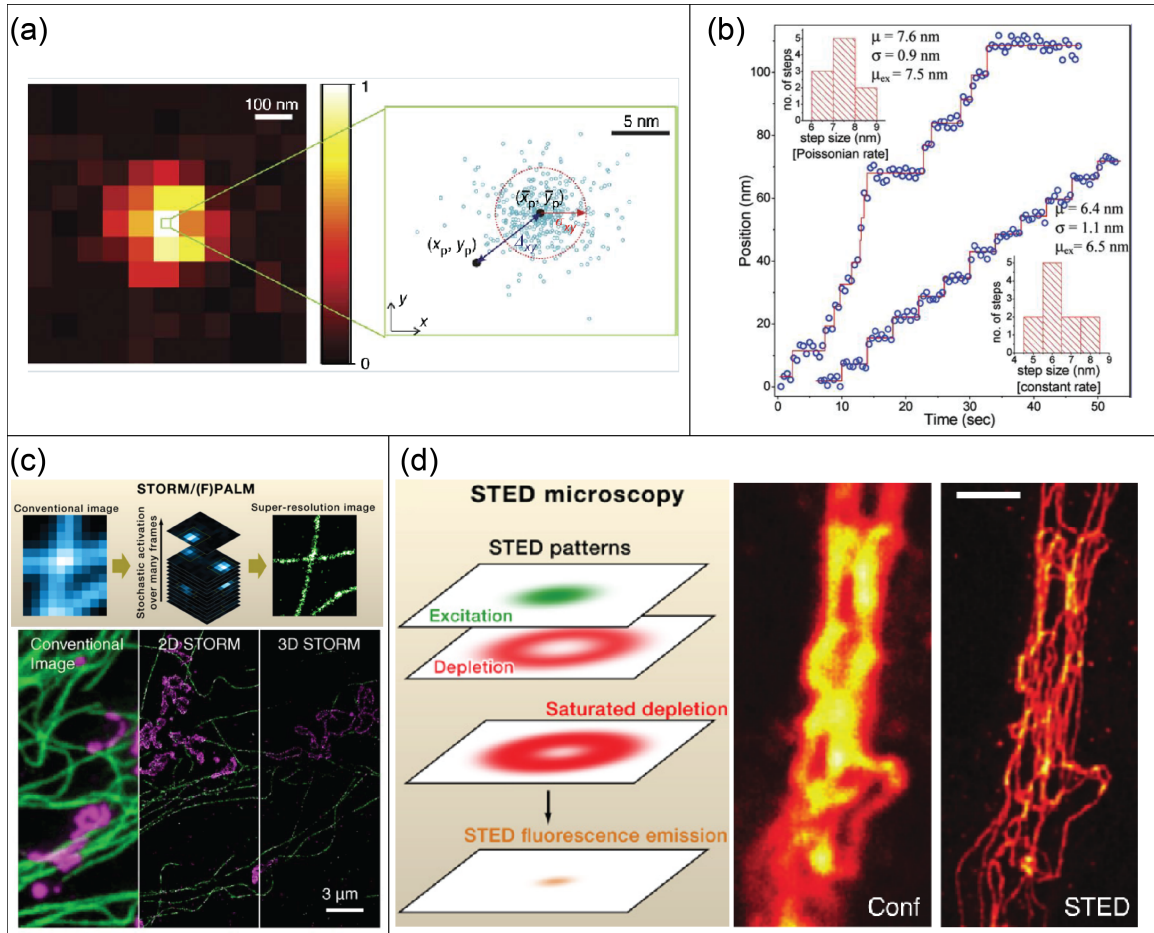


Figure 1.4. Sub-diffraction fluorescence imaging techniques. **(a)** Typical image of a single fluorophore is a pixelated PSF with around 200 nm diameter. Fitting the PSF with a Gaussian function allows sub 10 nm localization of the fluorophore position [58]. **(b)** Single fluorophore tracking using Gaussian fitting resolves 7 nm step length [59]. **(c)** Super-resolution principle of STORM and PALM [60, 61]. The spacially overlapping fluorophores are separated by randomly activating a subset of all fluorophores and localized by Gaussian fitting. The images shows microtubule (green) and mitochondria (magenta). **(d)** STED microscopy mechanism [61, 62]. Images are immunolabeled vimentin in a mammalian cell.

cesses, multi-color super-resolution imaging techniques have been introduced, which offer the possibility to assign every single molecule event to a corresponding probe class. A palette of probes based on photo-switchable fluorescent proteins and organic dyes have been created [63, 65–70]. However, the compromised low number of photons emitted from such probes tends to limit image resolution severely [65, 70, 71]. For organic dye based probes, either excitation [69], activation [63], or emission [68] wavelengths have been exploited to achieve multi-color super-resolution.

Super resolution microscopy methods also improved measurement accuracy for tracking slow moving particles. Several detailed reviews provide in-depth discussion on this topic [58, 72, 73]. With improving temporal and spatial resolution, we envision fluorescence microscopy will provide much detailed insights on DNA walker design.

1.1.3 Nanomaterials with Unique Optical Properties

Characterization of nanoscale structures and motion of dynamic DNA system benefits from novel optical materials developed by nanotechnology. Nanomaterials such as carbon nanotubes and quantum dots form the material basis for the development of nanoscience and nanotechnology. They are featured by small physical dimension in the nanometer scale, which is similar to the size of molecules. Such small physical dimension affects the material’s electronic configurations, yielding novel electrical and optical properties that are dependent on its size and structure. For example, the emissions from QDs and SWCNTs are both tunable through their structures, and the emissions are both photostable when compared to organic dyes.

1.1.3.1 Photophysics of Carbon Nanotubes

Single-walled carbon nanotube (SWCNT) can be considered as a rolled-up strip of planar graphene that forms a seamless cylindrical tube with a particular diameter and chiral angle. The distinct structures of the each nanotube species can be represented by a pair of integers (n,m) known as the chiral vector. SWCNT whose chiral vector

satisfies $n-m=0$ (the armchair structures) are metallic. Those with $n-m=3p$ (p is an integer) are semimetals. Nanotubes with $n-m \neq 3p$ are semiconductors [74]. Only semiconducting nanotubes show fluorescence. SWCNT is considered as a quasi-1D material, which gives rise to sharp peaks in their density of electronic states (DOS) known as Van Hove singularities (Figure 1.5a). Electronic transitions between these sharp peaks on opposite sides of the nanotube Fermi level determines its optical properties [75].

The first bandgap photoluminescence (PL) of carbon nanotubes was observed with SWCNTs isolated inside surfactant micelles [78]. The dispersed nanotubes show NIR emission in the 800~1600 nm wavelength range. The NIR emission is attributed to the band edge recombination of excitons, whose existence was confirmed by two-photon experiments [79]. Different species of carbon nanotubes have distinct optical signatures as a result of structural difference. Using Raman spectroscopy and photoluminescence excitation (PLE) spectra (Figure 1.5b), the fluorescence peak of each (n,m) nanotube species can be assigned [80].

The chiral (n,m) dependent optical transition energies, *i.e.* excitation and emission wavelengths, can be used to make a so-termed Kataura plot (Figure 1.5c). A Kataura plot shows the optical transition energies (E_{ii}) versus nanotube diameter. Both fluorescence spectroscopy [75] and theoretical calculations (tight binding model [81]) have been used to estimate the optical transition energies.

For applications exploiting SWCNT fluorescence, the quantum yield (QY) is of great interest as it directly determines the read-out signal intensity under given excitation conditions. The fluorescence QY of SWCNT, η , is defined as the ratio of the number of emitted photons to the number of absorbed photons [82]:

$$\eta = \frac{P_e \lambda_e S}{A P_i \lambda_i S_T} \quad (1.1)$$

here P_i , λ_i and S_T are the incident excitation laser power, wavelength, and spot area, respectively. A is the fraction of incident photons absorbed by nanotubes. P_e is the emission power from SWCNT, λ_e is the emission peak wavelength, and S is the surface area of SWCNT. The QYs of SWCNTs dispersed in surfactant were first estimated on

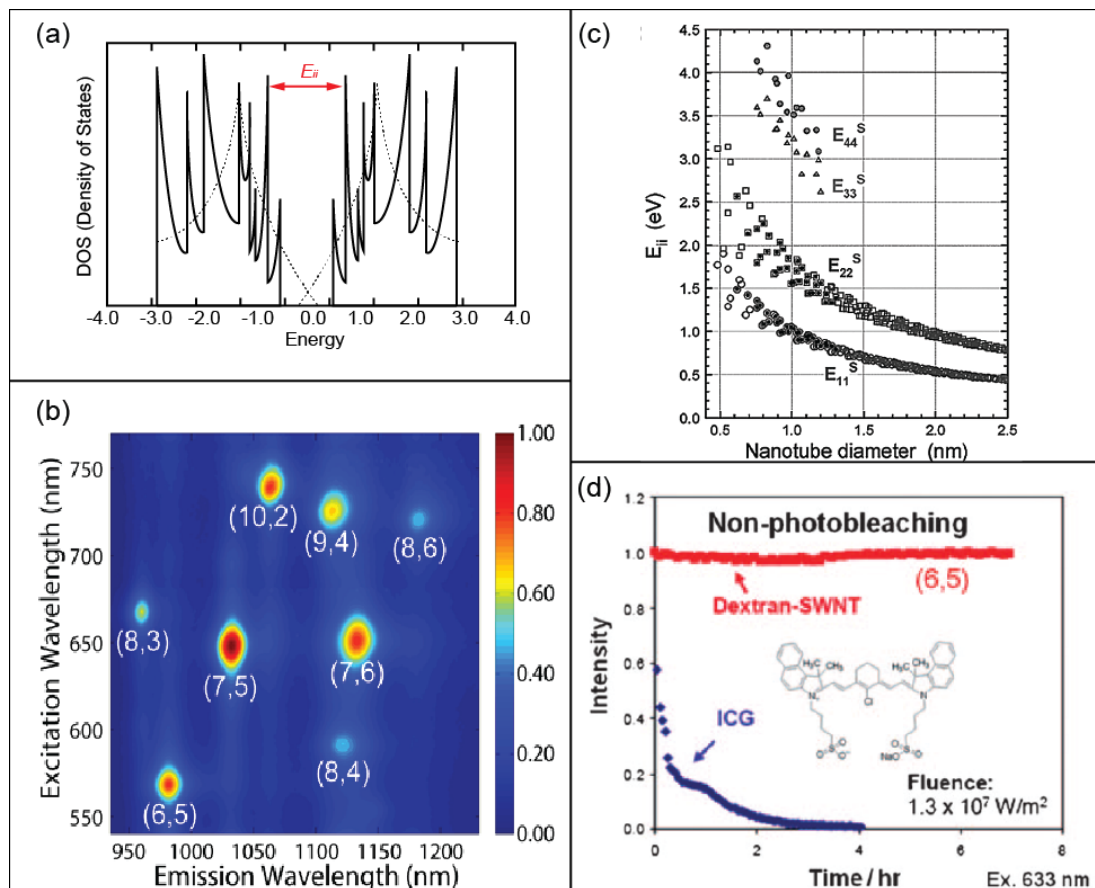


Figure 1.5. Optical properties of SWCNT. **(a)** Semiconducting SWCNT DOS. Sharp peaks shown in the plot are known as Van Hove singularities. The electronic transitions between DOS peaks (E_{ii}) show major optical absorption and emission energies calculated from an one-electron model [76]. The DOS for 2-D graphene (dotted line) is also shown. **(b)** 2-D PLE map of excitation and emission wavelengths of multiple SWCNT species in sodium cholate dispersed nanotubes. **(c)** Semiconducting SWCNT Kataura plot. Solid scatters are spectroscopic measurement data and open symbols are theoretical predictions of optical transition energies [75]. **(d)** Comparison of SWCNT and organic dyes photostability [77].

the order of $10^{-4} \sim 10^{-3}$ [78]. However, as only well-dispersed and undamaged SWCNT emit NIR fluorescence, the experimentally measured QY of a SWCNT sample can be highly dependent on its dispersion quality and purity. To overcome the difficulty in determining nanotube QY, density gradient ultracentrifugation (DGU) is applied to sort highly heterogeneous nanotube sample to single species. Crochet et al. [83] measured a highly concentrated individual (6,5) nanotube sample, which showed a QY of 1.1%. For single SWCNT suspended in air, the QY is determined to be $\sim 7\%$ [78, 82, 84].

Photobleaching and photoblinking are two major limiting factors for the application of organic fluorophores in long-term imaging and sensing. Photobleaching is the gradual decrease of fluorescence intensity over time due to continuous illumination. It significantly reduces the signal to noise ratio and data quality over long measurement time [85]. Photoblinking is the intermittency of fluorescence due to the trapping of electrons in long-lived triplet (dark) state, which leads to undesired fluctuations in optical signals. Compared to traditional fluorophores, SWCNT excels at its exceptional photostability (Figure 1.5d) [86–89]. Studies on the time trace of SWCNT fluorescence indicate constant PL up to 10 hours [86, 87]. Hartschuh et al. [89] reported a constant fluorescence intensity of single SWCNT on a time scale of 40 ms to 100 s at room temperature.

In addition to its photostability, SWCNT fluorescence is located at the so-called “biological window” (from 700 to 1800 nm), where absorption, scattering, and autofluorescence by tissues, blood, and water is minimal (Figure 1.6) [86, 93]. These optical characteristics render nanotubes a promising optical material for applications in biological environments.

1.1.3.2 Photophysics of Quantum Dot

The optical properties of QDs are modulated by its constituent material, structure, physical size and surface chemistry. Cadmium selenide (CdSe) and cadmium telluride

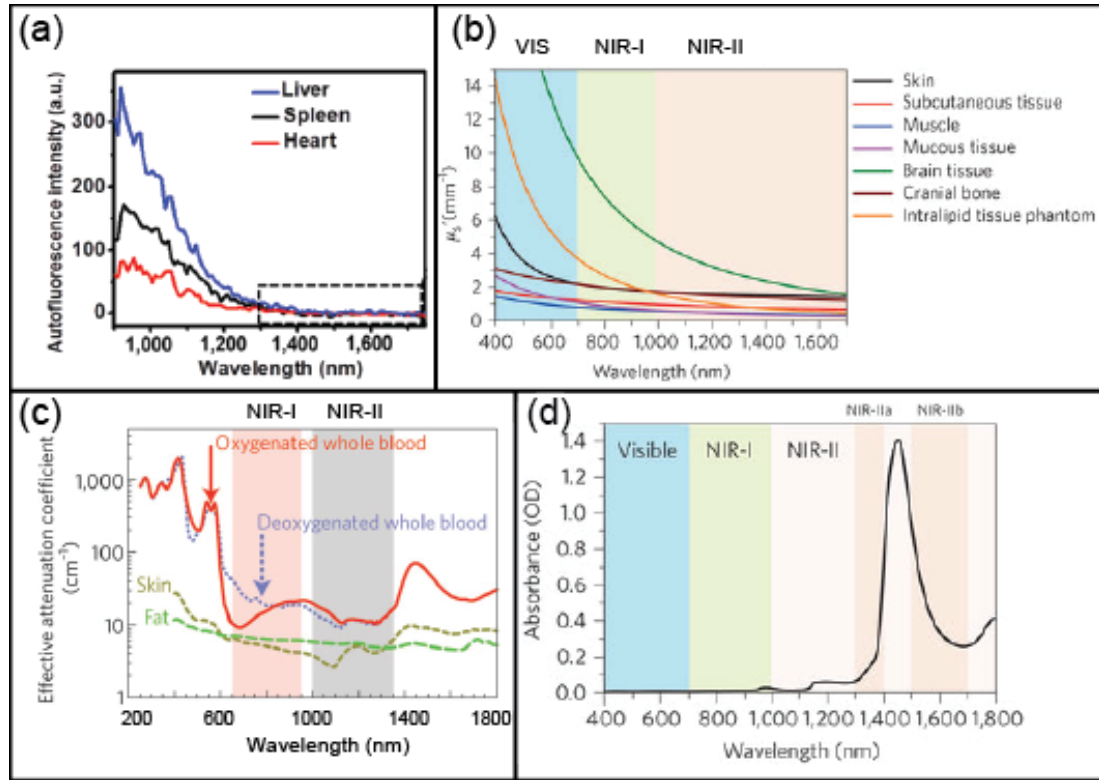


Figure 1.6. Optical properties of biological tissues and water in NIR. (a) Autofluorescence intensity [90]. (b) Scattering coefficient [91]. (c) Extinction coefficient [92]. (d) Water absorption [91].

(CdTe) are the most used types of QD for probing biological processes. They are selected primarily because of the ease of synthesis mono-disperse nanocrystals with desired optical properties [94].

Similar to SWCNT, QD is another type of low dimensional nanomaterial. Upon photo-excitation, excitons are confined in the small crystal lattice in all dimensions, thus tuning the exciton binding energy or the emission wavelength based on the size of the crystal [95]. The size dependence of emission and absorption of CdSe QD in water is shown in Figure 1.7a.

Photo-bleaching and emission intermittency have been observed in QD as a result of surface trapping states that prevent radiative recombination of excitons (Fig-

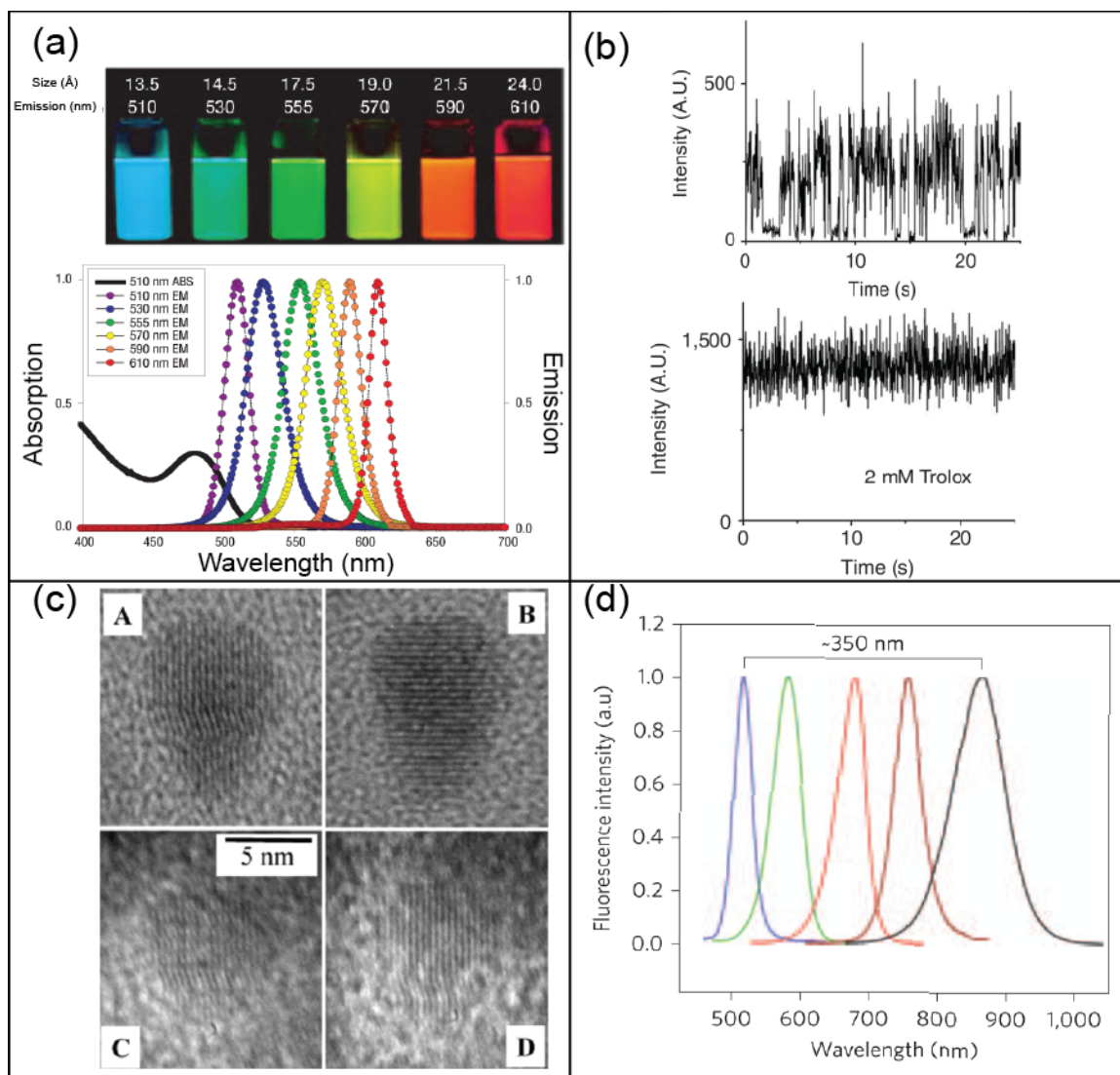


Figure 1.7. Optical properties of quantum dots. **(a)** Photograph and emission spectra of QD solution with different QD size. The change in emission wavelength is a result of quantum confinement effect [4]. **(b)** Top: emission intermittency (blinking) of a single QD. Bottom: addition of short thiol effectively suppress the blinking behavior by removing surface trapping state [96]. **(c)** TEM images of core/shell QD [97]. **(d)** QD emission wavelength tuning by lattice strain. The wavelength can be tuned from the visible to the NIR range [98].

ure 1.7b) [99]. To reduce the effects of surface hole traps, passivation layers such as zinc sulfide (ZnS) and cadmium sulfide (CdS) have been coated outside QD to form core/shell heterostructure QDs. When a thin layer of inorganic materials is coated onto QD, it prevents the exciton localized inside the core from escaping and becoming trapped at the QD surface (Figure 1.7b and c) [100–102] .

Core/shell heterostructure QDs have a wider tunability in its optical properties (Figure 1.7) [98,100]. The two different types of materials will induce lattice mismatch at the core/shell interface, which result in strains in the overall structure. The softer core is compressed by the shell. The strain in the core will raise the energy of its conduction band, resulting in a larger band gap energy. The quantum confinement effect, on the other hand, will decrease the energy of the conduction band for the shell structure. These two competing mechanism will determine the total energy of the radiative recombination, spanning the range of emission from visible to near-IR range [98].

1.2 Motivation

Natural biological systems use DNA to store genetic information that encodes various dynamic processes. Creating novel encoding schemes for dynamic processes using the same genetic material can fundamentally change the engineering of artificial systems. Synthetic nano-motor/walker serve as an ideal model system for experimenting oligonucleotide programmed dynamic processes. Molecular motors and walkers convert chemical energy from environment into mechanical motion. Its ability to actively locomote itself in an ever-fluctuating environment makes it a promising system in a wide range of applications [103–107]. Despite the research efforts in the community, synthetic nano walkers are still orders of magnitude slower than biological protein motors, which are optimized by evolution. Using DNA as building blocks to create mechanisms for molecular walkers allow programmatic controls of walker dynamics. Experimental and theoretical explorations on the engineering space and design prin-

ciples of DNA-based nanosystems will pave the road for creating synthetic systems that can ultimately rival natural molecular motors.

1.3 Scope of Study

This thesis focuses on creating synthetic systems consisting of optically active nanomaterials and programmable nucleotides. We explore using DNA chemistry to program the dynamic behavior of molecular systems. Two model synthetic DNA systems will be discussed: a highly specific molecular probe and an autonomous molecular walker. We use high-resolution optical methods to study the biophysical nature of DNA walkers and extract design principles for constructing high-performance walker systems. Regulation mechanisms for walkers are also explored to modulate their operation under different control signals.

1.3.1 Synthesis of DNA-based Nanosystems

Construction of an integrated system with nanomaterials and DNA requires interfacing techniques that minimize disturbance of the biochemical process under study. We design oligonucleotide strands that contain nanomaterial affinity region and functional region. The DNA strands self-assemble onto SWCNTs and QDs through the specific interaction between DNA and nanomaterial surface. The use of the DNA-SWCNT complex for the study of molecular recognition and transport is demonstrated and discussed.

1.3.2 Optical Nanoscopy

Optically visualizing nanoscale structure and motion provides useful information for studying detailed kinetic behavior of DNA walker systems. We combine the excellent optical properties of novel nanomaterials integrated into the walker system

with an advanced imaging platform and analysis algorithm to achieve sub-diffraction imaging resolution.

1.3.3 Biophysics of DNA Walkers

Displacement, velocity, and mean squared displacement (MSD) are extracted from fluorescence imaging and analyzed to reveal the nature of DNA walker translocation. Displacement fluctuations are analyzed to obtain walker stepping randomness and the rate-limiting steps in a single turnover event. The mean velocity under different experimental conditions are converted to reaction rates of each rate-limiting step. The scaling exponent of walker MSD is obtained to reveal the super-diffusive nature of the walker. Design principles are presented based on the insights in walker biophysics for the construction of a high motility and processivity DNA walker.

1.4 Organization

This thesis discusses experimental efforts in using of nucleotides to program molecular processes. Chapter 2 provides general experimental setups and sample preparation methods. The successful demonstration of an optically active DNA-SWCNT nanosystem and its application in the multiplexed detection of plasma porphyrins are presented in Chapter 3. The study of DNA walker kinetics and design principles using the DNA-SWCNT system is described in Chapter 4. Sub-diffraction characterization on the stochastic behavior of the DNA walker system is discussed in Chapter 5. The design and characterization of a multivalent DNA walker system that could power 2-D walking is presented in Chapter 6. Concluding remarks and future works are presented in Chapter 7.

2. METHODS

2.1 Single-walled Carbon Nanotube Functionalization

2.1.1 Nanotube Solubilization

Surfactant dispersed SWCNTs: Surfactant form micelles around nanotubes, separating otherwise aggregated SWCNTs in aqueous environments. Various surfactants were used in nanotube solution [108]. We use sodium cholate (SC) to solubilize nanotubes as they have a small aggregation number and form small micelle that can be easily removed. First, 0.6 g SC and 15 mg SWCNTs are mixed in 30 mL DI water, which gives 2 wt.% SC concentration for micelles formation. The mixture is probe sonicated in ice bath for 1 hr at 15 ~ 20 W to allow micelles formation around individually separated nanotubes. The sonicated sample is then ultracentrifuged for 4 hr at 30,000 rpm to remove unsolubilized bundles and impurities. The supernatant is separated from the centrifuge tube and stored in dark at -4 °C.

DNA dispersed SWCNTs: DNA nanotubes are prepared from SC solubilized nanotube by dialysis [109]. A 100 μ L aliquot of 1 mM DNA is mixed with 500 μ L of 10 mg/mL SC-SWCNTs in a 12-14 kDa molecular weight cut off (MWCO) membrane and dialysed against 2 L 1 \times TBS-EDTA (20 mM Tris, 100mM Na⁺, 0.5 mM EDTA, pH 7.4) buffer. A 24-hr dialysis period should be used to ensure surfactant exchange quality. During the dialysis, surfactants such as SC are removed from the solution so that micelles can no longer be maintained. DNA molecules, which have a MW larger than the cut-off size of the membrane, thus self-assembling onto the nanotube sidewall through $\pi - \pi$ stacking. To remove free DNA in the solution, a second stage dialysis is typically performed by replacing the 12-14 kDa membrane with 100 kDa membrane and dialysed for another 24 hr.

2.1.2 Length Fractionation by Molecular Crowding

To maintain a relatively uniform length distribution of the SWCNTs within a sample, length fractionation is performed after DNA functionalization. DNA-SWCNT are mixed with NaCl and PEG solution to make a final concentration of 4% PEG and 0.5 M NaCl. The mixture is incubated at 4 °C for 6 hr. After incubation, the mixture is centrifuged at 18,000 g for 15 min. The supernatant which contains short nanotube (~ 100 nm) is removed. The pellets are redispersed in 3% PEG and 0.5 M NaCl. The same incubation, centrifugation, re-dispersion procedure is repeated with decreasing PEG concentration from 3% to 2% and finally 1%. The supernatant containing nanotubes with increasing lengths are separated and imaged using AFM (Figure 2.1). The correspondence between PEG concentration and nanotube lengths is determined: 4% PEG: 100 nm SWCNTs; 3% PEG: 300 nm SWCNTs; 2% PEG: 500 nm SWCNTs; 1% PEG: 500 \sim 1,500 nm SWCNTs.

2.2 DNA Assisted Nanocrystal Growth

DNA capped CdS QD: Mix 30 μ L of 1 mM DNAzyme solution and 120 μ L of 5 mM CdCl₂ solution. Add 60 μ L of 5 mM Na₂S and 100 μ L of 1 \times TBS (20 mM Tris, 100mM Na⁺, pH 7.4) buffer is added with vigorous stirring to initiate the nucleation of nanocrystals. Upon Na₂S addition, the solution will turn light yellow. The molar ratio between the precursors are DNA: Cd²⁺: S²⁻ = 1: 20: 10. The solution is then incubated at 150 rpm for 6 hr in dark. The incubation process allows the nucleated CdS nanocrystal growth, which is important for uniform particle size. As-synthesized particles are purified by a non-solvent method to remove excess precursors and DNAzymes. Equal-volume 300 μ L each) of 3 M NaCl solution and isopropanol are mixed with the QD solution. The mixture is centrifuged at 20,000 rpm for 10 min to precipitate DNA-QDs. After removing supernatant, the yellow pellet is re-dispersed by 30 s bath sonication in 100 μ L 1 \times TBS buffer.

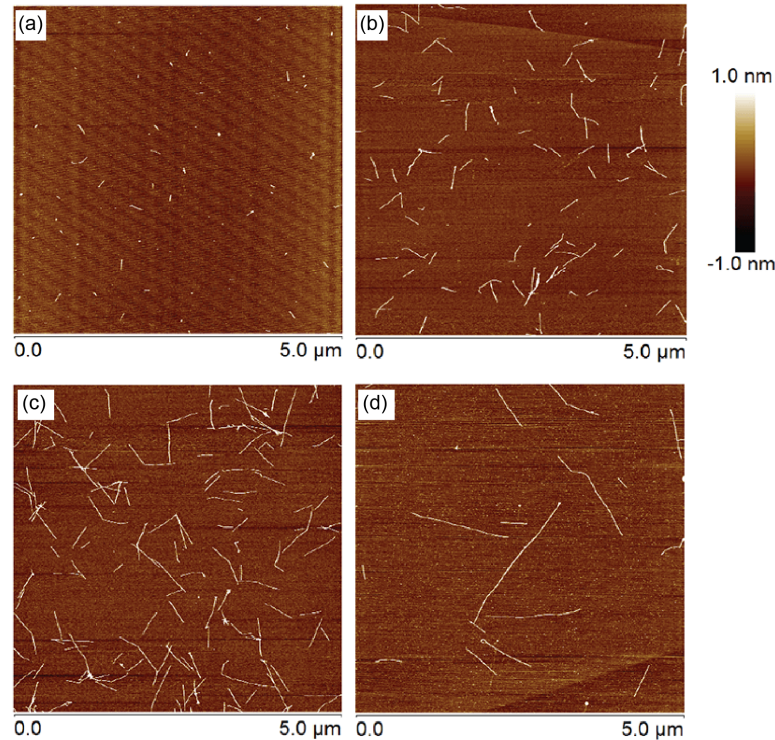


Figure 2.1. AFM characterization of length sorted D/RNA-SWCNTs. **(a)** 4% PEG: 100 nm SWCNTs; **(b)** 3% PEG: 300 nm SWCNTs; **(c)** 2% PEG: 500 nm SWCNTs; **(d)** 1% PEG: 500 ~ 1500 nm SWCNTs.

DNA capped CdTe/CdS QD: Aqueous synthesis of QD nanocrystals with excellent quantum yield and photo-stability have been reported previously [110–112]. We modified those synthesis routes to generate DNAzyme functionalized CdTe/CdS nanocrystal QDs. CdTe core with 2 nm diameter was first synthesized using NaHTe and $\text{Cd}(\text{NO}_3)_2$ as precursors and mercaptopropionic acid (MPA) as capping ligand. Tellurium precursors are made by adding 25 mg sodium borohydride (NaBH_4) and 40 mg Te powder in 2 ml DI water. The mixture is left overnight with N_2 gas protection to yield NaHTe solution. Cadmium precursors are prepared by adding 150 μL MPA into 200 ml 5 mM $\text{Cd}(\text{NO}_3)_2$ solution. The pH of the mixture is adjusted to 12.2 using NaOH titration. Cadmium and Tellurium precursors are mixed by adding 400 μL NaHTe solution to 200 ml $\text{Cd}(\text{NO}_3)_2$ -MPA solution after 10 min N_2 purging. The

mixture is left at 4 °C overnight for the formation of 2 nm CdTe core. We have found that commercially available carboxylated CdTe core type QD can also be used for core/shell structure QD synthesis. The synthesized core was subsequently purified by using 3 M NaCl and methanol as non-solvent and centrifuged at 20,000 RPM for 10 min. CdS shell was grown epitaxially over the CdTe core by heating a mixture of 100 μ L core solution, $\text{Cd}(\text{NO}_3)_2$ -MPA and phosphorothioated DNAzyme strands. CdTe/CdS QDs with 3 nm diameter (Figure 2.2a and b) and emission peak at 700 nm will form after 70 min heating time. The synthesized QDs were purified using a 30 kDa column filtration (Amicon) for 4 times. The emission from QDs are highly stable in $1\times$ PBS and 20 mM DTT (Figure 2.2c). Approximately 1000 photons from a single QD can be collected using 1s integration time (Figure 2.2d).

2.3 Nanometric Characterization

2.3.1 AFM Imaging

The structure of DNA functionalized SWCNTs and QDs can be visualized by AFM after deposition onto mica surface. The target sample is deposited onto freshly cleaved mica surface with equal volume of $1\times$ TAE (20mM Tris, 0.5 mM EDTA, pH 7.4) buffer containing 12.5 mM Mg^{2+} . The mica surface is incubated with the sample solution for 5 min. After incubation, the surface is washed by adding 90 μ L DI water and dried with compressed air. Most AFM images are captured by Bruker Dimension Icon AFM with peak force tapping imaging in air.

2.3.2 Spectral Characterization

Absorption: All absorption is measured by PerkinElmer Lambda 950 UV/VIS/NIR spectrophotometer. For oligonucleotides functionalized SWCNTs, optical density (OD) at 632 nm is used to determine its concentration with the extinction coefficient of $0.036 \text{ OD mL } \mu\text{g}^{-1} \text{ cm}^{-1}$. Oligonucleotide concentration is de-

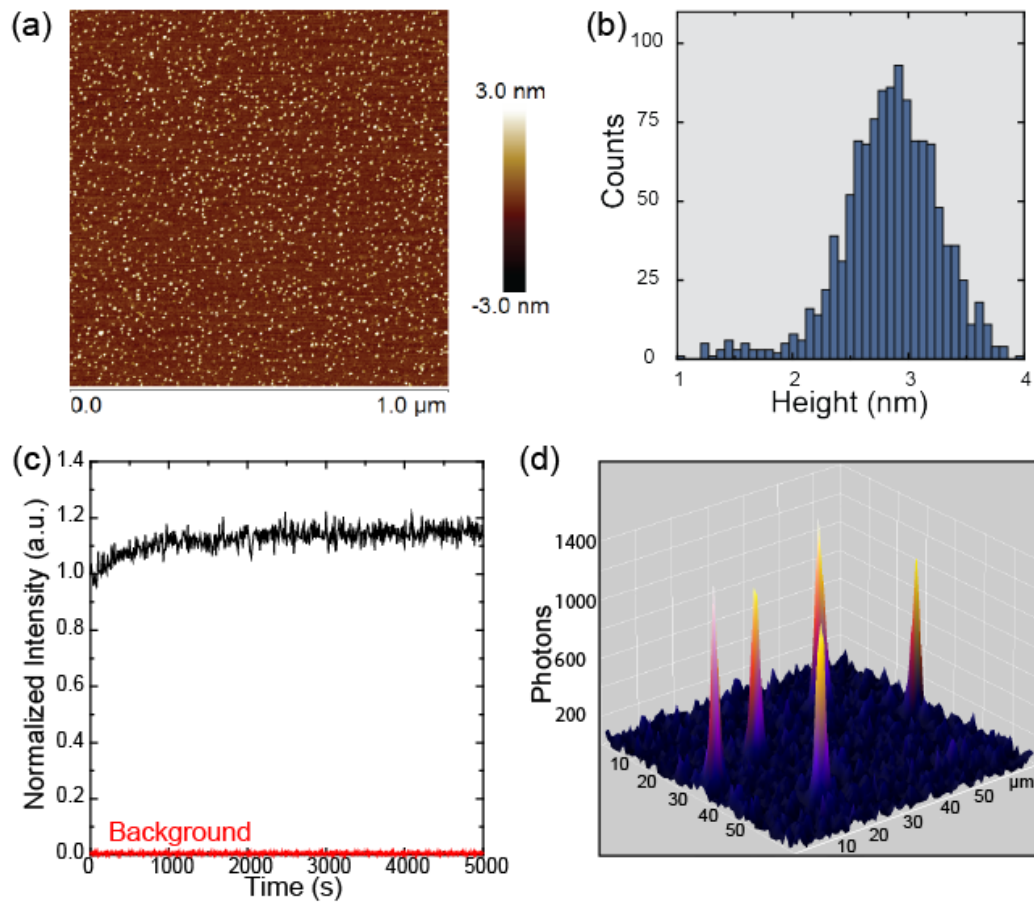


Figure 2.2. Characterization of CdTe/CdS QD size and optical properties. **(a)** An AFM image of a large number of QDs deposited onto a flat Mica surface. **(b)** QD size distribution extracted from the height profile of the AFM image. **(c)** Photostability of CdTe/CdS core/shell QD. The QDs are diluted with $1\times$ PBS and 20 mM DTT. Time trace of the emission is measured by a fluorometer with 0.1s integration time and 1s measurement interval. **(d)** Photon counts of the QDs obtained from a microscope image. The QDs are immobilized to the imaging surface in a flow channel with $1\times$ PBS and 20mM DTT. Typical emissions from QDs are ≈ 1000 photons at 1s integration time. The background intensity has a standard deviation of 50 photons.

terminated by measuring OD at 260 nm after subtracting SWCNT absorption background. Nucleotide-SWCNTs display red-shifted optical signatures compared to SC-SWCNTs [113], which are used to confirm the successful replacement of SC on the nanotube surface by oligonucleotides.

The concentration of QDs is characterized by the optical absorption of the first excitonic transition based on the correlation proposed by Peng et al [114]. The number of DNAzymes per CdS nanoparticle is determined by the concentration ratio of DNA/QD.

Photoluminescence: Photoluminescence is measured by a Jobin Yvon Fluorolog-3 fluorometer with a photomultiplier tube and a N₂-cooled InGaAs detector. A Xenon lamp is used for excitation. SWCNTs with different chirality, have distinct emission signatures [80]. The prevalent SWCNT species in the sample are identified by measuring the PLE spectra. A 800 nm long pass filter is placed before the photo-detector to filter excitation light. QDs with different diameters and structures are excited with a 405 nm laser. Its emission is filtered by a 500 nm long pass filter before photo detector.

2.3.3 Fluorescence Imaging

Optical Setup: Visible (Andor iXon 3 EMCCD) and near-IR (Princeton Instrument OMA V) cameras are connected to two exit ports of a microscope stand (Zeiss Axio Observer D1) to image the QDs and SWCNTs from two different spectral channels. The EMCCD features an 512×512 array of 16 μm sized pixels. Electron multiplication boosts the sample signal compared to the readout noise. The NIR camera features a 320×256 2-D array of 30 μm sized pixels. The camera is cryogenically cooled to minimize thermal noise. The two cameras are aligned through a stage micrometer before each experiment. The XY translation, rotation, and scaling are recorded as a transformation matrix for use throughout one experiment. Two lasers (500mW@658nm and 120mW@405nm, both from Laser glow) are coupled to the mi-

croscope stand through optical fibers. Excitation clean-up filter, dichroic mirror and emission filter are placed in a filter turret inside the microscope stand. Other optics are placed outside the stand for customization in each experiment (see Methods section in each chapter for specific setups). A piezo actuated stage capable of 1 nm XY displacement precision (Physik Instrumente P517) is mounted below sample stage for calibrating imaging precision. A 63 \times plano-achromat oil immersion objective lens with N.A. 1.4 is used for imaging. All equipments are connected to a computer and are controlled by μ manager.

Flow Channel Assembly: A multi-channel flow cell is assembled for imaging experiments as shown in Figure 2.3a. Quartz slides, fluorescence glass coverslips (Schott), and medical grade acrylic adhesive sheets (Adhesive Research) are used for flow channel assembly. Multiple 2 mm wide flow channels are cut out on the adhesive sheets using an electronic cutter (Silhouette Curio). The cut adhesive piece is then sandwiched between the slide and coverslip. Inlet and outlet ports (LabSmith) are then bonded to the slide using epoxy. Tygon microbore tubings are used to connect sample tubes and the flow channel.

Imaging Surface Preparation: The coverslips are passivated before channel assembly to prevent non-specific interactions between the walker system and the glass surface [115]. The coverslips are first thoroughly washed in DI water and methanol for 20 min. The washed coverslips are then activated by hydroxylating the surface in Piranha solution for 1 hr. This process increases the percentage of surface silanol groups to achieve a higher degree of passivation. The activated coverslips were then immersed with 0.1 vol% dichlorodimethylsilane (DDS) in hexane and sonicated for 1 hr. The passivated surfaces were stored in -20 °C and used within a month.

Before each experiment, 100 μ L of 0.5 mg/mL biotinylated-BSA solution was first introduced into the flow channel and incubated for 10 min. After BSA incubation, 100 μ L 0.2 vol% Tween 20 solution was introduced into the flow channel and incubated for another 10 min. The surfactant Tween 20 self-assembled onto the DDS surface and forms a passivation layer. The Tween 20 solution is then washed out by 100

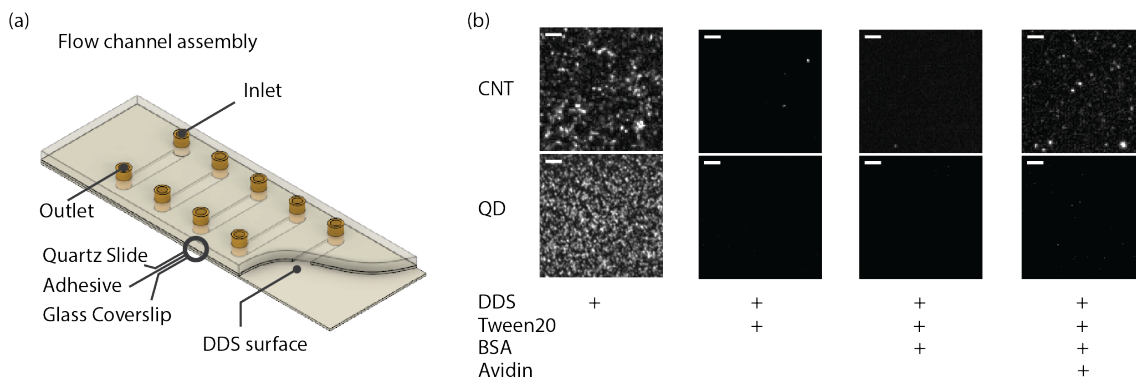


Figure 2.3. Flow channel assembly and surface characterization. **(a)** Schematic of the flow channel. The channels are cut in adhesive tapes. Imaging surfaces are first treated with a layer of dimethyldichlorosilane (DSS) grafted onto its surface. The channel array is then sandwiched in-between coverslip and slide. Connector ports are attached to the slides to form inlets and outlets. **(b)** Surface passivation characterization. First column: QDs and SWCNTs uniformly adsorb onto the DSS surface without any blocking buffer. Second and Third column: Tween 20 and biotinylated BSA adsorbs onto the DSS surface and form a blocking layer to prevent non-specific adsorption of QDs and SWCNTs. Fourth column: with the presence of streptavidin, biotinylated RNA functionalized SWCNTs specifically adsorb onto the surface. QDs are still repelled by the surface. The scale bars are 5 μm for all images.

μL PBS (pH 7.5) buffer. After washing, 100 μL 10 $\mu\text{g}/\text{mL}$ streptavidin solution was flowed into the channel and incubated for 5 min. The effects of surface passivation at the presence of biotinylated-BSA and streptavidin are shown in Figure 2.3b.

3. PROBING MOLECULAR INTERACTIONS

3.1 Introduction

The chemical properties and biological functionalities of oligonucleotides are highly programmable. Integrating such programmable biomaterials with nanomaterials allow engineering of systems with designed properties and functions. In this chapter, we demonstrate using synthetic short oligonucleotide strands to modulate the molecular interaction between carbon nanotube and porphyrins.

As mentioned in the previous chapters, SWCNTs are exceptionally photostable fluorophores that emit in the near infrared range. Their novel optical properties make them promising materials for building molecular probes [86, 116, 117]. However, their large aspect ratio and mostly inert surface chemistry limit their applications. Pristine nanotubes are not soluble in aqueous environments and are highly heterogeneous in structures, electronic and optical properties. On the other hand, the π electron rich graphitic lattice on nanotube sidewall allow non-covalent interaction with other π electron rich systems, such as nucleotides or pyrene [93]. Based on this property, we functionalize carbon nanotubes with a specific type of functional DNA sequence known as aptamers.

DNA aptamers are short oligonucleotides that can specifically bind to certain molecules. These sequences are identified from a process termed “Systematic Evolution of Ligands by Exponential Enrichment” (SELEX). They are capable of recognizing a broad range of molecules with high binding affinity, excellent stability, and are compatible with biological environments. Thus, aptamers have been considered promising target recognition molecules alternative to antibodies for molecular sensing applications [118]. DNA strand containing a previously identified heme binding

sequence [119] and a nanotube affinity region is used in this chapter to functionalize SWCNTs for multiplexed detection of plasma porphyrins.

Porphyrin is a common cofactor found in many proteins. In particular, an iron-containing porphyrin heme (FePP) plays critical roles in widely diverse biological processes [120,121]. The biosynthetic pathway of heme (or FePP in this study) relies on the interplay of several enzymes, which convert small molecules into pyrrole ring structures and produce intermediate porphyrin species along the way. Three intermediate species, protoporphyrin (PP), coproporphyrin (CP), and uroporphyrin (UP), are the most commonly found porphyrins in blood [121]. Disorders of blood porphyrin concentration bear significant diagnostic and therapeutic values for diseases such as porphyria and sideroblastic anemia [122]. Porphyrins are also optically active molecules due to the π electrons in the pyrrole ring structure. They exhibit strong absorption at approximately 400 nm (Soret band) and 550 nm (Q band) and bright emission at 600~700nm. These signatures arise from $\pi - \pi^*$ transitions between the highest occupied molecular orbitals (HOMOs) and lowest unoccupied molecular orbitals (LUMOs) [123]. The external and internal substitutions of atoms in the pyrrole ring alter porphyrin electronic structures, resulting in different optical properties among species.

The optical properties of porphyrins can be used to quantify their concentration in solution. However, intermediate porphyrin species during biosynthesis have similar optical properties, which results in the overlap of their optical spectra and makes it difficult for optical measurement [121]. To quantify different species of porphyrin in blood, current methods use solvent extraction or high-performance liquid chromatography (HPLC) to separate each porphyrin type for measurement [124,125]. However, blood porphyrins bound to plasma proteins with high affinity. Traditional solvent extraction produce inadequate separation and renders the test susceptible to errors [122,124,125]. HPLC separation is usually used for analyzing urine porphyrins, but not suggested for blood porphyrin tests [125,126]. Thus analytical platform ca-

pable of differentiating closely related porphyrin species in plasma for multiplexed quantification will be a useful tool for both scientific and clinical purposes.

Although the interactions of porphyrin-DNA and porphyrin-SWCNTs have been extensively studied, few studies have explored interactions between porphyrins and DNA functionalized SWCNTs [127,128]. Here, optical transduction signals are exploited to probe the interaction between the aptamer-SWCNTs (a-SWCNTs) complex with four biologically important porphyrins, heme (FePP), protoporphyrin (PP), coproporphyrin (CP), and uroporphyrin (UP). The observed optical signatures show two interaction mechanisms, specific binding and non-specific adsorption between porphyrins and a-SWCNTs. The optical signals from these two mechanisms are combined to formulate a multiplexed sensing scheme for all four types of porphyrin species in human plasma sample. Our strategy is selective and sensitive, which offers novel analytical tools for molecular sensing and engineering.

3.2 Scheme

The sensing approach exploits optical absorption and fluorescence signals for multiplexed quantification of the four porphyrin species commonly found in blood using a-SWCNTs (Figure 3.1). FePP-binding aptamer is used to solubilize and decorate SWCNTs while retaining the aptamer's target recognition ability [129]. As all four types of proteins have similar structures, we postulate they will interact with the a-SWCNTs with varying strength. The affinity between aptamer and its target brings porphyrins close to nanotube surface, which results in the perturbation of the π electron systems on both nanotube and porphyrins. We have discovered that FePP quenches a-SWCNTs fluorescence via a photo-excited state charge transfer mechanism, while other porphyrins with similar structures do not. In parallel, a-SWCNTs serve as effective quenchers of PP fluorescence but have little impact on other fluorescent porphyrins. We exploits these differences to distinguish each porphyrin species (Figure 3.1 bottom). FePP concentration is determined from its selective quenching

of a-SWCNTs emission. PP concentration is correlated to the fluoresce quenching of porphyrin mixture by a-SWCNTs. With FePP and PP concentration determined, CP and UP concentrations are then directly calculated from their absorption.

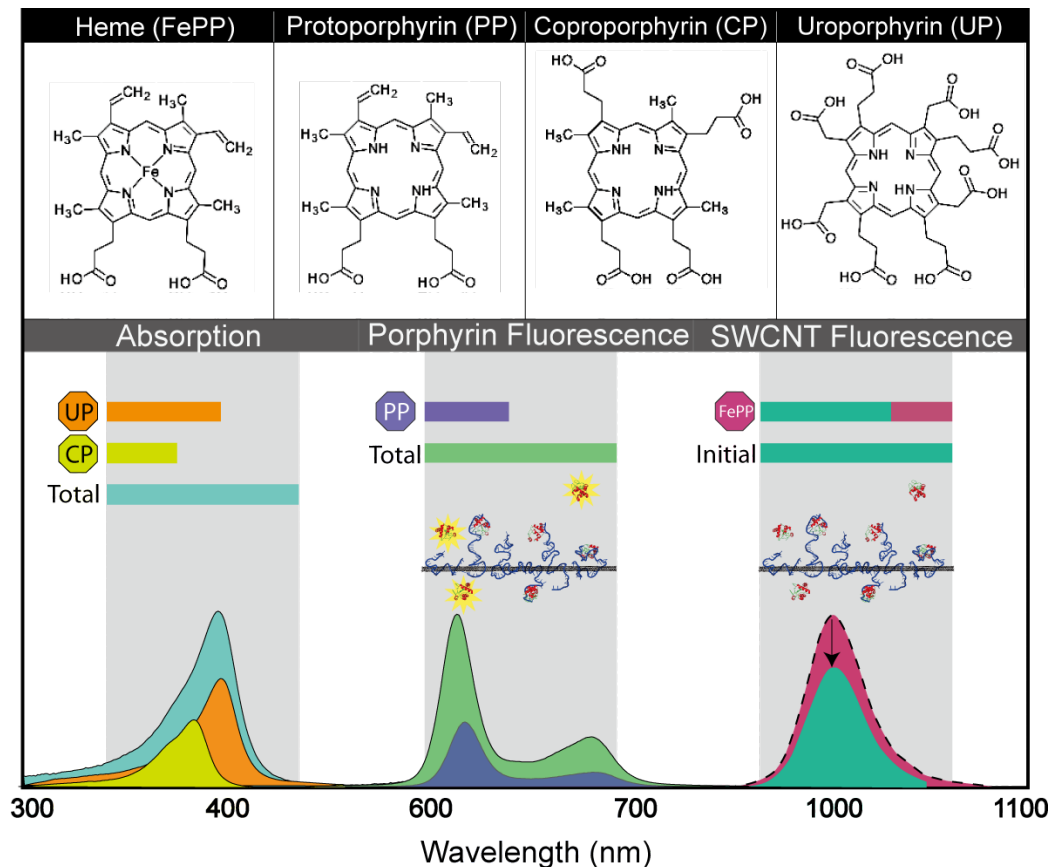


Figure 3.1. Overview of porphyrin structures and sensing scheme. Top: chemical structures of porphyrins species in heme biosynthesis. Bottom: multiplexed optical quantification scheme for the 4 porphyrins species. The quenching of a-SWCNT fluorescence relates to FePP concentration. PP concentration is determined by fluorescence quenching of porphyrin mixture. CP and UP concentrations can be calculated from their Soret band absorption.

3.3 Methods

All chemicals were purchased from Sigma-Aldrich unless otherwise specified. Coproporphyrin III tetramethyl ester was obtained from Frontier Scientific. CoMoCAT SWCNTs were purchased from Southwest Nano-technology. Sodium cholate was obtained from Affymetrix Inc. The heme aptamer sequence (5'-AGT GTG AAA TAT CTA AAC TAA ATG TGG AGG GTG GGA CGG GAA GAA GTT TAT TTT TCA CAC T-3') and human telomere DNA (5' -AGG GTT AGG GTT AGG GTT AGG GTT-3') were custom-synthesized from IDT. Deionized water ($>18.2\text{ M}\Omega$, ThermoScientific) was used in all aqueous solutions. 1X TBS buffer (20mM Tris, 100mM NaCl, 20 mM KCl, pH 8.0) was used as the standard buffer unless otherwise specified.

3.3.1 Porphyrin Stock Preparation

Porphyrin stock solutions were prepared by dissolving porphyrin powders in dimethyl sulfoxide (DMSO, spectral grade). The stock solution concentration was determined by measuring the absorbance at its corresponding Soret peak followed by dilution to 1 mM. The molar extinction coefficients ϵ for each porphyrin are as follows: FePP ($1.83 \times 10^5\text{ M}^{-1}\text{ cm}^{-1}$), PP ($1.71 \times 10^5\text{ M}^{-1}\text{ cm}^{-1}$), UP ($2.17 \times 10^5\text{ M}^{-1}\text{ cm}^{-1}$), and CP ($1.8 \times 10^5\text{ M}^{-1}\text{ cm}^{-1}$) [130, 131].

3.3.2 Aptamer-SWCNTs Synthesis

CoMoCAT carbon nanotube was functionalized by DNA aptamer strands using the same method as described in Chapter 2. A 61-nt, FePP-binding aptamer was used to functionalize nanotube [129]. This aptamer sequence binds to its target (FePP) with a dissociation constant of $K_d \sim 1\text{ }\mu\text{M}$, but has lower binding affinity with porphyrins of similar structures. FePP binds to the guanine (G)-quadruplex of the oligonucleotide with a stoichiometry of one FePP per aptamer

strand [129, 132]. The concentrations of DNA and SWCNTs were evaluated by measuring the absorption at 260 nm ($\epsilon_{DNA} = 6.19 \times 10^5 \text{ M}^{-1} \text{ cm}^{-1}$) and 632 nm ($\epsilon_{SWCNT} = 3.6 \times 10^3 \text{ L mg}^{-1} \text{ cm}^{-1}$). The number of DNA aptamer strands per nanotube was determined by comparing the molar concentration ratio of DNA to nanotube.

3.3.3 Optical Measurements

Porphyrins absorption spectra with and without aptamer or a-SWCNTs were obtained by first measuring the absorption of 0.5 μM porphyrin solution in buffer, followed by addition of aptamer and a-SWCNTs. DNA or nanotube absorption spectra, which was measured separately with the same concentration, was subtracted from porphyrin spectra to obtain the correct absorption only from porphyrin. The visible porphyrin fluorescence spectra and NIR a-SWCNT emission were measured with Horiba Jobin Yvon Fluorolog-3 fluorometer. The InGaAs array was first cooled cryogenically and the Xenon lamp was allowed to warm up for 30 min before each experiments. The integration time for visible and NIR measurements were 0.1 s and 0.5s, respectively. The slit widths of excitation and emission were 10 nm for both visible and NIR measurement. All dilution effects were corrected after data acquisition.

3.3.4 Porphyrin Characterization

The extinction coefficient of porphyrins in aqueous buffer were compared with porphyrins in DMSO. Molar extinction coefficients for porphyrins at 391 nm are determined as follows: $\epsilon_{391} = 4.7 \times 10^4 \text{ M}^{-1} \text{ cm}^{-1}$ for FePP, $\epsilon_{391} = 4.1 \times 10^4 \text{ M}^{-1} \text{ cm}^{-1}$ for PP, $\epsilon_{391} = 9.3 \times 10^4 \text{ M}^{-1} \text{ cm}^{-1}$ for CP, and $\epsilon_{391} = 9.8 \times 10^4 \text{ M}^{-1} \text{ cm}^{-1}$ for UP. The wavelength 391nm was chosen as it is the isosbestic point for CP and UP. Excitation at 400 nm is used for fluorescence measurements.

3.3.5 Porphyrin Mixture Quantification Procedure

Porphyrin mixture solution was prepared by diluting porphyrin stock solution with 1X Tris buffer to the desired concentration: 0.2 μ M FePP, 0.2 μ M PP, 0.1 μ M CP, and 0.1 μ M UP. The fraction of porphyrins were experimentally quantified using the steps described below. First, the FePP concentration in mixture was determined by measuring a-SWCNT fluorescence quenching when 5 μ L a-SWCNT solution was added to 115 μ L porphyrin mixture solution. A-SWCNT sample was excited at 658 nm and emission measured at \sim 1040 nm, which corresponds to (7,5) nanotube fluorescence signature. Second, the PP concentration was estimated from difference spectrum of mixture fluorescence before and after excess amount of a-SWCNT addition (a-SWCNTs/porphyrin = 20:1). Excitation at 400 nm was used. Last, absorption spectrum of the mixture solution was recorded. Based on the known concentrations of FePP and PP, the amount of CP and UP could be estimated after subtraction of FePP and PP absorption from the measured spectrum. Dilution effects were corrected after data acquisition.

3.3.6 Plasma Porphyrin Extraction Procedure

Approximately 200 μ L of plasma containing 20 μ M porphyrins was mixed with 200 μ L of extraction solution (20 mM Tris, 100 mM NaCl, 20 mM KCl, 5.5 wt.% trichloroacetic acid (TCA) and 50 vol.% DMSO). The mixture was centrifuged at 15,000 rpm for 30 min and the pellet was removed. The porphyrin containing supernatant was adjusted to pH 8.0 with 1 M NaOH and used as stock solution. Extraction coefficients of 85% are estimated for UP and CP and 80% for PP [121].

3.4 Results and Discussion

3.4.1 Optical Modulation of a-SWCNTs

Figure 3.2a shows the NIR emission spectra of carbon nanotubes interacting with porphyrins. The (7,5) nanotube fluorescence quenched upon the addition of FePP solution (red to black), whereas such emission quenching was not observed with the other three porphyrins. Here, the molar ratio of porphyrins to DNA strands on SWCNTs was roughly 1:5. The selectivity of the nanotube emission quenching was examined with various analytes such as bovine serum albumin (BSA) and lysozyme, which have negative and positive overall charges at the given pH 8 (isoelectric point at 4.8 and 9.3, respectively), as well as anionic phthalocyanines (Figure 3.2b). The proteins and phthalocyanines did not quench a-SWCNT fluorescence, while FePP addition to the mixture solution immediately resulted in signal transduction, indicating good selectivity of the aptamer-SWCNT hybrids. The SWCNT fluorescence quenching, while no significant changes were observed in nanotube absorption, can be explained by an excited state charge transfer mechanism [133]. The presence of the iron atom in the center of porphyrin ring provides charge transfer (CT) states energetically lower than its Q band, thus exhibiting no radiative recombination for FePP [134]. Since the redox potential of FePP is located in between those of the SWCNT valence and conduction bands [135], the charge transfer from SWCNT conduction bands to the CT states in FePP is attributed to the nanotube emission quenching [133]. However, the lack of CT states in PP [133,134] brings about unperturbed electronic transitions in a-SWCNTs.

3.4.2 Optical Transduction of Porphyrins

To further investigate the porphyrin/a-SWCNT interactions, we examined optical signal transduction of porphyrins. Figure 3.3 shows the absorption and fluorescence spectra of the four porphyrins (black), after aptamer addition (red), and after a-

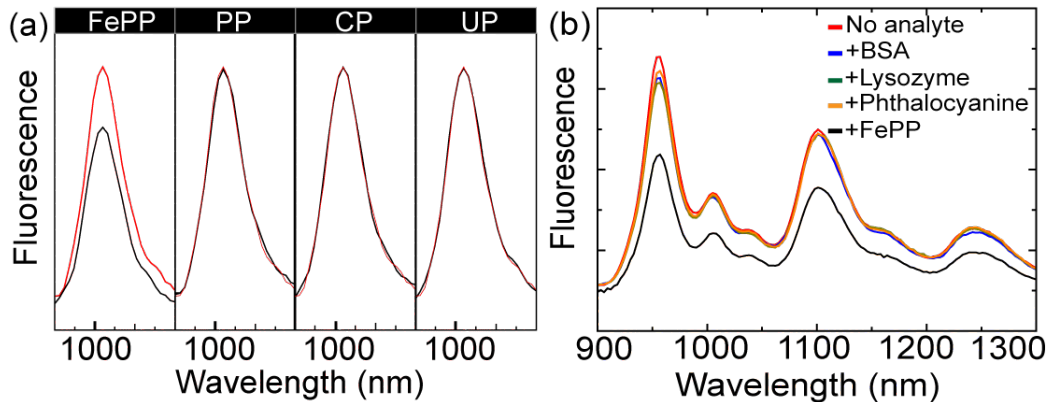


Figure 3.2. Nanotube emission quenching by porphyrins. **(a)** The emission of (7,5) SWCNTs (Excitation 658 nm) before (red) and after (black) the addition of porphyrin. The ratio between DNA and porphyrin is 5:1. **(b)** Selective a-SWCNT fluorescence (excitation 567nm) quenching by FePP. No significant decrease in the nanotube fluorescence intensity was observed with the addition of BSA, lysozyme, and phthalocyanine (analyte:DNA = 1:5). Upon FePP addition, nanotube fluorescence dropped immediately. All the experiments were carried out in 1X Tris buffer and the dilution effects are corrected.

SWCNT addition (blue), where the porphyrin to DNA ratio is kept constant at 1:1. The presence of DNA and a-SWCNTs did not modulate the optical signatures of CP and UP, indicating weak or no interactions. The lack of interactions is attributed to the negatively charged carboxyl groups at the porphyrin peripheral as they bring about better water solubility and less tendency to interact with anionic a-SWCNTs hybrids. In contrast to UP and CP, the absorption and fluorescence spectra of FePP and PP show strong evidence of interaction with aptamer DNA as well as a-SWCNTs. Figure 3.3a shows that FePP exhibits broad absorption features from 350 to 400 nm (black), which indicates the presence of both dimers and monomers in aqueous solution [130]. In comparison, FePP monomers alone show a sharp Soret peak at approximately 400 nm. The addition of aptamer DNA in FePP aqueous solution induced hyperchromic and bathochromic shifts in FePP absorption (black to red), recovering its Soret band features as monomers. This spectral change indicated that

the majority of the FePP dimers were separated into monomers while interacting with aptamer. Similar hyperchromic and bathochromic shifts were observed with PP interacting with aptamer (DNA/PP=1:1), but more aptamer strands were required to achieve comparable separation into monomers (DNA/PP=5:1, red to pink). This difference is due to the lower affinity between the aptamer and PP. Addition of a-SWCNTs to the FePP solution followed a pattern that was similar to the addition of aptamer, but with notably broader Soret peak and decreased intensity. The addition of a-SWCNTs to PP solution (DNA/PP=1:1) resulted in a broader peak at longer wavelength (blue) compared to the addition of aptamer only (red). Increasing the a-SWCNTs to PP ratio from 1:1 to 5:1 (blue to green) had little effect on the Soret peak features.

From these observations, we propose two interaction mechanisms between porphyrins and a-SWCNTs: (1) specific binding via aptamer DNA and (2) non-specific adsorption on a-SWCNTs. Firstly, the aptamer strands on SWCNTs provide a hydrophobic environment as a specific binding site for FePP and PP to separate porphyrin dimers, and thereby giving rise to the better resolved Soret band signatures. We previously observed transfer interactions between porphyrins and nanotubes through intercalated DNA, which were used for photocurrent generation [127]. Secondly, porphyrins may also adsorb onto SWCNTs non-specifically through $\pi - \pi$ stacking, resulting in a broad Soret peak at 420 nm [136]. The prevalence of the two interaction mechanisms is determined by the affinity between porphyrins and the aptamer sequence. Upon a-SWCNTs addition, monomer Soret peak features are observed more prominently for FePP compared to PP as a result of higher affinity. These results suggest that the specific binding mechanism is favored for FePP, while the non-specific, π -interaction is more probable for PP. A control experiment replacing the aptamer with another DNA sequence (24-base-long human telomere in this case) shows no significant Soret band changes after DNA addition as a result of poor affinity for both FePP and PP Figure 3.4. However, broad absorption peaks at ~ 420 nm were observed with both porphyrins after human telomere DNA-SWCNTs

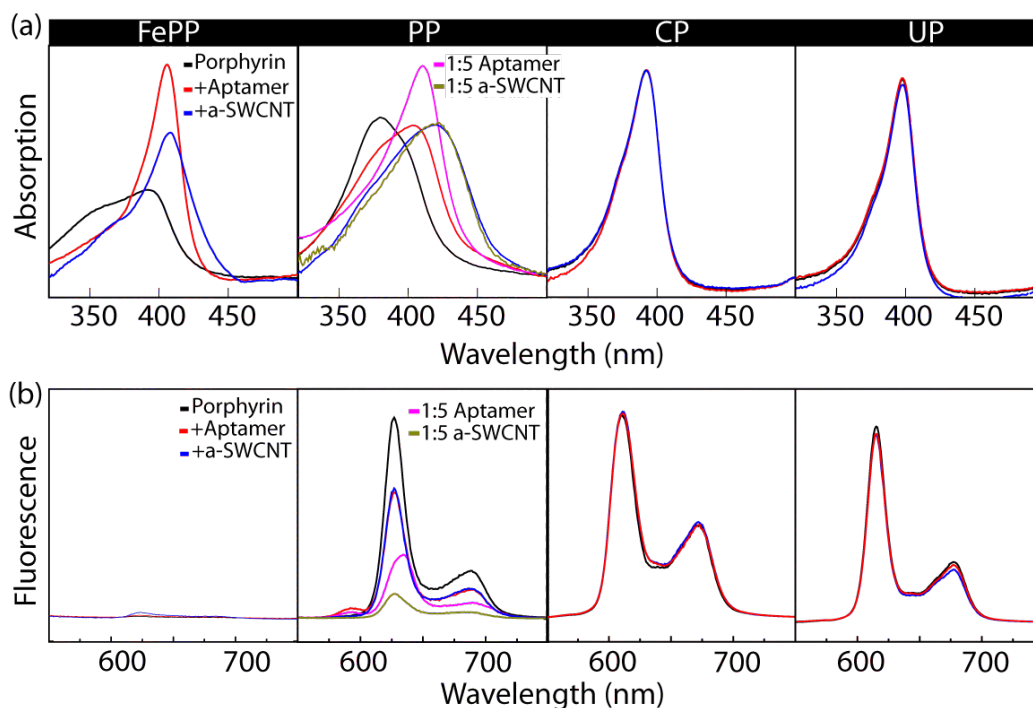


Figure 3.3. Optical signature of porphyrins/aptamer/a-SWCNTs interaction. **(a)** Porphyrin absorption spectra before (black) and after aptamer (red) or a-SWCNTs (blue) addition. Only FePP and PP absorption show significant spectral change, which indicates stronger interaction between porphyrin and the aptamer strands. **(b)** Porphyrin fluorescence (black) spectra upon addition of aptamer (red) and a-SWCNTs (blue). Similar to the absorption, no detectable interactions are observed for CP and UP. In all measurements (except for PP), porphyrins and aptamer strands are kept at equal molar ratio. For PP, additional aptamer strands (pink) and a-SWCNTs (green) were added (porphyrin:DNA = 1:5) due to lower binding affinity.

addition. This observation supports the proposed interaction mechanisms since the absence of the monomer Soret band features indicates less specific binding interactions due to poor affinity.

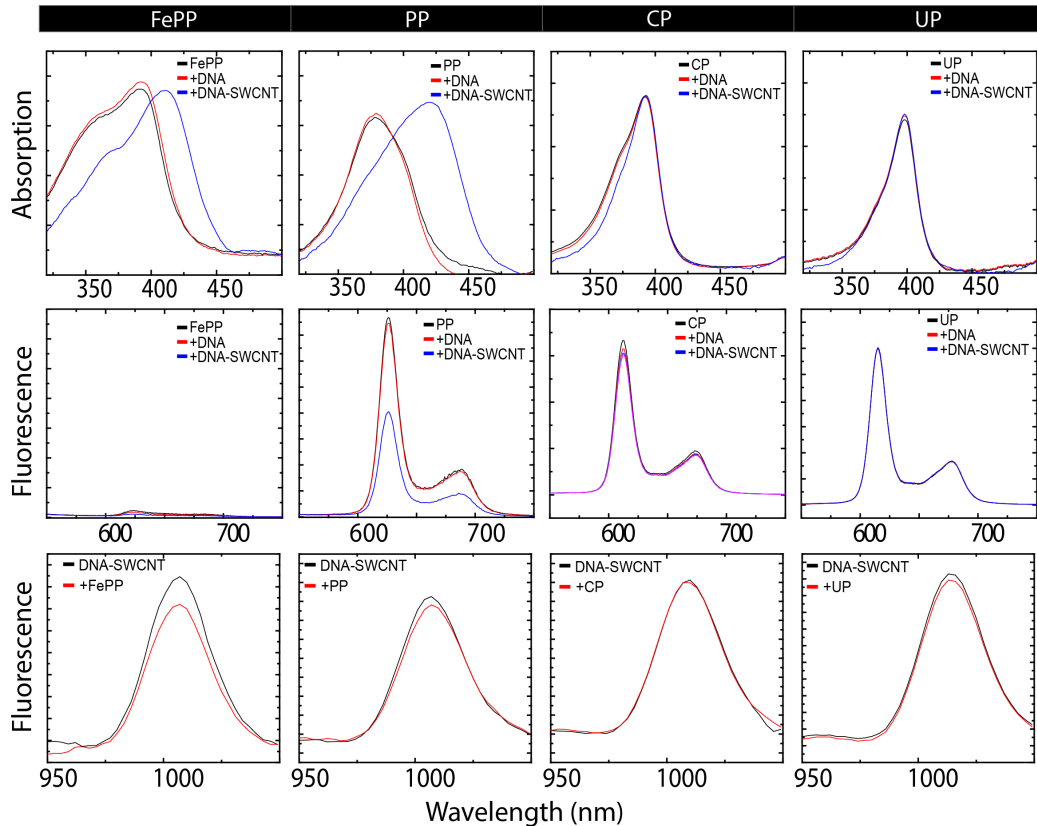


Figure 3.4. Optical signatures for porphyrin/human telomere DNA-functionalized SWCNTs interaction. Compared to FePP-binding aptamer DNA, a 24-nt human telomere DNA (5'-AGG GTT AGGGTT AGG GTT AGG GTT-3') strand was used. The first row shows porphyrin absorption shift upon DNA (red) and DNA-SWCNTs (blue) addition. The second row shows porphyrin fluorescence change. In both absorption and fluorescence measurements, the ratios between porphyrin DNA were kept at 1:1. The third row shows SWCNT fluorescence upon addition of porphyrins (porphyrin/DNA = 1:5). Quenching is observed with FePP addition only.

Close examination of PP fluorescence spectra also supports the proposed interaction mechanisms and provides further insights in the transfer processes. Both free aptamer DNA and a-SWCNTs additions (DNA/PP=1:1 in both cases) decreased the

PP fluorescence intensity (Figure 3.3b, red and blue). While the increased amount of a-SWCNTs addition (DNA/PP=5:1) almost completely quenched the fluorescence (blue to green), more aptamer strands addition resulted in relatively less fluorescence quenching compared to a-SWCNTs addition (red to pink). The decrease observed with aptamer addition is a result of porphyrin-DNA interactions, which also corresponds to the optical responses in porphyrin Soret band [137]. We have shown previously that when fluorescence intensity is corrected for absorption change, the variation is no longer observed in the fluorescence spectra with DNA addition [127, 137]. In contrast, the significant decrease in fluorescence after DNA-SWCNTs addition persists even with the absorption correction, which is attributed to transfer interaction between the porphyrins and nanotubes [113, 127]. As a comparison, when human telomere DNA was used, no optical response was observed after DNA addition, while human telomere DNA-SWCNTs caused a large decrease in fluorescence intensity.

3.4.3 Quantification of Porphyrins from Mixture

The optical responses of a-SWCNTs interaction with the porphyrin species are used to formulate a multiplexed method for porphyrin quantification in mixture solution (Figure 3.5). As a first step, the amount of SWCNTs fluorescence quenched by FePP was directly correlated to its concentration in solution (Figure 3.5a). The addition of increasing FePP in a-SWCNTs solution resulted in gradual SWCNT fluorescence quenching. A detection limit of ~ 20 nM was determined from the characterization of the linear range from 0 to 200 nM. Of considerable utility is that the nanotube emission quenching by FePP is not affected by the presence of PP, CP, and UP. While the sequential addition of other three porphyrins didn't show any optical modulation, the addition of FePP to the a-SWCNTs/porphyrin mixture immediately led to a 25% decrease of nanotube fluorescence intensity (porphyrin:DNA = 1:5). In the second step, the PP concentration was calculated by taking the difference of the porphyrin fluorescence spectra before and after a-SWCNTs addition (Figure 3.5b and

c). The fluorescence spectrum of porphyrin mixture is the sum of the fluorescence signals of PP, CP, and UP, depending on their respective concentrations, since FePP does not demonstrate radiative emission. The PP component in the total fluorescence spectrum was quenched upon excess a-SWCNTs addition (porphyrin: DNA=1:20), resulting in a spectrum of only CP and UP components (Figure 3.5b). The PP fluorescence was reconstructed by taking the difference between the spectra before and after a-SWCNTs addition (Figure 3.5c). The correlation between fluorescence intensity and PP concentration was experimentally determined. Thus, the PP concentration in mixture was calculated.

In the last step, with the FePP and PP concentrations determined, the CP and UP concentrations in mixture were quantified using absorption spectra [124]. Under aqueous buffer conditions, CP and UP have absorption maxima at 392 and 398 nm, respectively (Figure 3.5d), and the isosbestic point of CP and UP mixture is at 391 nm (Figure 3.5e). The molar extinction coefficient (ϵ) of each porphyrin species at 391 nm was determined by correlating the optical density with the known porphyrin concentration. The sum of the UP and CP Soret band absorption spectrum was generated by subtracting the PP and FePP components from the mixture absorption spectrum. By varying UP (or CP) percentage in the mixture, we obtained a correlation between mixture solution absorption maximum wavelength and the ratio of UP to CP (Figure 3.5f). The total CP and UP content was determined by the absorption at the isosbestic point, and the molar fraction of UP and CP were then estimated from the absorption peak wavelength. After applying our detection steps, the contributions of each porphyrin species to the total optical signal were obtained and reconstructed as shown in Figure 3.6. The comparison of the calculated and experimental results shows an excellent agreement in both absorption and fluorescence of mixture solution.

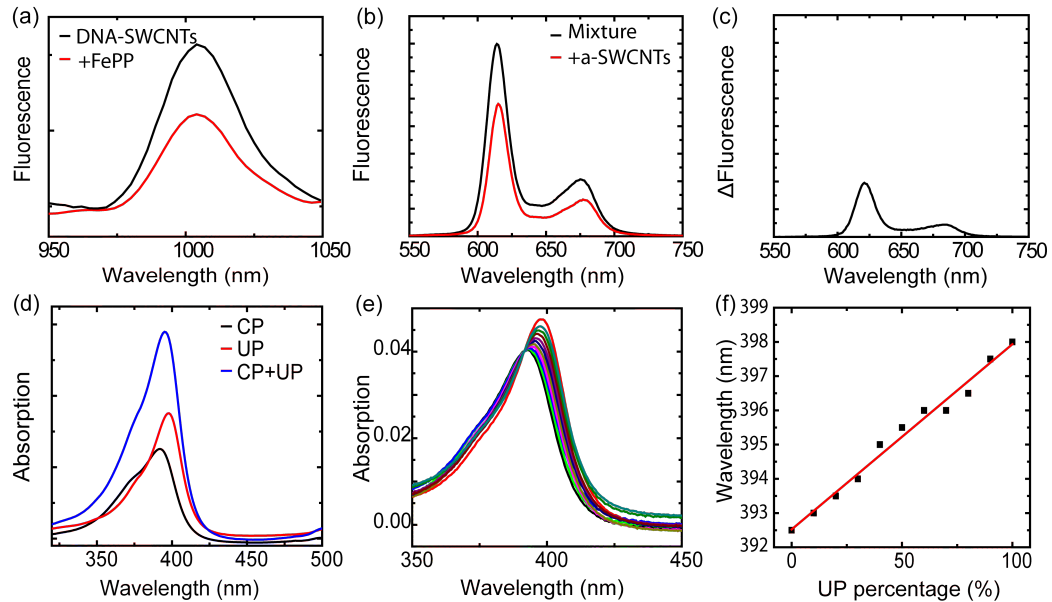


Figure 3.5. Multiplexed porphyrin quantification scheme. **(a)** SWCNT emission quenching by FePP, from which the FePP concentration can be obtained. **(b)** Porphyrin mixture emission quenching upon a-SWCNTs addition. An excess amount of a-SWCNTs was added to ensure complete PP fluorescence quenching. **(c)** Difference spectrum constructed from **(b)** shows PP fluorescence, which can be used to quantify PP concentration. **(d)** Total absorption spectrum (blue) of CP (black) and UP (red) obtained by subtracting fractions of FePP and PP. **(e)** The experimental determination of the isosbestic point of CP and UP at 391nm. **(f)** Absorption peak shift with increasing UP concentration. The total concentration of CP and UP mixture can be determined from **(d)** at its isosbestic point, while individual fractions of CP and UP is determined by the absorption peak position.

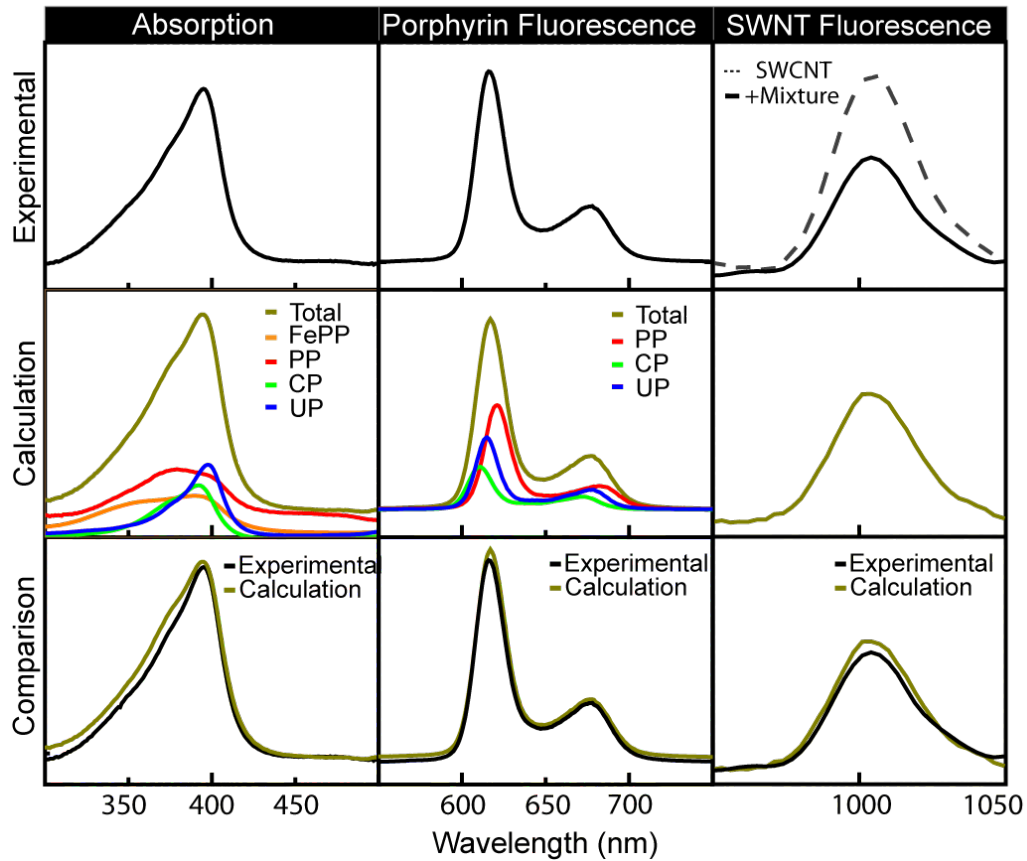


Figure 3.6. Results of porphyrin mixture quantification. Top row: porphyrin optical absorption and emission, as well as a-SWCNT NIR emission quenching. Middle row: the estimated fraction of each porphyrin type compared to that of the experimentally measured mixture values. Bottom row: experimentally measured absorption and fluorescence spectra compared with the recovered spectra from calculation.

3.4.4 Porphyrin Detection in Plasma

Our method can readily be combined with existing porphyrin solvent extraction methods for quantifying plasma porphyrins. The plasma porphyrin test is useful for the diagnosis of porphyrin related diseases as it is both sensitive and specific [121]. Typically, there are only trace amounts ($<1 \mu\text{M}$) of porphyrins in blood. However, the plasma porphyrin concentration increases drastically for patients with diseases such

as porphyria ($\sim 40 \mu\text{M}$). Additionally, the plasma porphyrin concentration has been directly related to disorders of heme synthetic pathways and is thus a more specific indicator than urinary or fecal porphyrins [121]. In plasma, porphyrins are bound to albumin and hemopexin with high affinity [126]. A fluorescence scanning approach based on solvent extraction to remove bound proteins has been suggested for plasma porphyrin tests [121, 125]. Mixing plasma with porphyrin extraction solution precipitates all proteins in plasma, and porphyrins were recovered to their free forms. Figure 3.7 shows our experimental results where an abnormal plasma porphyrin concentration was simulated by adding a known concentration of each porphyrin in the plasma sample, mimicking the possible scenario of the disease Porphyria Cutanea Tarda. The resultant free porphyrin containing extraction solution was used as stock solution and subjected to our detection schemes to obtain quantitative porphyrin concentration data. In Figure 3.7, the gray bar represents the concentration of each type of porphyrin in plasma determined from our measurements, while the white bar denotes the value of each porphyrin species added to the plasma. The experimental error for each porphyrin species is less than 3%, demonstrating a better accuracy than the previous fluorescence scanning method with $\sim 10\%$ errors [124]. It should be emphasized that this method enables an one-step extraction, whereas the previous methods require multiple extraction steps to separate the mixture into individual porphyrin species before quantification.

3.5 Conclusions

In summary, we have shown that oligonucleotides can be used to program the molecular interaction characteristics of optical nanomaterials. As a model system, we demonstrated an analytical platform for blood porphyrin quantification. Two interaction mechanisms, specific binding of aptamer to porphyrins and non-specific adsorption of porphyrins on nanotube sidewall, are used to modulate optical properties of optically active SWCNTs and porphyrins. The affinity between aptamer

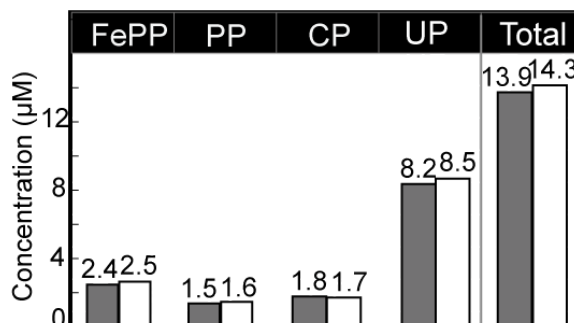


Figure 3.7. *In-situ* quantification of porphyrins in blood plasma. Porphyrins were added to human plasma sample with known concentrations. The sample was then subjected to solvent extraction and optical quantification. White bar shows the extracted values and the gray bar represents the calculated concentrations of each porphyrin species. Numbers above the columns also indicates the corresponding concentrations.

and target molecules (porphyrins) is used to control the optical responses. Using this aptamer-SWCNT system, a multiplexed porphyrin sensing strategy is developed. The platform developed in this study can readily be used for porphyrin detection in plasma samples, eliminating otherwise laborious porphyrin separation steps. We envision that such programmed molecular system can be applied to study various dynamic processes. In the next chapter, we use similar system construction (functional DNA with optical nanomaterials) to study synthetic molecular walkers.

4. UNDERSTANDING DNAZYME WALKER KINETICS

4.1 Introduction

The excellent programmability of nucleic acids have been exploited to construct static nanostructures of complex geometries [138–140] as well as dynamic nano-devices with diverse behaviors. Such dynamic systems includes circuits [141–143], catalytic cascades [28, 144], switches [10, 12], and reconfigurable structures [145–147]. In the previous chapter, we demonstrate that functional DNA aptamer strands could modulate molecular interaction at nanomaterial surface and serve as a novel molecular probes. In this chapter, we describe a DNAzyme based synthetic molecular walker. As described in Chapter 1, DNA walkers achieve linear motion by continuously consuming fuel strands planted on a track. The walker competes a single step (or turnover) through a series of reactions, including walker association, enzymatic cleavage, and branch migration. Since the first bipedal DNA walkers were demonstrated in 2004 [18, 19], multiple walking mechanisms have been designed to drive nanoscale translocation [20, 21, 24, 26, 30, 33, 38–41, 148]. DNAzyme based walkers achieve autonomous and processive movement by hydrolyzing RNA substrate and extracting chemical energy. They walk directionally by a so-termed “Burnt-bridge” mechanism [20, 21, 24, 33, 38, 45]. Typical DNAzyme walkers have motility ranging from 0.001 to 0.1 nm s⁻¹, which is several orders of magnitude slower than biological counterparts such as kinesin and dynein motors. The rich chemistry and programmability of DNA walkers make them an ideal system for various tasks, such as organic synthesis [149] and molecular transport [31]. The walker platform could also in turn serve as a well-controlled system to elucidate fundamental biochemical reaction kinetics.

A major problem for the rational design of DNAzyme walker is how design parameters affect walker translocation kinetics. Both experimental and simulation studies were performed in recent years to improve DNA walker performance [49, 150, 151]. However, no engineering guidelines have been proposed for the design of DNAzyme walkers with specified properties. To address this problem, we performed mechanistic studies to elucidate key design parameters that govern the motility and processivity of DNAzyme walkers. To measure detailed kinetics data, we integrate DNAzyme walkers with optical nanomaterials for direct visualization. CdS quantum dot functionalized by DNAzyme walker translocates autonomously and processively along a RNA-coated carbon nanotube track [35]. Both the walker and track can be directly imaged using their distinctive fluorescence. We explored the effects of DNAzyme type and structure, recognition arm lengths, and environmental factors such as ionic strength. A single-molecule kinetics model was developed to evaluate both single-turnover and intermediate reaction rates. Kinetics-based design guidelines are extracted from the model, which greatly enhance the walker performance as we demonstrate an unprecedented walker moving processively near $5\text{ }\mu\text{m}$ with an average velocity of $\sim 1\text{ nm s}^{-1}$. Based on the extracted walking kinetics, we also show the incorporation of photo-isomerizable azobenzene moieties can be used for photo-regulation of walker motility. The work presented in this chapter provides general design principles to construct high performance DNA walkers with regulated kinetics.

4.2 Scheme

4.2.1 Kinetic Model

The reaction pathway of a single walking cycle or a single turnover event of DNA and nicking restriction enzymes was proposed as a 4-step process [21, 35, 45]. However, three rate-limiting intermediate steps in the single turnover event predominantly determine the overall walker kinetics. To extract design principles for DNA walkers, a kinetic model that accurately reflects the biophysical nature of the reactions and pro-

vides means for quantitative evaluation of each design parameter must be established. Here, we model the walker's stepping process by taking into account the rate-limiting steps as shown in Figure 4.1a. Initially, the nanoparticle (shown in yellow) capped DNA enzyme strand (E) is bound to the RNA substrate (S1, blue) through base-pairing of the upper and lower recognition arms (red) on the nanotube track (black). The enzyme core (green) cleaves the prearranged part (pink) of S1 into two fragments (P1 and P2) in the presence of divalent metal cations (M^{2+}) [152]. This irreversible catalytic cleavage reaction is critical in walker operation as the walker did not exhibit any significant movement with no cations or when the catalytic core and RNA strands were mutated such that catalytic cleavage reactions were prohibited [35]. After cleavage reaction, the upper RNA fragment or P1 is replaced by the next unbound RNA fuel strand S2, transitioning from state (ii) to (iii) as the duplex ES2 is thermodynamically more stable. Subsequently, the lower recognition arm displaces from P2 and migrates to S2 ((iii) \rightarrow (iv)), completing a single turnover event [153].

The single turnover event can be analyzed based on molecular statistics given the stochastic nature of the reactions at the single-molecule level. Each reaction step in a single turnover event is associated with a characteristic time τ , which denotes the waiting time to complete a state transition. The waiting time τ is a stochastic variable that can be characterized by its statistical distribution $P(\tau)$. For a single-step process, $P(\tau) = ke^{-k\tau}$ follows a single exponential decay, where $k = 1/\langle\tau\rangle$ is the reaction rate constant. Similarly, the waiting time for the single turnover event depicted in Figure 4.1a is associated with three intermediate steps, and its probability distribution is the convolution of three exponentials. The distribution $P(\tau)$ and its moments contain rich kinetic information about individual intermediate steps as well as single turnover event [154, 155]. The first moment of single turnover provides a mean reaction time [155, 156]:

$$\langle\tau\rangle = \int_0^\infty P_{(i)\rightarrow(iv)}(\tau)\tau d\tau = \frac{1}{k_1} + \frac{1}{k_2} + \frac{1}{k_3} = \frac{1}{k_{single}} \quad (4.1)$$

Here, three reaction rate constants (k_1, k_2 and k_3) reflect the contribution of its corresponding chemical process to the overall translocation kinetics (k_{single}). Cleavage

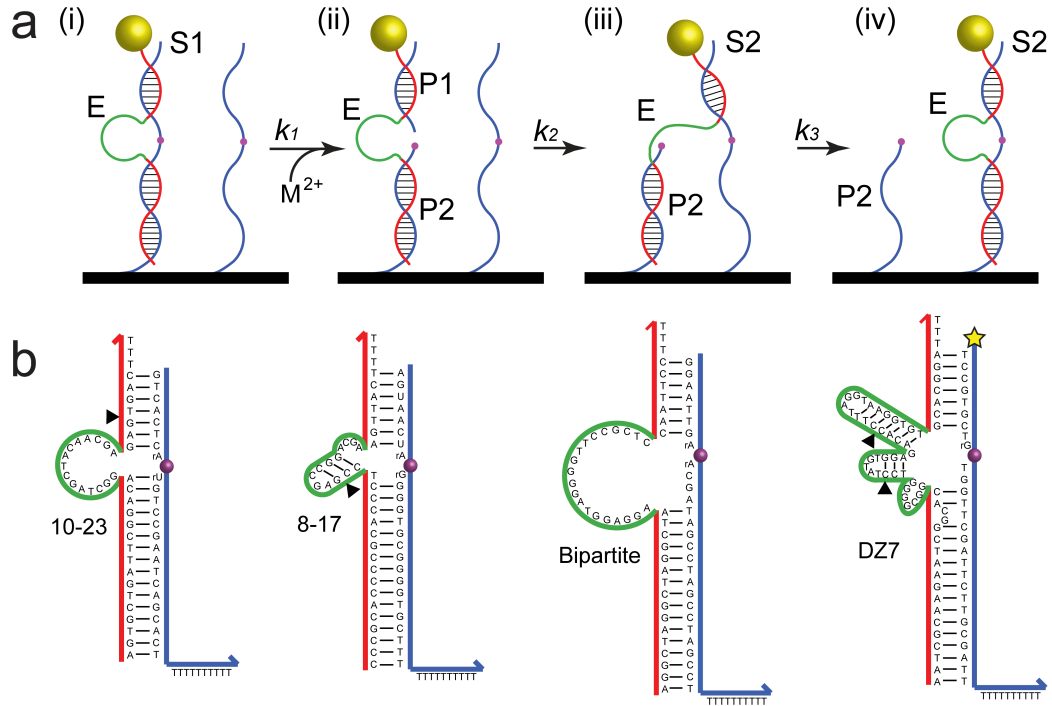


Figure 4.1. DNAzyme walking mechanisms. **(a)** A CdS quantum dot (yellow sphere) is decorated with DNAzyme. The walking process starts with the walker strand (E) associated to a fuel strand (S1) immobilized onto nanotube sidewall. The walker strand contains a catalytic core (green) and two recognition arms (red). The catalytic core E hydrolyze the RNA fuel at specific site (pink) at the presence of metal cations (Mg^{2+}), creating a nick site and a less stable duplex structure with two fragments (P1 and P2). The upper fragment will then be replaced by the next intact fuel strand (S2) at rate k_2 . As a full complementary binding with strand S2 is thermodynamically more favorable, the lower walker arm will spontaneously migrate to S2 at rate k_3 . The three steps completes a single enzymatic turnover. Repetition of this process leads to autonomous, processive and directional movement, which can be directly imaged using the fluorescence of quantum dot and nanotube. **(b)** Walker strand with four different types of DNAzymes core. Black triangles indicates azobenzene modification site in photo-regulation experiments. Yellow pentagram indicates FAM fluorophore for solution based reaction rate measurement.

reaction rate k_1 depends on the DNA enzyme core type and structure. Strand replacement rates k_2 and k_3 of the upper and lower recognition arms are determined by the length and sequence. Environmental factors such as divalent cation type and concentration also contribute to all reaction rates. Numerical calculation of the rate constants relates to experimentally obtained walker velocity $\langle v \rangle$ and step size l by: $k_{single} = \langle v \rangle / l$. The change of design parameters in our experiments leads to the change in the reaction rate k_{single} values which thereby provide a quantitative measure of the parameters' effect on the overall translocation kinetics. In this analysis, the rate constant of each intermediate step (*i.e.* k_1, k_2 and k_3) is correlated with design parameters through the calculations presented below.

4.2.2 Calculation of Reaction Rates

For enzymatic cleavage of the fuel strand, k_1 is the metal cation-dependent reaction rate, which is governed by the Michaelis-Menten equation [152]:

$$k_1 = \frac{k_{max}[M^{2+}]}{([M^{2+}] + K_d)} \quad (4.2)$$

where $[M^{2+}]$ the concentration of the divalent metal cation, and K_d is the dissociation equilibrium constant for the given metal cation M^{2+} . K_d varies from 10 to 200 mM depending on the sequence [157–159], and is fixed at 50 mM in our calculations. k_{max} represents the maximum cleavage reaction rate under a saturated concentration of metal cations, and is primarily determined by the sequence and structure of the DNA enzyme core as well as the metal cation species used in this study [152]. It is assumed that k_{max} is unaffected by the length and sequence of the recognition arms. In this work, the k_1 of the 10-23 enzyme from the report by Santoro and Joyce [152] was used as an input for the calculation of k_2 and k_3 in studying the effect of the recognition arm length. With knowledge of k_2 and k_3 , the cleavage rate k_1 for 10-23, 8-17, bipartite, and DZ7 DNA enzymes were determined [157–159].

The process of upper/lower recognition arms migrating to the next fuel strand is modeled as a random walk of the ends of the duplex with reaction rates k_2 and k_3 [156, 160]:

$$k_{2,3} = k_{sd}c[S] = \frac{2k_a c[S]}{(N - 2n + 2)} \exp\left(\frac{\Delta G_n}{RT}\right) \quad (4.3)$$

Here, k_{sd} is the strand displacement rate calculated by $k_{sd} = k_a P_1 P_2$. k_a is the association rate constant for duplex formation, measured as $10^6 \sim 10^7 \text{ M}^{-1} \text{ s}^{-1}$ [156, 161, 162]. $k_a = 4 \times 10^6 \text{ M}^{-1} \text{ s}^{-1}$ was used in our calculation. $P_1 = 2\exp(\frac{\Delta G_n}{RT})$ is the probability that n base-pairs dissociate from the original duplex, and has an exponential dependence on the free energy ΔG_n for opening up the duplex. n is the minimum number of base-pairs required to form a stable duplex, and its value is typically between 3 and 4, [156] or used as the toehold length in the case of toehold-mediated strand displacement. ΔG_n is computed from the Nearest Neighbor model [163, 164]. R and T denote the universal gas constant and temperature. $P_2 = \frac{1}{N-2n+2}$ is the probability that the branched point migrates to the end of duplex which results in the total displacement of the original strand. N is the total number of displacing base-pairs, which is the arm length.

The term $[S]$ in Equation (4.3) is the concentration of fuel strands (*i.e.* RNA substrates) on the carbon nanotube track. $[S] = 1 \text{ mM}$ is calculated based on the moles of RNA substrates in a cubic volume whose dimension equals to the walker step size l . One major difference between our kinetic study and traditional solution-based kinetics analysis is the determination of local substrate concentration. In most traditional kinetics studies, the measurements are typically taken in free solution. Therefore, the reaction rate k and substrate concentration $[S]$ account for the diffusive nature embedded in the enzymatic reaction process. In contrast, the recent development in surface-based walker systems [33–35, 45, 165] is non-diffusive in that the walkers follow prescribed paths on a surface. The reaction kinetics model should thus describe the effects exerted by surface constraints as well as other factors such as assembly quality. Here we propose to use a correction factor c as shown in Equation (4.3) to account for such effects. We examined the effect of the recognition arm length

on the correction factor and fixed all other parameters that potentially affect walker kinetics. The 10-23 DNA enzyme was used for all experiments studying arm length effects under identical conditions. Since the k_1 value for the 10-23 DNA enzyme is well characterized in the literature (Table 4.4) and is not affected by the recognition arm length, it is used as a fixed value in our calculation of c . When the effect of the recognition arm length is factored into c , its physical meaning can be understood as the probability of finding the next available fuel strand. Therefore, a fuel strand (and the corresponding enzyme strand) with the longer total length should have a larger c value. Overall, the total length effect (probability of finding the next fuel strand) and strand displacement kinetics (the shorter the arm length, the faster the kinetics) are two competing mechanisms in determining the recognition arm displacement rates k_2 and k_3 .

The rate constant associated with each reaction step is computed by varying only the parameter under study while fixing all other variables. Residual minimization is performed to fit the computed k_{single} from Equation (4.1) to the experimental data. The rate constants that provide the best-fit curve are extracted.

4.3 Methods

4.3.1 DNA Enzymes and RNA Substrates

In our mechanistic study, we examined several critical parameters that govern the translocation kinetics of DNA walkers. These parameters include DNA enzyme core type and structure, upper/lower recognition arm lengths, and metal cations. To explore the effect of DNA enzyme core type, four different DNA enzymes (10-23, 8-17, bipartite, and DZ7) and their corresponding RNA substrates were studied, while their upper and lower recognition arm lengths were fixed at 7 and 16 nucleotides (nt), respectively. The effect of the recognition arm length on walker kinetics is studied from two aspects: the total arm length and the relative length of the upper/lower recognition arms. The effect of total arm length on the DNA enzyme's catalytic

activity was previously studied with the 10-23 DNA enzyme by varying the total arm-length gradually from 4/4-nt to 13/13-nt [152]. We chose the most representative cases (i.e. 4/4-, 7/7-, and 13/13-nt) for study in this work. The effect of the relative upper/lower arm lengths were also investigated using 10-23 DNA enzymes with 7/7-, 7/16-, 7/25-, 16/7-, and 25/7-nt arms. These 5 cases cover all possible configurations of the relative upper/lower arm lengths, illustrating the overall trend of the recognition arm length effect. For photo-regulation experiments, azobenzene-integrated DNA enzymes (10-23, 8-17, and DZ7) were utilized. For 10-23 enzymes, the azobenzene molecules were attached in the upper recognition arms, while 8-17 and DZ7 enzymes have the photo-responsive moieties in their hairpin stems of the catalytic cores as shown in black triangles of Figure 4.1b. All custom-synthesized DNA and RNA sequences were purchased from Integrated DNA Technologies, Inc. The sequence information of DNA enzymes and the corresponding RNA strands for all experiments are presented in Table 4.3.1, Table 4.3.1 and Table 4.3.1.

4.3.2 Walker Synthesis

The DNAzyme walker consists of walker-capped nanoparticles and RNA-functionalized SWCNTs. The synthesis procedures of both DNA-CdS QDs and DNA-SWCNTs are described in Chapter 2. The synthesized CdS nanoparticle has a diameter of ~ 3 nm with emission maximum at ~ 550 nm. Based on absorption measurement, approximately 20 DNA walkers are estimated per CdS, but only one DNAzyme is involved in walking [35, 166]. The mono-valence of walker on CdS was confirmed by comparing the translocation velocity of CdS particle with dense (~ 20) or sparse (~ 2) surface walkers attached [150]. CdS nanocrystals with different surface walker density show nearly identical motility. The walker-CdS particle and fuel-SWCNT track were incubated in $1\times$ TAE buffer (40 mM Tris, 20 mM acetic acid and 1mM EDTA) for 48 hr at 1:1 molar ratio in dark.

Table 4.1.
Sequence information for DNAzyme walkers with different enzymatic core.

Item	Sequence ^a
10-23 DNAzyme	5'-AGT GCT GAT TCG GAC AGG CTA GCT ACA ACG AGA GTG ACT TT-3'
10-23 RNA	5'-GTC ACT CrArU GTC CGA ATC AGC ACT TTT TTT TTT T-3'
8-17 DNAzyme	5'-CCC GCA CCC CGC ACC CTC CGA GCC GGA CGA AGT TAC TTT T-3'
8-17 RNA	5'-AGT AAC TrArG GGG TGC GGG GTG CTT TTT TTT TTT TT-3'
Bipartite DNAzyme	5'-AGG CTA GGC TAG GCT AAG GAG GTA GGG GTT CCG CTC CAA TTC CTT T-3'
Bipartite RNA	5'-GGA ATT GrArA CGA TAG CCT AGC CTA GCC TTT TTT TTT TT-3'
DZ7 DNAzyme	5'-AAT CGC AAG AAT CGG CAC GGC GGG GTC CTA TGT GGA GAC ACC TTT AGG TAA GGT GTG CAC GGA TTT-3'
DN7 RNA	5'-TCC GTG CTrG TGG TTC GAT TCT TGC GAT TTT TTT TTT TT-3'

a. 7-nt upper and 16-nt lower arm configuration is used for all cases unless otherwise specified.

Table 4.2.
Sequence information for DNAzyme walkers in solution measurement and photoregulation experiments.

Item	Sequence
FAM-DZ7 RNA ^a	5'-6-FAM-TCC GTG CTrG TGG TTC GAT TCT TGC GAT TTT TTT TTT TT-3'
Azo 10-23 DNAzyme	5'-AGT GCT GAT TCG GAC AGG CTA GCT ACA ACG AGA G /Azobenzene/ TG ACT TT-3'
Azo 8-17 DNAzyme	5'-CCC GCA CCC CGC ACC CTC CGA G /Azobenzene/ CC GGA CGA AGT TAC TTT T-3'
Azo DZ7 DNAzyme	5'-AAT CGC AAG AAT CGG CAC GGC GGG GTC /Azobenzene/ CTA TGT GGA GAC AC /Azobenzene/ C TTT AGG TAA GGT GTG CAC GGA TTT-3'

a. FAM represents 6-carboxyfluorescein.

4.3.3 Flow Channel Assembly

For imaging experiment, a flow cell is prepared for sample immobilization and buffer change [35]. Flow channels are manually cut on a acrylic tape before assembly. The tape is then sandwiched between a quartz slide and coverslip. Inlet and outlet holes are drilled onto the slides and connected to Tygon tubings. Epoxy is used to seal gaps in-between the tubing and the ports. The assembled walker/track sample were deposited onto a 2 wt.% agarose film on the imaging plane.

4.3.4 Optical Platform

The fluorescence emission of CdS nanoparticles and carbon nanotubes were imaged directly for tracking DNA translocation. The microscope setup is described in Chapter 2. A 658 nm laser diode was used for carbon nanotube excitation, which is

Table 4.3.
Sequence information for DNAzyme walkers with different arm lengths.

Item	Sequence ^a
4/4-nt RNA	5'-ACT CrArU GTC TTT TTT TTT T-3'
7/7-nt RNA	5'-GTC ACT CrArU GTC CGA TTT TTT TTT T-3'
13/13-nt RNA	5'-TCA CTC GTC ACT CrArU GTC CGA ATC AGC TTT TTT TTT T-3'
7/25-nt RNA	5'-GTC ACT CrArU GTC CGA ATC AGC ACT GTC CGA ATC TTT TTT TTT T-3'
16/7-nt RNA	5'-TCG TCA CTC GTC ACT CrArU GTC CGA TTT TTT TTT T-3'
25/7-nt RNA	5'-ACT CGT CAC TCG TCA CTC GTC ACT CrArU GTC CGA TTT TTT TTT T-3'

a. 10-23 DNAzyme core is used for all cases. Sequence rArU denotes cleavage point recognized by DNAzyme.

predominantly in resonance with (7,6) and (7,5) tubes that fluoresce at around 1,150 nm and 1050 nm. CdS fluorescence in the visible range (550 nm) is imaged using 405 nm excitation. Images from both VIS and NIR channels are taken every 3 hr. Typical experiment lengths are 12 hr.

The two imaging channels (VIS and NIR) were registered in each experiment to ensure accurate co-localization (Figure 4.2). A stage micro-ruler was imaged in both channels before each experiment to obtain the transformation matrix for the co-localization. The same transformation matrix was then applied to all recorded images throughout the remainder of the experiment. The QD emission PSF was smoothed and interpolated to estimate the walker position using PSF centroid [35, 55].

Uncertainty analysis was performed to determine measurement and alignment precision. To obtain measurement precision, we captured 20 images of a QD immobilized

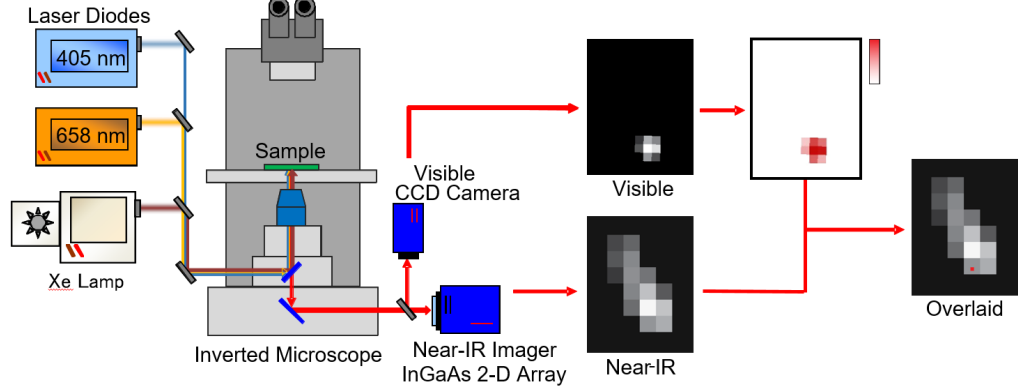


Figure 4.2. Schematic of optical setup and image co-localization method.

on a quartz cover slip with an integration time $t = 1$ s at ~ 20 mW excitation power. A typical value of the standard deviation $\Delta x = \Delta y = 20$ nm was obtained from the analysis of the distribution of the estimated QD position. This value is much smaller compared to the walking distance of at least 300 nm between our measurements. A more critical factor in the experiment uncertainty is the drift of the sample stage due to the mechanical relaxation of the imaging system [138]. To avoid erroneously including the drift as walker displacement, we used near-IR nanotube track images as the fiduciary marker to align the QD images. Carbon nanotube images taken at each sampling time were registered with respect to the reference image which was the first measurement in the experiment. The displacement of the QD along the 1-D nanotube image after the alignment with the reference image was then treated as the actual displacement. Alignment precision is the registration accuracy of the nanotube track to the reference track image. To quantify our alignment precision, we performed a control experiment where a QD was immobilized onto a nanotube track without the walking mechanism. The stage was then randomly translated using a piezo stage (Physik Instrument P-545 XY scanning stage) over typical drift distances. The QD position in the first measurement was used as the reference, and the relative distance of the QD to the reference position was calculated after the alignment. The distri-

bution of QD displacements from 30 measurements shows a standard deviation of $\Delta x = 50$ nm $\Delta y = 95$ nm. The combination of the measurement and alignment precision yields an overall experimental uncertainty of $\Delta x = 55$ nm $\Delta y = 97$ nm. In all our experiments, we used a sampling time that allowed the walkers to produce a displacement at least three-folds larger than the uncertainty level. A typical experiment took 4-12 hr depending on the experimental conditions. Both QD and carbon nanotube fluorophores in our system are highly photo-stable [139, 140], which maintain similar uncertainty level throughout all the measurements. The displacements we measured in actual experiments were at least three-folds larger than this value to be considered as walking.

4.3.5 Calculation of Walker Step Length

To estimate the average distance between two neighboring RNA substrates (*i.e.* walker step size l), the total concentration of RNA strands and carbon nanotubes were determined based on the optical absorption signatures of RNA-functionalized carbon nanotubes from 200 to 1350 nm. The total number of RNA strands in the solution sample was calculated using their absorption intensity at 260 nm and their extinction coefficients. The carbon nanotube absorption at 632 nm was used to determine the nanotube concentration based on the extinction coefficient of $3.6 \times 10^4 \text{ cm}^{-2} \text{ g}^{-1}$. We roughly estimate that the average number of RNA strands is ~ 28 per 100-nm-long carbon nanotube. From this estimation, we assumed that the distance between two neighboring RNA strands is approximately 3.5 nm and that the fuel strands are uniformly decorated along the one-dimensional nanotube track.

4.3.6 Ensemble Single Turnover Rate Measurement

As an alternative approach to determine the single turnover reaction rates, we measured the rate of the DZ7 enzyme walker ensemble and compared it with the rate obtained from our single molecular motor measurements (Figure 4.3). First, we

incorporated fluorophores (Fluorescein or 6-FAM) at the 3'-end of the fuel strands (yellow pentagram in Figure 4.1b) and collected the RNA fragments (*i.e.* fluorophore-attached P1) generated by motor operation at the outlet of the microchannel for 2 hr at a flow rate of $100\text{ }\mu\text{L hr}^{-1}$. The amount of collected RNA fragments was determined by measuring the emission intensity of the fluorophores. With knowledge of the number of DNA walkers in the reaction chamber, we calculated the single turnover reaction rate in the presence of 50 mM Mg^{2+} . In our calculation, we assumed that all the walkers in our ensemble sample moved at a uniform speed, given the continuous operation of our DNA walkers. The single turnover rate measured from the fluorophore-attached DZ7 ensemble sample is approximately 0.031 s^{-1} , which is comparable with that (0.026 s^{-1}) from the single walker measurement using our single-particle/single-tube spectroscopy (Figure 4.3b). As a control experiment, the fluorophore emission was also measured in the absence of metal cations. As anticipated, the collected solution did not show any significant fluorescence emission as shown in Figure 4.3c, confirming that the fluorophore emission was indeed generated by the walker translocation. It should be noted that the flow in the microfluidic reaction chamber does not have any significant effect on the walker kinetics under our experimental conditions as we observe nearly identical motor speed with and without the flow (Figure 4.3d).

4.3.7 Photo-regulation

Photo-transformable azobenzene moieties, which switch reversibly between two isomers of *trans* and *cis* forms, are used to remotely control DNA duplex formation, thereby walker translocation kinetics. The azobenzene molecules retain their *trans*-form under visible light illumination (*i.e.* 400 - 700 nm) which allows a duplex formation. In contrast, the out-of-plane *cis*-form induced by UV irradiation (*i.e.* 300 - 400 nm) destabilizes the duplex due to steric hindrance. The 7-nt upper and 16-nt lower recognition arms were used in the photo-regulation experiments with 10-23,

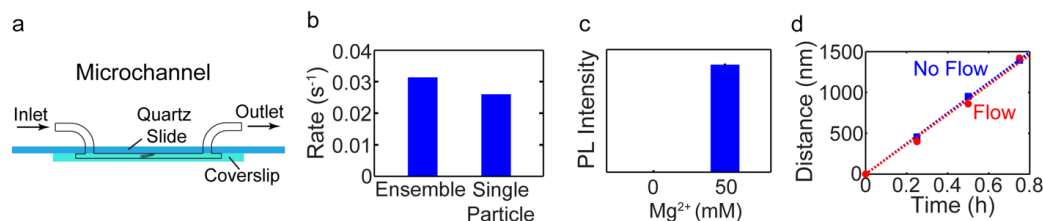


Figure 4.3. Ensemble turnover rate measurement. **(a)** Schematic of the microfluidic reaction chamber for the DZ7 walker experiments to measure the single turnover reaction rate from an ensemble sample. The buffer is introduced from an inlet and flows through the microchannel to an outlet. **(b)** The single turnover reaction rates obtained from the fluorophore-attached ensemble sample (left bar) and from the single-particle/ single-tube spectroscopy of a single DNA walker (right bar). **(c)** The PL signature of P1-attached fluorophores was recorded in the presence of 50 mM Mg^{2+} , whereas no measurable PL signal was observed in the absence of Mg^{2+} (*i.e.* 0 mM metal cation). **(d)** A flow rate of 100 L hr^{-1} is used to collect the byproducts (cleaved RNA fragment P1) from the DNA walker operation at the outlet of the microchannel. No apparent effect of the buffer flow is observed on the DNA walker translocation.

8-17, and DZ7 enzymes. A 150W Xenon lamp (Newport) and appropriate filter sets were used as UV and visible light sources. Approximately 10 min of UV and visible light irradiation were applied to control the isomerization of azobenzene moieties in the DNA walkers. We varied the irradiation time interval from 10 to 30 min to obtain this optimum value for current experimental setup. Irradiation for 10~30 min did not show any significant difference in the effectiveness of photo-regulation, whereas irradiation time less than 10 min had less effective control on the walker kinetics.

4.4 Results

4.4.1 Mechanistic Studies of Walker Translocation Kinetics

We examined several parameters that govern the motor translocation kinetics, including DNA enzyme core type, upper and lower recognition arm lengths, and var-

ious metal cations. First, four different enzyme sequences (10-23, 8-17, bipartite, and DZ7) and the corresponding chimeric RNA/DNA fuel strands in Figure 4.1b were explored [157–159, 167]. These enzymes, identified via in-vitro selection, cleave their respective RNA parts with high sequence specificity through deprotonation of the 2'-hydroxyl group. To elucidate the effect of the catalytic core type alone, the lengths of the upper and lower recognition arms were fixed at 7 and 16, respectively, and the measurements were carried out under identical conditions: pH 8.0 and 25 °C in TAE buffer with Mg^{2+} . To visualize individual motor translocation, we spectroscopically tracked a walker-integrated CdS quantum dot along an immobilized carbon nanotube which fluoresce in the visible and near-infrared, respectively [35]. Figure 4.4a shows experimentally obtained motor speeds (filled objects) and calculated single turnover rates (solid curves in the corresponding colors) of the enzymatic walkers as a function of Mg^{2+} concentration. At saturated cation concentrations (>100 mM), the 10-23 enzyme motor demonstrates a translocation speed of ~ 200 nm hr $^{-1}$, followed by bipartite (~ 170 nm hr $^{-1}$) and 8-17 walkers (~ 120 nm hr $^{-1}$). The DZ7 enzyme-based walker displays a significantly higher motility at ~ 380 nm hr $^{-1}$.

The extracted kinetic parameters (k_1 , k_2 , and k_3) are presented in Figure 4.4b to d. In Figure 4.4b, the cleavage reaction rate varies from 0.020 to 0.12 s $^{-1}$ at 100 mM Mg^{2+} , depending on the catalytic core type. These k_1 values of 10-23, 8-17, and bipartite enzymes are comparable to those determined from free solution ensemble measurements under similar conditions (gray bars in Figure 4.4b) [157–159]. The value for k_1 of the DZ7 enzyme under similar conditions is not available in the literature, to the best of our knowledge. The numerical values of the experimentally extracted k_1 and that found in the literature are also shown in Table 4.4. The displacement rates of the upper and lower recognition arms are shown in Figure 4.4c and d. Given that all four enzymes have 7-nt upper arms, the reaction rates are constant at $k_2 = \sim 0.11$ s $^{-1}$. The 16-nt lower arms show migration rates slower than the 7-nt upper arms at $k_3 = \sim 0.025$ s $^{-1}$. The DZ7 enzyme is an exception which displays $k_3 = \sim 0.060$ s $^{-1}$. This anomaly is attributed to the internal sequence mismatch with

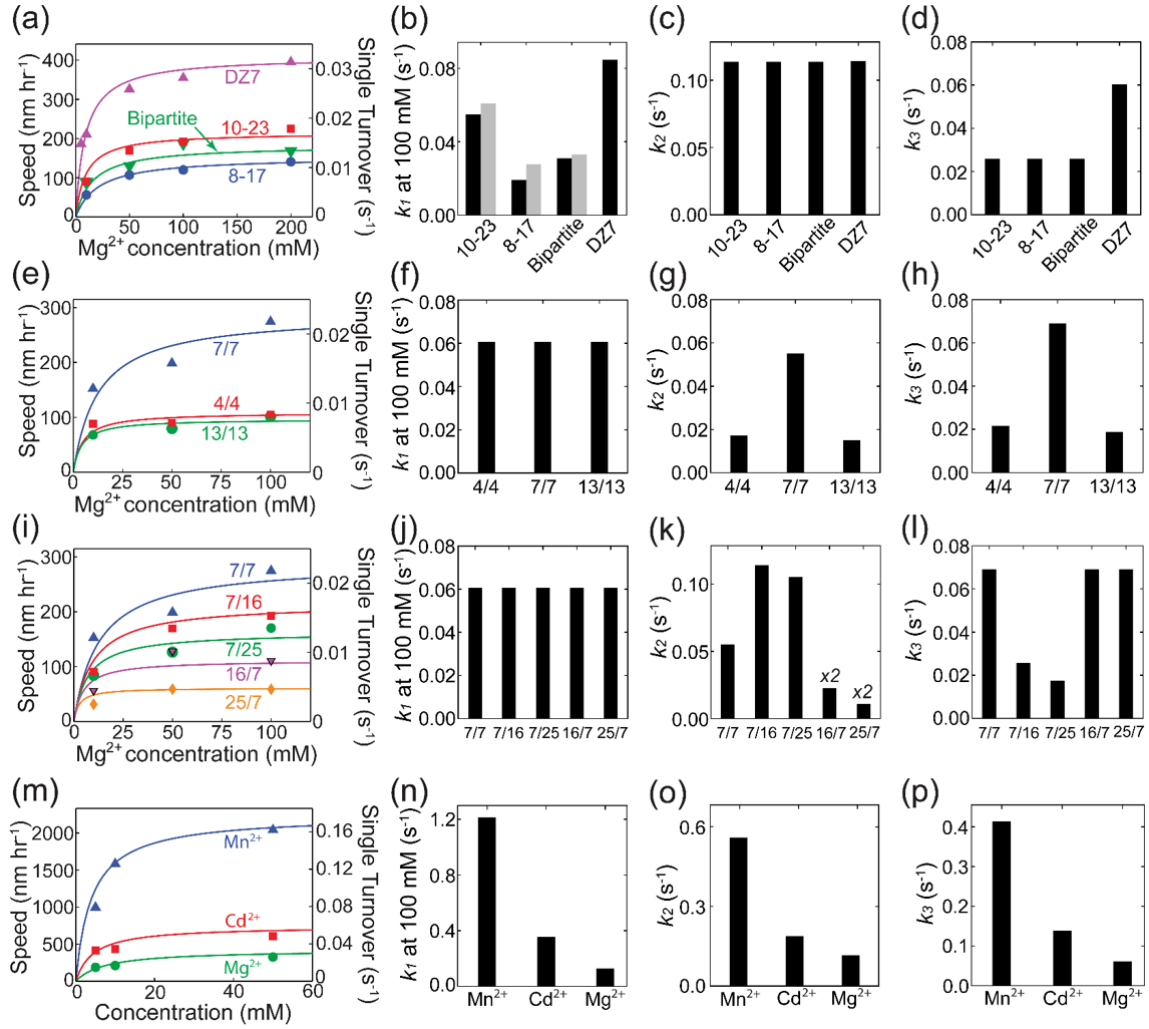


Figure 4.4. Walker motility as a function of DNAzyme type, recognition arm lengths, and environmental factors. Speed (scatter) and simulated single turnover rates (lines) are plotted in the first column. The cleavage reaction rates (k_1) at 100 mM Mg²⁺, upper and lower arm replacement rates (k_2, k_3) are extracted from the kinetic model and plotted in the three bar charts on the right. (a-d) Effect of enzymatic core type. The DNAzyme walker is configured with 7/16-nt arm. (e-h) Effect of total arm length. 10-23 DNAzyme walkers with 4/4-nt, 7/7-nt, and 13/13-nt arm length are compared. (i-l) Effect of asymmetric arm lengths. 10-23 DNAzyme cleavage core is used for all the cases. (m-p) Effect of various metal cations (Mn²⁺, Cd²⁺, and Mg²⁺) on 7/16-nt armed DZ7 DNAzyme walker motility. All experiments were performed in 1× TAE buffer at room temperature.

Table 4.4.
Comparison of cleavage reaction rate k_1 values.

Core	k_1 (kinetic model) ^a	k_1 (literature)
10-23	0.0547	0.0607 ^b
9-17	0.0191	0.0277 ^c
Bipartite	0.0308	0.0330 ^d
DZ7	0.121	N/A

a. All the calculated cleavage rate constants are based on 25 °C, pH 8, and 100 mM Mg^{2+} unless indicated otherwise.

b. Obtained from literature [152], where the experiment was performed in the presence of 150 mM NaCl, 100 mM Mg^{2+} , 50 mM *N*-(2-hydroxyethyl)-piperazine-*N'*-3-propanesulfonic acid (EPPS) at pH 7.5 and 37 °C.

c. Obtained from literature [158], where experiment was performed in the presence of 50 mM sodium acetate, 100 mM Mg^{2+} at pH 7 and 28 °C.

d. Obtained from the literature [159], where the experiment was performed in the presence of 150 mM NaCl, 100 mM Mg^{2+} at pH 7.5 and 23 °C.

two additional bases in the lower recognition arm (Figure 4.4b). The two mismatches increases the overall free energy of the formed duplex [156], rendering such structure less stable than perfect complimentary sequences [168]. Strand displacement of the walkers' lower arms is slower than the previously reported displacement rate of strands with proximal toeholds ($\sim 1.0 \text{ s}^{-1}$), but is similar to the reported rate ($\sim 0.025 \text{ s}^{-1}$) of a 22-nt strand with a 14-nt toehold overhang and a 10-nt toehold spacer [29, 160]. The enzyme cores serve as a spacer between the remote toehold segment (*i.e.* upper arm) and the displacing lower arm, thus suppressing the migration kinetics.

The effect of the recognition arm length on walker kinetics is studied from two aspects: the total strand length and the relative length of the upper and lower recognition arms. First, the total length effect is explored by using symmetric arm configurations. The 4/4-, 7/7- and 13/13-nt upper/lower arm lengths with identical 10-23 DNA enzyme cores are examined (Figure 4.4e to h). These motors display their maximum speeds of approximately 105, 275, and 100 nm hr⁻¹ (corresponding k_{single} of 0.0083, 0.022, and 0.0080 s⁻¹) at 100 mM Mg²⁺, respectively. Since the same catalytic core is used, the cleavage reaction rate $k_1 = 0.061s^{-1}$ is used in the calculations for all the cases (Figure 4.4f). With knowledge of k_1 , both k_2 and k_3 are calculated to best describe the experimental data. From the Nearest-Neighbor model, the shorter armed 4/4-nt walker should have faster kinetics than the other two walkers since the duplex is less stable with fewer base-pairs. However, experimental results clearly indicate that the 4/4-nt walker has a slower speed than the 7/7-nt walker and is comparable to the 13/13-nt walker. A similar trend for DNA enzyme reaction rate was also observed by solution measurement as a result of the less stable enzyme-substrate complex [152]. In our model, the strand length affects both the probability of finding the next available fuel strand and the displacement rate, which compete with each other. Consequently, the 4/4-nt walker experiences a lower effective fuel strand concentration, while the 13/13-nt walker has a slower displacement rate, resulting in a 3-fold slower walker kinetics in both cases compared to the 7/7-nt walker.

Besides the total arm length effect, the influence of the relative lengths of upper and lower recognition arms on the walker kinetics are examined. Figure 4.4i shows the translocation speeds and single turnover rates of the 10-23 DNA enzyme walkers with 7/7-, 7/16-, 7/25-, 16/7- and 25/7-nt upper/lower recognition arms. While the lower arm rates of 7/7-, 16/7- and 25/7-nt armed walkers are held constant at $k_3 = 0.070s^{-1}$ (Figure 4.4l), the upper arm rates k_2 varies from 0.0056 to 0.056 s⁻¹ (Figure 4.4k), depending on the strand displacement and the probability for finding the next fuel strand. In the cases of 7/7-, 7/16-, and 7/25-nt arms, upper

arm rate k_2 increases from 0.056 to 0.11 s^{-1} with increasing total strand length, while the lower arm rate k_3 decreases from 0.070 to 0.017 s^{-1} as a result of an increased number of base-pairs (Figure 4.4l). Unlike solution measurements that may not distinguish between 7/16-nt and 16/7-nt (or 7/25-nt and 25/7-nt) upper/lower arm configurations, our experimental results suggest a significant decrease in speed for the walker with a longer upper arm. The upper arm replacement process resembles strand displacement without a toehold, while the lower arm replacement process is similar to branch migration after stable (remote) toehold duplex formation. The strand displacement process with a toehold segment has much faster kinetics than those without a toehold [144,160]. Thus, the longer upper arm significantly slows the walker as opposed to the longer lower arm.

The role of divalent metal cations (Mn^{2+} , Cd^{2+} and Mg^{2+}) on the DZ7 walker kinetics is shown in Figure 4.4m to p. As previously reported, the catalytic cleavage reaction rate with Mn^{2+} is much greater than those with Cd^{2+} and Mg^{2+} ions [167]. The strand replacement rates are also found to be highly dependent on the metal cation species [169,170]. We used the cation concentration correction correlation [171–173] to calculate k_2 and k_3 (Figure 4.4o to p), and numerically determined cleavage reaction rate k_1 from experiments (Figure 4.4n). Considering the increase in all reaction rates, the overall translocation speed of the DZ7 walker in the presence of Mn^{2+} is much greater than those with Cd^{2+} and Mg^{2+} in our experiment.

With knowledge of detailed motor kinetics, we designed a high-motility walker (Figure 4.5). Here, we used DZ7 enzyme with 7-nt upper and 16-nt lower arms in the presence of 100 mM Mn^{2+} . The identity of a single CdS nanocrystal is verified by intermittent on/off emission phenomena (inset in Figure 4.5). The DNA walker moved around 5 μm along the nanotube track for less than 2 hr with an unprecedented translocation speed of approximately 1 nm s^{-1} . A greater motility is expected with higher buffer temperature.

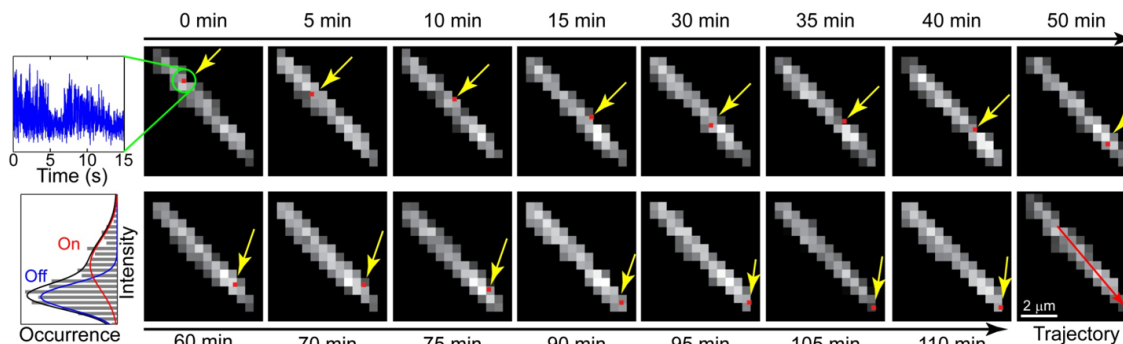


Figure 4.5. DNAzyme walker with high motility and processivity. The time-lapse images show the movement of a DZ7 DNAzyme powered walker with 7/16-nt arm configuration. The walker position is shown as a red dot and emphasized with a yellow arrow. The walker propels itself for $\sim 5 \mu\text{m}$ along the nanotube track with an average speed of $\sim 1 \text{ nm s}^{-1}$ in the presence of 100 mM Mn^{2+} at 25°C and $\text{pH } 8.0$. The blinking of CdS QD shown on the left confirms the single nanoparticle identity.

4.4.2 Photo-regulation of Walker Kinetics

To remotely control the motor kinetics with external light irradiation, we integrated photo-transformable azobenzene into the upper recognition arm of 10-23 enzyme as shown in Figure 4.1b (indicated by the black triangle). The two isomers of *trans* and *cis* forms of azobenzene can be switched reversibly by varying light wavelengths; the *cis*-form is induced by UV irradiation, while visible light converts it into the thermodynamically more stable *trans*-form. [174] This intriguing property of azobenzene was recently used as a versatile switch to control DNA duplex formation and DNA walker direction, [175] as its planar *trans*-form allows base-pairing, whereas the out-of-plane *cis*-form does not, as illustrated in Figure 4.6a. Figure 4.6b and c show the traveled distance over time with alternating light wavelengths and the translocation speeds of the walker with the azobenzene moiety measured in the presence of 100 mM Mg^{2+} . In the absence of external light illumination, no significant differences in the translocation kinetics are observed between the walkers with and without azobenzene moieties ($\sim 200 \text{ nm hr}^{-1}$). After 10 min of UV irradiation,

the walker with the photo-responsive moiety becomes stationary for the next 9 hr, because the *cis* isomer prevents the upper recognition arm from binding to the adjacent fuel strand. Upon visible light illumination, the azobenzene moiety reconfigures to be the *trans* isomer, and the walker resumes its movement along the nanotube track with an average speed of $\sim 200 \text{ nm hr}^{-1}$. It is worth noting that in this experiment, UV-induced DNA damage is not significant as was previously reported that mild irradiant conditions do not cause any adverse effects on the duplex formation of oligonucleotides with azobenzene moieties [176]. Our observation of the reversibility in the motor speeds confirms no evidence of DNA damage.

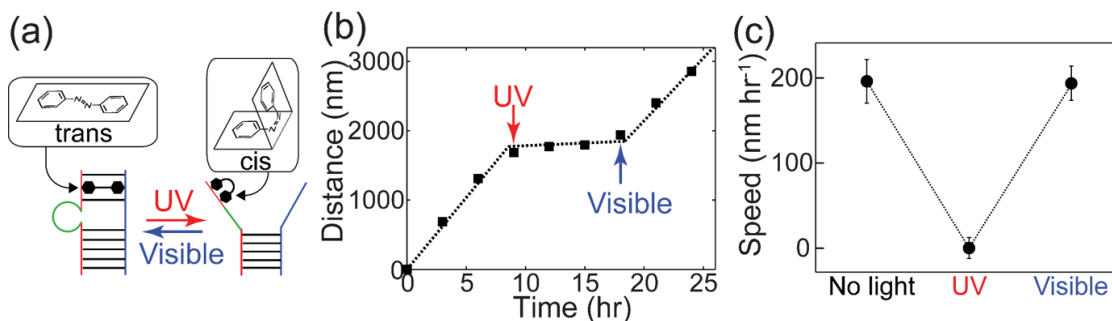


Figure 4.6. Photo-regulation of a DNAzyme walker using azobenzene moiety. **(a)** Schematic of DNA duplex formation controlled by photo-switchable *trans*- and *cis*- form of the azobenzene incorporated into the upper arm of the walker strand. **(b)** Displacement plot and **(c)** the corresponding speed plot of a 10-23 DNAzyme walker with alternating UV/visible illumination. Exposure of azobenzene under continuous UV light for 10 min transforms its structure from *trans* into *cis* form, inhibiting any walking due to dissociated upper arm. Walking activity can be restored after 10 min visible illumination. An average velocity of $\sim 200 \text{ nm hr}^{-1}$ is consistent for walkers with visible light or with no azobenzene moiety. The cation concentration in the TAE buffer is 100 mM Mg^{2+} .

We extended this photo-regulation strategy to study the role of the enzyme core conformation on reaction kinetics (Figure 4.7). Both 8-17 and DZ7 enzymes include hairpin stem structures, where we inserted the azobenzene moieties (indicated by black triangles in Figure 4.1b), such that UV and visible irradiation opens and closes

the hairpin stems, respectively. For both enzymes, the translocation speeds were notably greater after UV irradiation than visible illumination. Our kinetic calculation indicates that the cleavage reaction rates are consistently higher in the enzyme with an open core conformation compared to the enzymes with a closed core structure. In the case of 100 mM Mg^{2+} , $k_{1,UV}/k_{1,visible}$ is approximately 2 for both 8-17 and DZ7 enzymes. A similar observation was reported in a free solution ensemble measurement using 8-17 enzyme derivatives [177]. The enhanced catalytic cleavage reaction with the open core motif may be understood from the more relaxed enzyme conformation which allows metal cations to freely access the reaction site of the fuel strand compared to the more compact, enzyme-RNA conjugate with the hairpin stem. These results suggest that photo-regulation is a powerful way to modulate cleavage reaction kinetics as well as to remotely send on/off signals to DNA walkers.

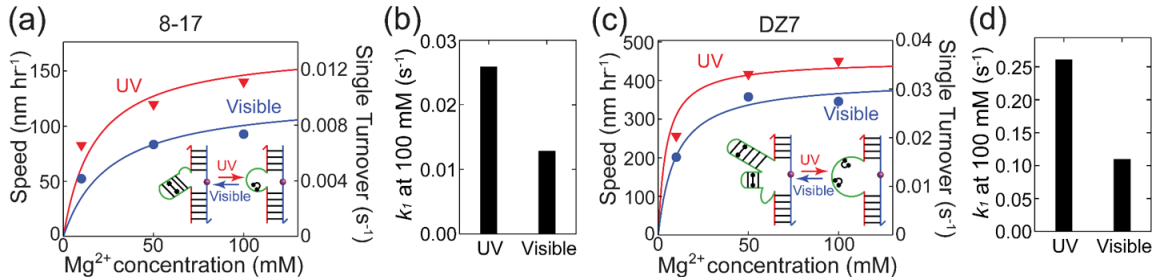


Figure 4.7. Motility of DZ7 and 8-17 DNAzyme walker with azobenzene incorporated in the enzymatic core after UV (red) and visible (blue) illumination for 10min. (a) and (c) show experimentally determined speed (scatter) and simulated single turnover rate (line). (b) and (d) presents rate k_1 of the DZ7 and 8-17 DNAzyme walker at 100 mM Mg^{2+} , respectively.

4.5 Discussion

We have studied the translocation kinetics of DNA enzyme walkers as functions of catalytic core type, recognition arm lengths, and metal cations. Tuning these parame-

ters in walker designs allows us to improve the DNA walker's motility and processivity. Our study provides useful guidelines in DNA enzyme-based walker designs.

4.5.1 Catalytic DNA Enzyme Core

At low metal cation concentrations (<50 mM), the cleavage reaction rate k_1 is typically lower than strand replacement rates k_2 and k_3 , making cleavage the rate-limiting step. The sequence and structure of the catalytic enzyme core have significant effects on k_1 , ultimately regulating overall translocation kinetics. High-speed enzymes such as DZ7 increase the overall walker motility. For 8-17 and DZ7 enzymes, modulation of the walker motility can be achieved through integration of azobenzene moieties within the DNA enzyme core, switching the walker between high speed (open motif) and low speed (closed motif) modes with alternating UV-visible light irradiation.

4.5.2 Recognition Arms

The length of substrate-binding recognition arms affects both the motility and processivity of walker systems. At saturating metal cation concentrations, the strand replacement rates ($0.0056 \sim 0.11$ s^{-1}) are similar to the cleavage reaction rates ($0.031 \sim 0.12$ s^{-1} with Mg^{2+}). For a given enzyme, increasing the strand displacement rates (*i.e.* decreasing arm length) have significant effects on the overall walker speed. As depicted in Figure 4.4e to l, the shorter armed 7/7-nt walker has greater motility than all other cases. However, further decrease in the total recognition arm length (*e.g.* 4/4-nt) slows the walker: the shorter length of the walker strand decreases the effective substrate concentration (*i.e.* probability of finding the next fuel strand), thus decreasing the processivity of the walker. For the same total strand length, the shorter upper arm imparts the walker with faster kinetics than the shorter lower arm. This asymmetric effect is induced by the two different mechanisms of strand replacement (*i.e.* blunt-end and remote toehold) due to surface constraints on the fuel strands. In general, a stable enzyme-substrate complex ensured by the lower recog-

nition arm (>10 -nt) and a highly reactive upper arm (<10 -nt) are recommended for high motility/processivity walker designs. The incorporation of azobenzene moieties in the recognition arms provides a powerful method for sending 'go/stop' signals to the walker through external light stimuli.

4.5.3 Environmental Effects

Divalent metal cations (*e.g.* Mn^{2+} *vs.* Mg^{2+}) significantly affect catalytic activities of DNA enzymes as well as strand displacement reactions. Manganese ions have several times greater k_1 , k_2 , and k_3 than Cd^{2+} and Mg^{2+} , facilitating the single turnover reaction rate greater than 0.1 s^{-1} at saturated concentrations. Previous studies showed that Mn^{2+} are less effective in stabilizing the DNA duplex compared to Mg^{2+} ion [171]. This results in faster displacement rates for the upper and lower recognition arms. Additionally, Mn^{2+} and Cd^{2+} have smaller hydrated ionic radii than Mg^{2+} , which may allow easier access into the reaction sites for faster cleavage reactions [178]. One would expect that other cations exhibiting superior cleavage activities to Mn^{2+} (*e.g.* Pb^{2+} for 8-17 enzymes) could demonstrate even greater translocation kinetics [158]. High temperature and high pH environments should further promote the motor kinetics. These environmental effects may be used to effectively control the motility of DNA walkers.

4.5.4 Motor Track

Our DNA walkers move along RNA-decorated carbon nanotube tracks. While it is challenging to arrange RNA strands on the carbon nanotubes precisely, the nanotubes serve as a rigid frame for the flexible RNA track. The length of nanotubes for walker experiments in this work is mostly longer than $2 \mu\text{m}$, which enables autonomous long-distance walking upon motor conjugation. Compared to other types of tracks [33,45], starting position control on the track is not required as the long nanotubes provide ample room for walking. In addition, their intrinsic near-infrared emission properties

provide a unique way to visualize the track. An alternative approach of using DNA origami may provide a means to engineer 1-, 2-, or 3-D platforms where RNA strands are planted uniformly. In such case, the walking pathways may be programmed based on the design of fuel strand arrangement [33, 45]. Both methods provide unique track properties. Fabrication of a high quality track with well-controlled mechanical, optical, and electrochemical properties is important for walker system designs. It is worth noting that the carbon nanotube track does not appear to affect DNA reaction activities significantly, as enzymatic reaction rates on the track are shown to be comparable with those from free solution ensemble measurements.

4.6 Conclusions

In this chapter, we explored the impacts of various design components on DNAzyme walker's translation kinetics. The programmability of oligonucleotides makes it possible to construct walkers with desired motility and processivity based on the design principles presented in this chapter. The conclusions from this study are also not specific for our particular DNAzyme system, but can be generalized to other systems as long as the same nucleotide chemistry, such as strand displacement and duplex dissociation, is employed as one intermediate reaction step.

The high motility DZ7 walker presented can achieve a max velocity of $\sim 1 \text{ nm s}^{-1}$, which is at least 10-fold faster than other reported DNA walkers [20, 33], but is still orders of magnitude slower than protein motors under physiological conditions [179].

To design DNA walkers that can rival the biological motors, rate-limiting reactions during the walking process need to be identified. Such intermediate steps can be replaced by new reaction schemes with faster rates. However, faster reaction rates will render the walker less processive, as the dissociation of walker leg may occur faster than association with the next intact fuel. To address this problem, we envision integrating multi-valence in walking mechanism could drastically increase walker motility while maintaining its processivity. Walker motility can be enhanced by using

multiple enzymes working in parallel, which enhances both fuel hydrolysis and dissociation rate. Meanwhile, multiple walker legs would allow shorter or even no lower arm, which speeds up branch migration process.

In the next chapter, we use sub-diffraction imaging method to identify rate-limiting intermediate reactions during a DNAzyme walker turnover. Fluorescence localisation scheme provides much more accurate walker tracking data and fuel track structure, which allows the number of rate-limiting reactions to be estimated. With the knowledge of the rate-limiting reactions, a modified multivalent walker design will be described in Chapter 6.

5. IMAGING STOCHASTIC WALKER BEHAVIOR

5.1 Introduction

DNA walkers are inspired by motor proteins and are often benchmarked with such high performance biological motors. Despite the efforts and progress made in the past decade, DNA walkers are still orders of magnitude slower than protein motors. Part of the reason for the difficulties in designing high performance DNA walkers is a lack of reliable nanometric characterization methods to probe detailed walking mechanisms.

Most DNA walkers are studied using ensemble measurements such as gel-electrophoresis [19,32,39] or Förster resonance energy transfer (FRET) [20,180] which cannot resolve the behavior of individual walkers. More advanced single molecule techniques including fast-scan AFM [45, 181], single-molecule FRET [50, 51] and single-particle tracking [33, 35, 56] have recently been demonstrated in the study of DNA walkers. However, the small physical dimension and slow kinetics have rendered such techniques with limited precision, and have limited the use of direct tracking techniques typically used in biological motor protein studies [59, 73].

In the previous chapter, we described a DNA walker system which integrates the biochemical functionality of DNA with the optical properties of nanomaterials. Fluorescent imaging using signals from the walker itself is applied to study walker translocation kinetics [182]. The use of novel nanomaterials in walker system exploits its excellent photo-stability and tunable emission properties. Various methods have been used to interface optical nanomaterials with DNA molecules [110,111,131,183], making such materials integral parts of the walker system. With the advent of sub-diffraction imaging techniques in recent years, we anticipate that fluorescent imaging will be able to resolve the structure and kinetics of DNA walker system with unprecedented details.

In this chapter, we provide an imaging system for visualizing slow-moving DNA walkers with high precision. Multi-color sub-diffraction imaging and tracking resolves the structure and motility of the walker system. Distribution of displacement, velocity, and kinetic fluctuation are extracted from the imaging data to reveal detailed walking mechanism. We demonstrate that nanometric fluorescent imaging on DNA walkers can be used to study the stochastic behavior of the walker kinetics.

5.2 Scheme and Methods

All DNA and RNA sequences are purchased from IDT and used as received. The detailed sequences are listed in Table 5.1. All reagents are purchased from Sigma-Aldrich unless otherwise noted. All solution samples and buffers are prepared in deionized (DI) water.

5.2.1 DNA/nanotube Walker System

The walker system is constructed from a DNzyme walker strand decorated CdTe/CdS QD conjugated to RNA fuel functionalized SWCNT track (Figure 5.1a) [35]. Both SWCNT and QD are optical nanomaterials that serve as probes for reporting system status. QD with visible emission signatures works as a cargo that shows the walker location. The NIR emitting, π -electron-rich SWCNT provides a rigid track for the self-assembly of RNA fuel strands. Before mixture of the cargo and track, oligonucleotides serve as surfactants that keeps both optical nanomaterials stable in solution. Upon conjugation, the track and cargo are linked through the complementary base pairing of nucleotide strands on the SWCNT surface which are then activated to function as a walker system.

Both the walker and fuel strands consist of three parts: nanomaterial affinity region that interacts with QD or SWCNT, recognition arm for complementary base-pairing, and enzymatic reaction region that undergoes chemical cleavage in the pres-

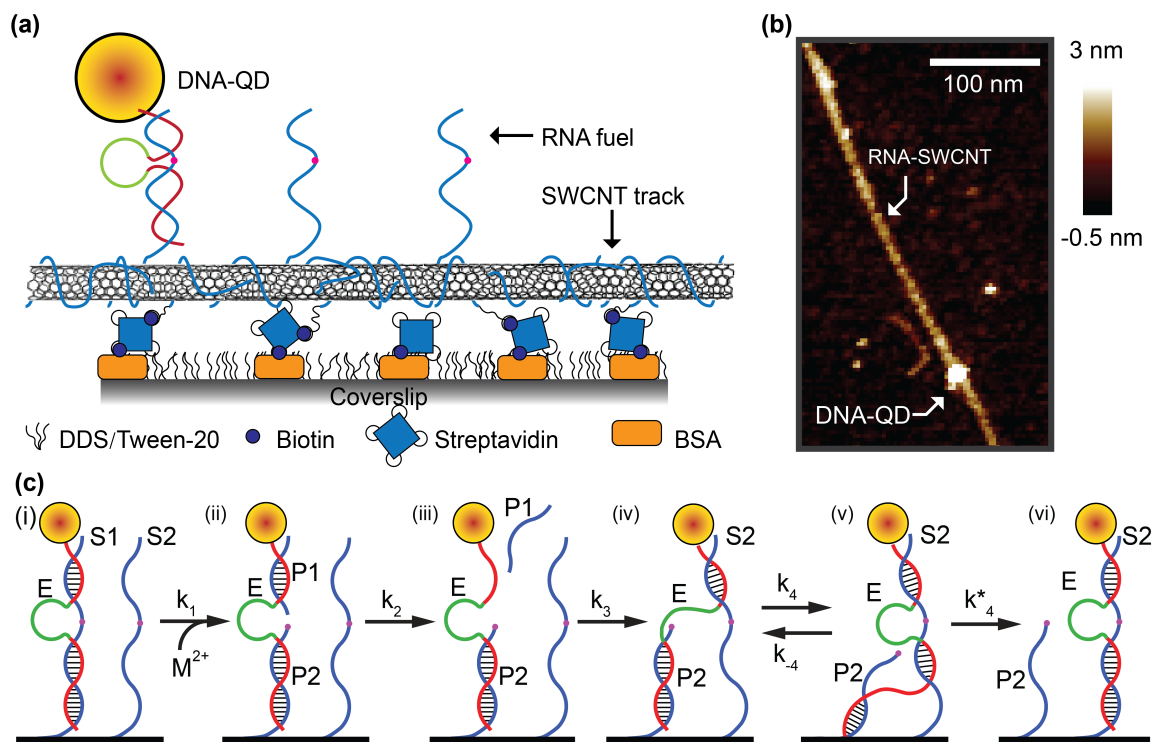


Figure 5.1. Schematic of the DNAzyme walker walking mechanism. **(a)** Scheme of a DNAzyme walker on a coverslip for imaging. Biotin-BSA is attached to the coverslip, serving as anchors for nanotube track. The coverslip is passivated by DDS-Tween 20 to prevent non-specific interaction with the walker strand. 3' biotinylated RNA and RNA fuel strands functionalized carbon nanotube binds to the surface through streptavidin. CdTe/CdS quantum dots with functionalized by DNAzyme walker strands conjugate to the immobilized nanotube track through complementary base-pairing. **(b)** An AFM image showing the walker system presented in **(a)**. **(c)** Reaction steps during DNAzyme single turnover. The walking process has similar principles as presented in Figure 4.1 with more detailed intermediate reactions for optical identification.

Table 5.1.
Sequence information for DNAzyme walker and RNA fuel.

Item	sequence ^a
10-23 DNAzyme	5'-AGT GCT GAT TCG GAC AGG CTA GCT ACA ACG AGA GTG ACT TTT T T*T*T* T*T*T*-3'
10-23 RNA fuel	5'-GTC ACT CrArU GTC CGA ATC AGC ACT TTT TAT TAT TAT TAT-3'
DZ7 DNAzyme	5'-AAT CGC AAG AAT CGG CAC GGC GGG GTC CTA TGT GGA GAC ACC TTT AGG TAA GGT GTG CAC GGA TTT T*T*T*T*T*T*-3'
DZ7 RNA fuel	5'-TCC GTG CTrG TGG TTC GAT TCT TGC GAT TTT TAT TAT TAT TAT-3'
Biotin strands	5'-GTG TGT GTG TGT GTG TGT GT/-3Bio/-3'

^aThe asterisk sign denotes phosphorothioated bases.

ence of divalent metal cations. For the DNA walker strand, the QD affinity region is realized by the phosphorothioation of the phosphate backbone for 5 bases' length. The thiol groups on the DNA back bone forms coordination complex with Cd^{2+} during QD crystal growth, thus remains integrated into the CdS shell layer of the QD [110,111]. For the RNA fuel strand, oligonucleotide motifs that selective binds to carbon nanotubes [131,183] are used as affinity region to achieve a higher degree of SWCNT surface functionalization and reduce interaction between the SWCNT surface and enzymatic functional region on RNA fuel.

The DNAzyme walker system operates by cycling through free energy cascades (Figure 5.1c) [165]. When a DNAzyme walker strand (E) is hybridized with a fuel strand (R), it cleaves the RNA substrate at the presence of divalent cation (M^{2+}), thus lowering the overall system free energy. The cleaved DNAzyme/RNA complex

(EP1P2) are thermodynamically less stable than binding with a new intact RNA fuel strand, thus the walker system goes under spontaneous branch migration from the cleaved fuel strand to the adjacent intact fuel strand (ES2P2 in state (iv) and ES2 in state (vi)), completing one single turnover reaction (*i.e.* one step forward). The walker repeats this process, resulting in a 1-D walking along nanotube track.

In the previous chapter, we have demonstrated the use of various RNA cleaving sequence as the enzymatic core and the effects of different arm length on walker kinetics. In the current chapter we use two types of DNAzymes: 10-23 and DZ7 with fixed 7/16 arm length.

5.2.2 Walker System Synthesis

The RNA covered SWCNT track and QD linked DNAzyme walker are synthesized using the methods described in Chapter 2. (7,6) enriched CoMoCAT SWCNT powder is used to make RNA-SWCNT sample. To maintain a relatively uniform track length, we performed additional length sorting to obtain sample enriched with *c.a.* 500 nm long tracks [184] (Figure 2.1). All inert PEG molecules are removed during RNA-SWCNT sample immobilization onto coverslip surface.

Aqueous synthesis of QD nanocrystals with excellent quantum yield and photostability have been reported previously [110–112]. We modified those synthesis routes to generate DNAzyme functionalized CdTe/CdS nanocrystal QDs. The detailed synthesis protocol and optical properties are described in Chapter 2.

5.2.3 Optical Platform

The schematic of imaging system is shown in Figure 5.2. Two diode lasers (405 nm and 658 nm) from Laserglow are coupled to a Carl Zeiss Microscope through optical fibers. A custom made filter cubes with two bandpass filters and a dichroic beam splitter are placed at the backport of the microscope for simultaneous introduction of both laser lines. The excitation lights are focused onto the sample through a $63\times$

Zeiss plan-apochromat objective. The power of the excitation light at the sample stage is measured by a power meter (Newport Inc) which yields 50 mW for 658 nm excitation and 2 mW for 405 nm excitation. Emission light from the sample is separated into two light paths (VIS and NIR). The VIS path is directly imaged by Andor iXon 3 EMCCD camera after tube lens and emission filters. The NIR path has an additional 2 \times magnifier inserted to achieve better resolution of the nanotube image. A cryogenically cooled InGaAs 2D array (Princeton Instrument) is mounted at the image plane of the NIR path. All the instruments are controlled by a computer with self written control scripts [185]. The images from the two cameras are registered to each other through a transformation matrix, which is obtained by imaging the same area of a microruler before each experiment.

5.2.4 Walking Experiment Procedure

After surface preparation procedure described in Chapter 2, Length fractionated RNA-SWCNT stock solution is diluted 10 times in PBS buffer and introduced into the flow channel. After 20 min incubation, 200 μ L of PBS buffer was introduced to wash away unbounded RNA-SWCNT and other impurities (*e.g.* PEG molecules). The DNA-QD stock solution is diluted 10,000 times in PBS buffer containing 20 mM dithiothreitol (DTT). The presence of DTT improves the photostability and emission efficiency of both SWCNT and QD [186, 187]. The diluted DNA-QD solution is continuously flowed into the channel and imaged until sufficient conjugation spots are present. The channel is then washed by PBS buffer containing desired concentration of metal cation and 20 mM DTT to remove unbound QDs. Both NIR and VIS images are acquired simultaneously under 1000 ms integration time. A typical experiments last about 1 hr with 20 s image acquisition interval to avoid excessive photo-bleaching of both fluorophores.

After each walking experiment, the PBS buffer (pH 7.5) in the channel was exchanged with a lowered pH PBS buffer (pH 6.0). The removal of DTT and lowered

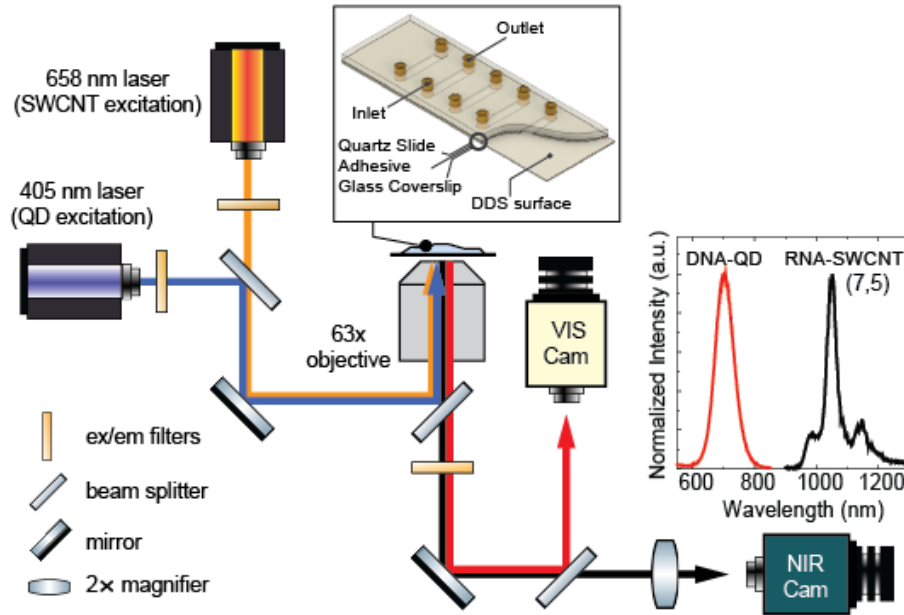


Figure 5.2. Experimental setup and imaging scheme. Optical image system setup. Output of two laser lines are passed through clean-up filters and directed into the backport of the microscope. A diaphragm in the reflected light channel is used to modulate the excitation intensity. The excitation beams are focused onto the sample stage through a 63 \times objective lens. Emission light from the sample are separated into two light paths (NIR and VIS) and imaged using corresponding cameras. The emission spectra of both QD and SWCNT are shown above the camera image. A 2 \times magnifier lens is placed in the NIR light path before the camera. Scale bars are 500 nm.

pH will enhance emission intensity fluctuations of SWCNT (Figure 5.5c-d), thus provide means for sub-diffraction image reconstruction [188]. The images are recorded at 1,000 ms integration time for up to 5,000 images.

5.2.5 Subdiffraction Tracking of Walker

All experimental images are processed in ImageJ using custom written scripts. Both drift correction and Gaussian fitting are adapted and modified from GDSC

SMLM plugin (<https://github.com/aherbert/GDSC-SMLM>). The registration of QD image and SWCNT image through a transformation matrix is accomplished by using a previously published intensity based registration method [189]. The same transformation matrix is used throughout the entire experiment to avoid any errors introduced due to camera alignment.

Correction on stage drifting during the experiment span is particularly important for imaging slow moving DNA walkers [56,190]. Sample drift caused by mechanical relaxation of the stage is significant in our walking experiment as a result of the long experimental time. We used the NIR image of the nanotubes as fiduciary markers to correct the drift in the VIS image. The (x,y) positions of RNA-SWCNTs are first approximated by finding their maxima in each frame. The sub-diffraction positions of SWCNTs from 10 consecutive images are then grouped to form an image set. The drift between each image set and the average positions of all the captured images are calculated using a correlation analysis over the entire image. The process is repeated till converge and the drift from each iteration is combined to generate the final correction curve. The correction values are then applied to translate the VIS image. The drift correction scheme can achieve a localization accuracy of ~ 50 nm.

The (x,y) position of a QD is obtained by fitting its PSF to a Gaussian function. The precision σ of the fitting can be theoretically calculated by Equation (5.1) [58,59]:

$$\sigma = \sqrt{\frac{s^2}{N} + \frac{a^2/12}{N} + \frac{8\pi s^4 b^2}{a^2 N^2}} \quad (5.1)$$

where s is the standard distribution of the Gaussian distribution, a is the pixel size of the iXon 3 camera, b is the background noise level and N is the number of photons collected. Under our experimental condition, $a = 232\text{nm}$, $s = 115\text{nm}$, $b \approx 65$, $N \approx 1,000$, which yields a localization precision $\sigma \approx 20\text{nm}$.

To achieve the theoretical value of precision from the drift corrected image, we performed additional corrections by subtracting the displacement of stationary QDs from that of the moving QDs. The drift corrected image is segmented into multiple areas, each of which containing only one QD. All the sub-image areas are categorized

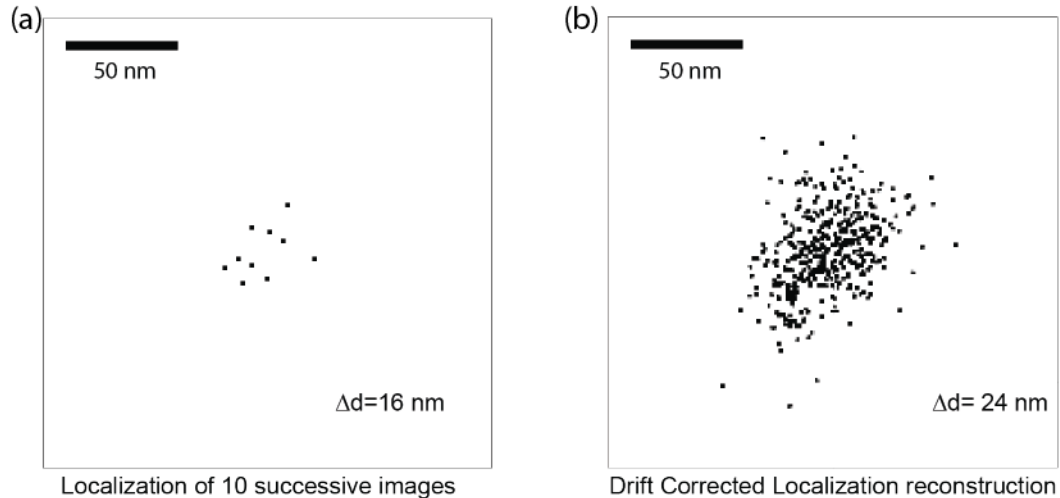


Figure 5.3. Characterization on the localization and drift correction precision. QDs and SWCNTs are fixed onto a non-passivated surface and imaged in $1\times$ PBS buffer and 20 mM DTT. The images are continuously acquired at 1 s integration time and 5 s measurement interval. A total of 500 images are acquired analyzed. **(a)** Precision of QD localization. Centroids of Gaussian fitting of 10 successive frames are shown. The precision of localization is measured by the standard deviation $\Delta d \approx 16$ nm from the mean position of the 10 fitting. **(b)** Precision of drift correction on QD image. The drifting of QD image due to stage relaxation is corrected by subtraction the drifting traces of the NIR images of the nanotube and the average drifting of other QDs. Centroids of Gaussian fitting of all the frames after drift correction are shown. A standard deviation of $\Delta d \approx 24$ nm is obtained.

into two groups: conjugated and non-conjugated with RNA-SWCNTs. The average position difference between frames of the non-conjugated QDs are subtracted from the position changes of the conjugated QDs. This result in an experimental localization precision of ~ 30 nm as shown in Figure 5.3. The final positions of the QDs are subsequently used for kinetics analysis.

5.2.6 Subdiffraction Imaging of Nanotubes

The NIR images of RNA-SWCNTs are first drift corrected using the previously mentioned scheme. After drift correction, the fluctuation in intensity is obtained by subtracting an image from its successive frame. The pixel values of resultant difference images are then all converted to positive integers for Gaussian fitting. According to Equation (5.1), the localization precision in the NIR range is *c.a.* 100 nm, which is about 1/10 of the emission wavelength. Fitting results from all images are combined to reconstruct the nanotube image (see Figure 5.5 for more details).

5.2.7 Walker Data Analysis

The coordinates of the first 10 localizations of QD images are averaged as the origin position of the walker. Based on the average velocity, the distance traveled by the walker in this period is about 20 nm, which is within the 30 nm localization precision of our platform.

The translocation distance $d(t)$ of the walker is calculated by Equation (5.2):

$$d(t) = \sqrt{(x(t) - x_0)^2 + (y(t) - y_0)^2} \quad (5.2)$$

A rolling smoothing with a window size of 10 data points is applied to the displacement data so that noise can be averaged out. The displacement of all the experimental cases used are plotted in Figure 5.3.

The mean squared displacement is calculated by Equation (5.3):

$$MSD = \langle d(\delta t)^2 \rangle = \frac{1}{T} \sum_{t=1}^{t=T} d(\delta t)^2 \quad (5.3)$$

where δt is the lagtime and T is the last time point available for time average. Time averaged MSD from different cases are ensemble averaged to obtain the final experimental value for one experimental condition (black squares in Figure 5.7.) The MSD is fitted with a power-law time dependence $MSD = At^\alpha$. The scaling exponent $\alpha = 1.72$ is obtained from least square fitting.

The randomness parameter r is computed using Equation (5.4):

$$r = \frac{\langle \tau^2 \rangle - \langle \tau \rangle^2}{\langle \tau \rangle^2} = \frac{\langle d(t)^2 \rangle - \langle d(t) \rangle^2}{t} \frac{1}{l \langle v \rangle} \quad (5.4)$$

where $l = 4$ nm is the spacing between two fuel strands. The velocity $\langle v \rangle = \langle d(t) \rangle$ is obtained by first fitting the displacement data in every 500 s. The histogram of the velocity is approximated by a normal distribution to yield a mean velocity of $\langle v \rangle \approx 0.13$ nm/s. The slope of the displacement variance increase with time is used for the term $\langle d(t)^2 \rangle - \langle d(t) \rangle^2/t$. All the quantities are also calculated in the same way for simulated walking data, which is described in the next section.

5.2.8 Simulated Walking

The process of DNAzyme strand walking on nanotube surface can be modeled as a 1-D biased continuous time random walk process. Consider a walker strand just hybridized with a RNA substrate. The right side of the walker strand has intact fuel strand anchored periodically by a distance l , while the left side of the walker are the areas previously explored by the walker strand. Assuming a linear track on the nanotube side wall, the displacement $d(t)$ of the walker is calculated by the total number of steps in the given amount of time t :

$$d(t) = \sum_{i=0}^{N(t)} \chi(\tau_i) l + \sigma \quad (5.5)$$

$$t = \sum_{i=0}^N \tau_i \quad (5.6)$$

where $N(t)$ denotes the number of stepping events occurred during time t , and l is the average spacing of fuel strand on the SWCNT surface. The term σ is a Gaussian noise due to Brownian motion and experimental uncertainties. $\chi(\tau_i)$ is a function that indicates step direction with the form:

$$\chi(\tau_i) = \begin{cases} 1 & \tau_i = \tau_f \\ -1 & \tau_i = \tau_r \end{cases} \quad (5.7)$$

Here τ_i is the dwell time in-between two stepping events. τ_f and τ_r are the single turnover time generated by the simulation for forward or backward stepping. The distribution of dwell time is determined by the nature of the biochemical reaction related to a single stepping turnover [191]. For a single turnover event with n rate limiting intermediate steps of similar rate k , the distribution $p(\tau_i)$ follows a gamma distribution:

$$p(\tau_i) = \frac{k^n \tau_i^{n-1}}{\Gamma(n)} e^{-k\tau_i} \quad (5.8)$$

where $\Gamma(n)$ is the gamma function equivalent to $(n-1)!$. In simulation of walking process, we define the dwell time τ_i as the smaller amount of τ_f and τ_r (*i.e.* $\tau_i = \min(\tau_f, \tau_r)$). The value of τ_f and τ_r are generated by random numbers following gamma distribution. For τ_f , we use different combinations of (n, k) but with same mean value for the gamma distributions that the average single turnover time τ_f will remain the same. (see Figure 5.4a) A average value of $\langle \tau_f \rangle = 30$ s is used based on the experimentally determined average velocity $\langle v \rangle = 0.13$ nm s⁻¹ and fuel spacing $l = 4$ nm. For τ_r , a single step Poisson distribution with $\langle \tau_r \rangle = 300$ s is used as a back-step to the cleaved strand is much slower compared to the forward step.

For each case of the (n, k) combination, 500 steps are run for each walker and traces from 100 walkers are aggregated to produce the displacement plot shown in Figure 5.4a. The error bar in Figure 5.4a also indicates the variance from all the traces within one case of (n, k) combination used. The Displacement variance in plotted in Figure 5.4b. It is evident that even though the displacement is similar, the different number of rate limiting steps within a single turnover can be retrieved from the variance of the displacement.

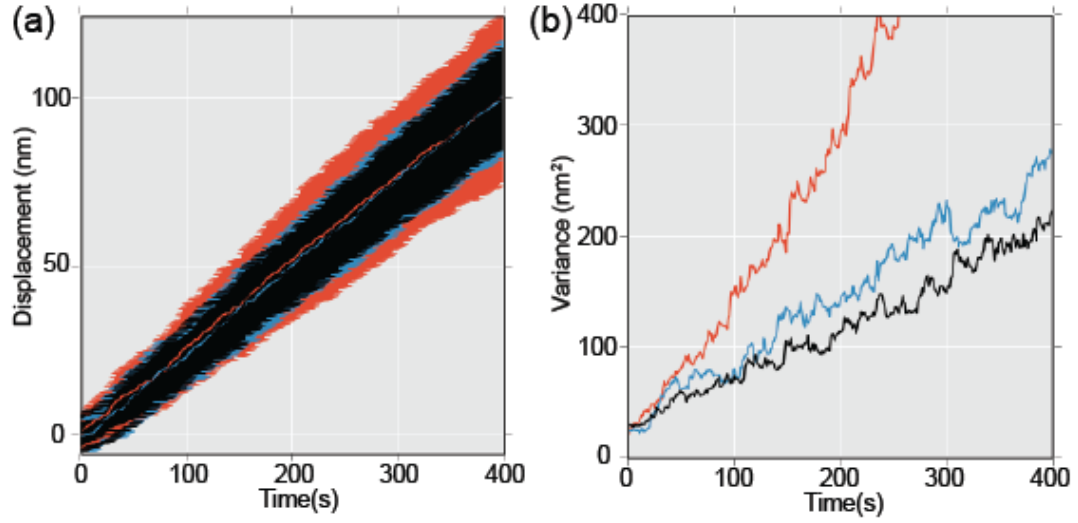


Figure 5.4. Simulated translocation of DNA walker. 3 sets of (n, k) combinations are tested with 500 steps for each walker and 100 walkers for each case. Different cases are color coded as follows: red : $n = 1$; blue : $n = 2$; black : $n = 3$. **(a)** Averaged displacement. **(b)** Displacement variance of all walkers.

5.3 Results

5.3.1 Visualizing Nanoscale Structure and Motion

Nanometric optical imaging on DNA walkers bears resemblance to typical single particle tracking (SPT) experiments, but requires additional features for the imaging platform. In both cases the position information is extracted by approximating the point spread function (PSF) of the fluorescent probe to a 2-D Gaussian function. The localization precision on the particle's position is determined by the signal intensity, noise level, camera pixels and the fitting algorithm used (see Equation (5.1)) [58, 59, 192]. Compared to protein motors studied in SPT experiments, typical DNA walker systems have much lowered translocation velocity and shorter travel distance. This leads to small position difference in-between measurements and

long overall experimental time. The small translocation distance requires high precision in position measurement. Researchers have demonstrated imaging with several nanometer precision by achieving a high signal photon count [59,187]. The long overall experimental time requires photo-stable fluorophores as well as mechanically stable hardware setup to minimize uncertainties associated with photo-bleaching and stage drifting. Efforts on the long term tracking on DNA walkers have been demonstrated using Cy3/Cy5 dyes as optical probe/marker with a high concentration of oxygen scavenger system that prolongs the emission signal from the probes [33,56].

The emissions from both fluorophores are imaged by a custom built epifluorescence system as shown in Figure 5.2. An EMCCD camera and an InGaAs 2D array are used so images from both visible (VIS) and NIR channels can be acquired simultaneously. The processing schemes for both VIS and NIR channels are shown in Figure 5.5. QD images from the VIS channel is localized by fitting Gaussian function to its PSF. The localized QD image is then combined with the 10 successive localizations to form a single sub-diffraction estimation on the QD position (Figure 5.5b). According to Equation (5.1), the precision of a single localization is approximately 20 nm, which agrees with the standard deviation of the 10 localizations Figure 5.5b.

The NIR image of nanotube track is resolved to 100 nm, which is approximately $\lambda/10$ of the nanotube's emission wavelength. The nanotube image is a concatenation of all exciton recombination centers along nanotube axis. Temporal separation of such emission centers can be achieved through emission intermittency at low pH (~ 4) for surfactant solubilized carbon nanotubes [188]. Such fluctuations in emission intensity is a result of protonation/deprotonation reactions on the nanotube surface that interfere with radiative exciton recombination process. Compared to surfactant solubilized nanotubes, our RNA-nanotube complex has a lower degree of surfactant coverage [193,194], thus the nanotubes are more susceptible to the local dielectric environment. We observed intensity fluctuation at pH 6 in PBS buffer (Figure 5.5e). The underlying nanotube surface reaction centers are localized by constructing the difference image of consecutive frames and fitting the isolated PSF with Gaussian

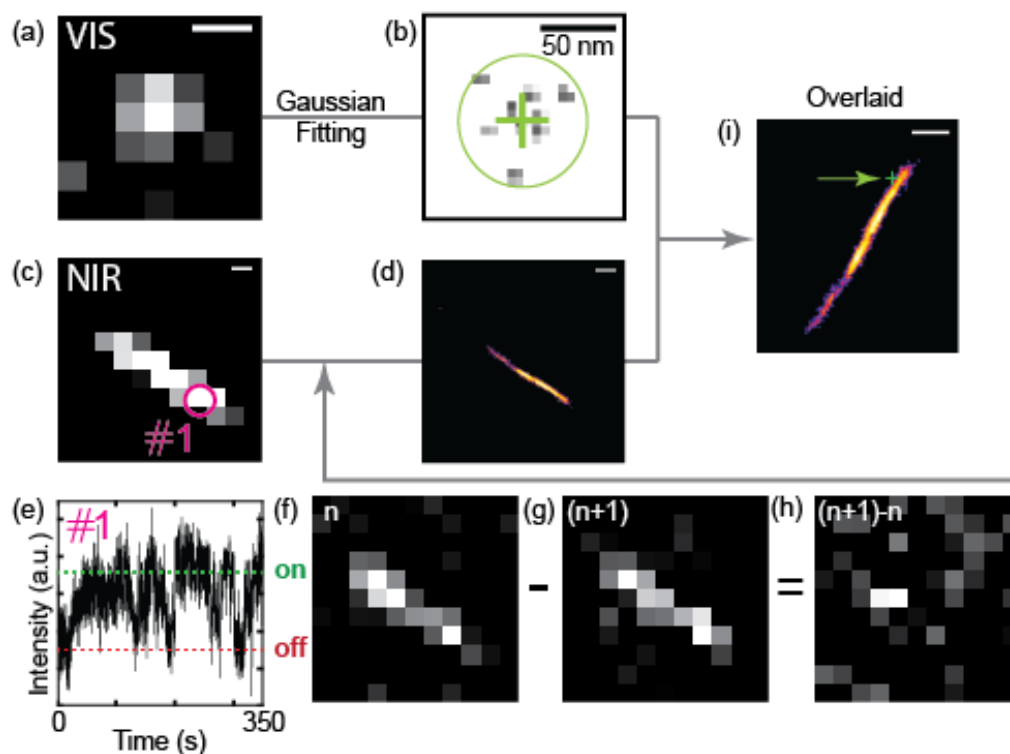


Figure 5.5. Sub-diffraction imaging scheme for both VIS and NIR images. (a)-(b) Gaussian fitting of QD PSF is used to estimate its centroid. The average result from 10 localizations are used as the final position. (c)-(h) the intensity fluctuation of the pixel labeled #1 in a NIR nanotube image (c) is presented in intensity vs. time plot (e). The reaction center of such intensity change is isolated by constructing difference image of successive frames ((f)-(h)). The separated PSFs are localized to reconstruct the sub-diffraction nanotube image (d). The localized VIS and NIR images are registered to produce the overlaid image (i). The QD position is emphasized by a green arrow. Scale bars are 500 nm.

function (Figure 5.5e-h). The combination of all the localized surface reaction centers thus reconstructs a sub-diffraction image of the nanotube as shown in Figure 5.5d. The NIR and VIS image are registered to the same set of coordinates to construct the final overlaid image Figure 5.5(i).

Figure 5.6 shows a representative result of a DZ-7 walker traveling over 200 nm in 10 min. The walkers are imaged in $1\times$ PBS buffer containing 20 mM DTT and 10 mM Mg^{2+} using the previously described localization and drift correction scheme.

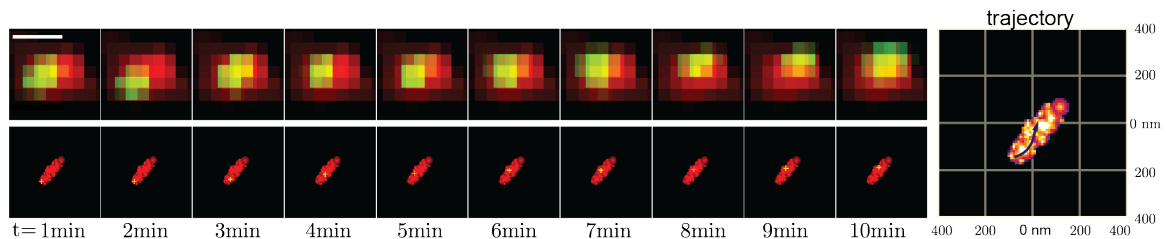


Figure 5.6. Raw and sub-diffraction images of a DZ-7 enzyme walker operation in $1\times$ PBS with 10 mM Mg^{2+} and 20 mM DTT. The walker travels approximately 200 nm in 10 min. The images are taken at a 5 s interval and localized using the scheme shown in Figure 5.5. The walking trajectory is plotted in a 400 nm \times 400 nm grid for better visualization of the distance. The scale bar is 500 nm.

5.3.2 Displacement and Velocity Distribution

Position information is extracted from raw image to produce the displacement shown in Figure 5.7a. Representative result of the displacement of 10-23 walker moving under 10 mM Mg^{2+} condition (blue scatter) and 10-23 walker under 0 mM Mg^{2+} (black scatter) are shown. The positions from successive 10 frames are averaged using the previously discussed scheme to produce the smoothed curve (blue and black lines). Additional displacement curves under similar experimental conditions are shown in Figure 5.8. Walker velocity is obtained by fitting the displacement curve for

every 500 s segment. The velocity distribution is fitted to a Gaussian function and a mean velocity of $\sim 7.8 \text{ nm nm s}^{-1}$ is obtained.

Further details on the walkers' translocation mode can be investigated from MSD. The walker strand binds to an intact fuel strand with a faster rate and higher probability, thus the walker is biased to move away from random diffusive motion to a directed translocation. The nature of such walking scheme is reflected in the power-law form of MSD [195, 196]: $\langle d(\delta t)^2 \rangle = At^\alpha$. Different mode of motion can be categorized by the MSD scaling exponent α : for confined motion such as proteins crossing cell membrane [197], $0 \leq \alpha \leq 1$ (sub-diffusive); for random diffusion, $\alpha = 1$; for active process such as transport by intracellular motor proteins [198], $1 \leq \alpha \leq 2$ (super-diffusive). Figure 5.7c shows the time averaged MSD (black lines) and ensemble averaged MSD (black scatter) constructed from the smoothed curve from the displacement plot. A power function (red line) is fitted to the experimental data which gives $\alpha = 1.72$. A linear fitting of the first 10 scatter points (blue line) is also included to better visualize the clear curl-up shape of the walker MSD. We performed numerical simulations based on the proposed walking mechanism with kinetic rates similar to the experimentally obtained values (see subsection 5.2.8). The power law dependency of the MSD shown in Figure 5.7c is consistent with that generated by simulations.

5.4 Discussion

A walker system turns biochemical reactions into processive operations, accumulating the individual single turnovers to produce net results that can be measured by experimental techniques. In our DNA walker system, displacement and velocity provide good measure on processivity and motility. Assuming the mean step length exists, the displacement gives the average number of single turnover events, while the velocity gives the average single turnover reaction rate [182].

Further understanding on the nature of such walking process, however, requires more detailed information beyond averaged kinetics. A typical value used to char-

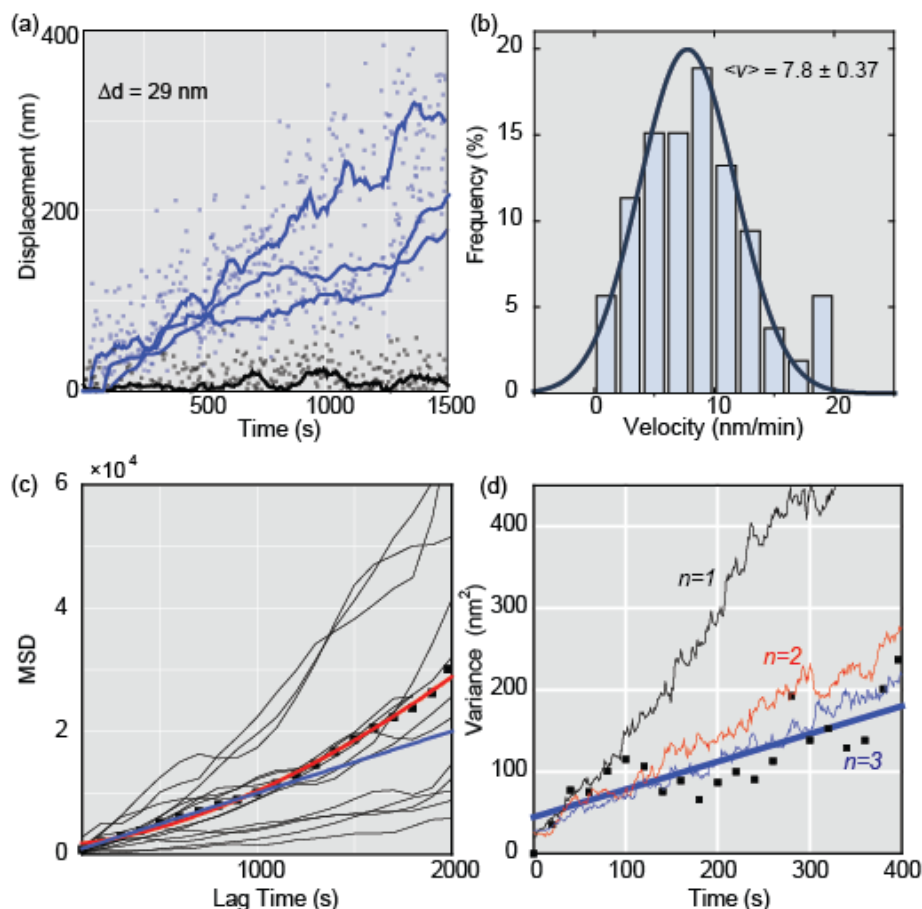


Figure 5.7. Quantitative evaluation of a 10-23 enzyme walker. **(a)** Displacement of the 3 walkers (blue scatter) as compared to control experiment (black scatter). The smoothed displacement from averaging successive 10 localizations is plotted as a solid curve. Control experiment is conducted without any Mg^{2+} . **(b)** Velocity distribution of DNAzyme walkers generated from data shown in Figure 5.8. The histogram is fitted to a Gaussian distribution with mean value $\sim 7.8 \text{ nm min}^{-1}$. **(c)** Walker MSD. Black lines are the time averaged MSD from a single walker trajectory. Black scatters are ensemble averaged data. The MSD is fitted to a power-law function with a scaling exponent $\alpha = 1.72$. The first 10 scatter points are linearly fitted (blue line) and extended for better visualizing the deviation of walker MSD from diffusive motion. **(d)** Displacement variance of experimental (black scatter) and simulated data (line). 3 cases with different intermediate reaction numbers, $n=1$ (black), $n=2$ (red), $n=3$ (blue), are presented. Linear fitted (blue line) line was used to determine the slope of ~ 0.34 .

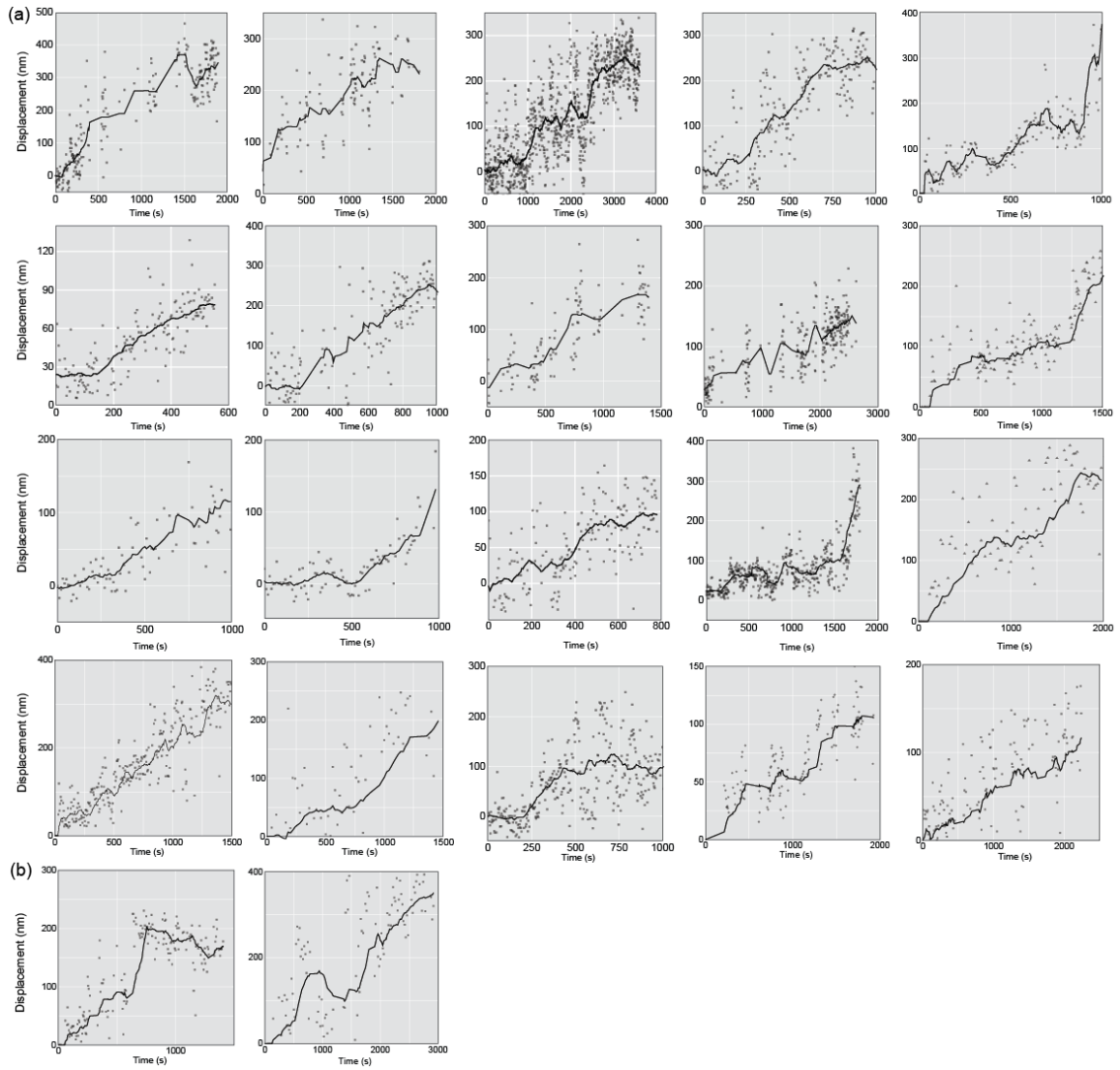


Figure 5.8. Displacement plots of all datasets used in this study. All the traces are obtained from experiments of 10-23 DNA enzyme decorated QD moving along a carbon nanotube in $1\times$ PBS, 10 mM Mg^{2+} and 20 mM DTT. Localizations from a single frame is plotted as scatter points and the average position from 10 localizations are plotted as a smoothed curve. **(a)** Displacements showing processive walking. These datasets are used in the analysis for displacement variance, velocity distribution, and MSD. **(b)** Displacements showing stalling and back-stepping due to possible assembly defects on the nanotube surface. These datasets are excluded from our analysis.

acterize enzymatic reaction is the single turnover waiting time τ and its statistical distribution $P(\tau)$. For example, the knowledge of such distribution helps determine kinetic intermediates in one single turnover reaction [191], or uncover the dynamic disorder of an enzyme's catalytic rate [154,199]. For DNA walkers, these insights shed light on detailed walking mechanisms that help to answer questions such as whether the presence of nanomaterials interfere with walking process, or whether the cargo rolls over the track instead of walking. We analyzed the fluctuations of the walker displacement as a starting point to address such questions. Instead of using $P(\tau)$ directly, Schnitzer and Block [155,179] proposed using the moments of $P(N,t)$ to study the fluctuation of a processive enzyme. Here $P(N,t)$ denotes the probability of N single turnover events happened in time t . In more details, the displacement of a DNA walker follows Equation (5.9):

$$d(t) = Nl + \sigma \quad (5.9)$$

where l is the step length and σ is the noise term due to Brownian motion. At single molecule level, the random variable N and its statistical distribution $P(N,t)$ determine all the characteristics of walker behavior. When only one rate-limiting reaction is present in a single turnover event, $P(N,t)$ follows Poisson distribution. The distribution becomes complicated when n rate-limiting reactions with similar reaction rate k_i are present. Despite the complexity of $P(N,t)$, its moments can be deduced without the knowledge of the exact distribution. The moments of $P(N,t)$ reveals important kinetic information. For example, the average displacement $\langle d(t) \rangle = \langle N(t) \rangle$ can be obtained by having the first moment of $P(N,t)$: $\langle N(t) \rangle = t/T_0 = k_i t l / n$. Similarly, the variance of the walker displacement can be obtained by the second moment of $P(N,t)$:

$$Var[d(t)] = \langle d(t)^2 \rangle - \langle d(t) \rangle^2 \quad (5.10)$$

$$= \frac{d^2}{T_0} \frac{1}{n} t + \langle \sigma^2 \rangle \quad (5.11)$$

It can be seen that variance of the displacement contains information on the number of rate limiting steps. Non-dimensionalize Equation (5.11) gives the randomness parameter r , which is a measure of the kinetic fluctuation of the walker [200]:

$$r = \frac{\langle d(t)^2 \rangle - \langle d(t) \rangle^2}{t} \frac{1}{l\langle v \rangle} = \frac{1}{n} \quad (5.12)$$

Thus, measurement of the walker displacement variance and velocity provides an estimation on the number of rate-limiting steps n [155].

To confirm the robustness of the fluctuation analysis on walker kinetics, we performed numerical simulations to test the robustness of the fluctuation analysis method (see subsection 5.2.8). When multiple rate limiting steps with similar reaction rate are present in a single turnover, the waiting time follows a gamma distribution [191]. We used gamma distributions with different shape and scale parameters but same mean value to generate waiting time distributions in simulated walking. Displacements variance from 100 runs for each case are presented in Figure 5.7 (thin lines in different colors). As back-stepping, stalling and sudden hopping reflect defects in particular samples rather than the nature of the walking process, we selected short walking distance (~ 400 s) and processive walker trajectories for the analysis of displacement variance. The scatter points in Figure 5.7d shows the experimentally obtained displacement variance. A linear fitting of the experimental data yields randomness parameter $r = 0.34$ and $n \approx 3$. This result is consistent with the proposed mechanism as shown in Figure 5.1b, which indicates that the DNAzyme decorated QD indeed walks processively along the nanotube.

5.5 Conclusions

The DNAzyme walker benefits from the specificity and programmability of nucleotide molecules. Design improvements on such systems require characterization methods capable of probing detailed walking mechanisms. A multi-color subdiffraction imaging platform for optically tracking slow motion of DNA walkers have been presented in this chapter. We obtained walker displacements, MSD, velocity, and

the randomness parameter using the imaging platform. Three rate-limiting reaction steps are identified from the tracking data. These quantities provides useful insights on walker kinetics and help design more efficient walking mechanisms. In the next chapter, we demonstrate a new walker design by speeding up the rate-limiting reactions identified in this chapter and incorporating multi-valency into the walking mechanism.

6. PROGRAMMING 2-D MOLECULAR TRANSPORT

6.1 Introduction

Natural molecular motors play vital roles in various biological processes. At single molecule level, they transform random molecular fluctuations into directed motion with high energy efficiency. At system level, they self-assemble and operate collectively to accomplish highly diversified biological functions. For example, the axonal transport by kinesin towards synapse [201], the contraction of muscle by coordinated motion of myosin [202] and the transcription of RNA by RNA polymerase along a DNA track [203]. The ability to create synthetic versions of similar molecular motors will expand the design space for complex molecular systems with desired functions, thus providing novel tools for various applications.

In previous chapters, we developed a nanoscopic characterization system to study the mechanisms and kinetics of DNA walkers. The obtained insights allow us to effectively design and fabricate single DNA walkers with desired motility. In this chapter, we use enzymatic DNA walkers to realize 2-D super-diffusive molecular transport powered by collective operation of multiple DNA walkers. The effects of enzymatic cleavage rate, multi-valence, and sequence length on transport kinetics are explored to determine rate-limiting steps and extract design guidelines. We also devised a regulation scheme on walker activity so that more complex behaviors could be embedded into the system.

6.2 Scheme

The system consists of a DNA walker decorated fluorescent particle conjugated to RNA fuels immobilized onto a 2-D surface (Figure 6.1). The fuel strands immobilized onto the surface has a 15-nt RNA “fuel” portion (blue) and 20-nt DNA “anchor” (red).

Multiple walker strands with upper (complementary to RNA) and lower (complementary to DNA) arms associate with the surface bound fuel. We use the notation n/m to indicate n -nt upper arm and m -nt lower arm walker configuration. Active translocation is achieved by hydrolysis of the RNA fuel using enzymatic nuclease, thus driving the system away from an equilibrium state.

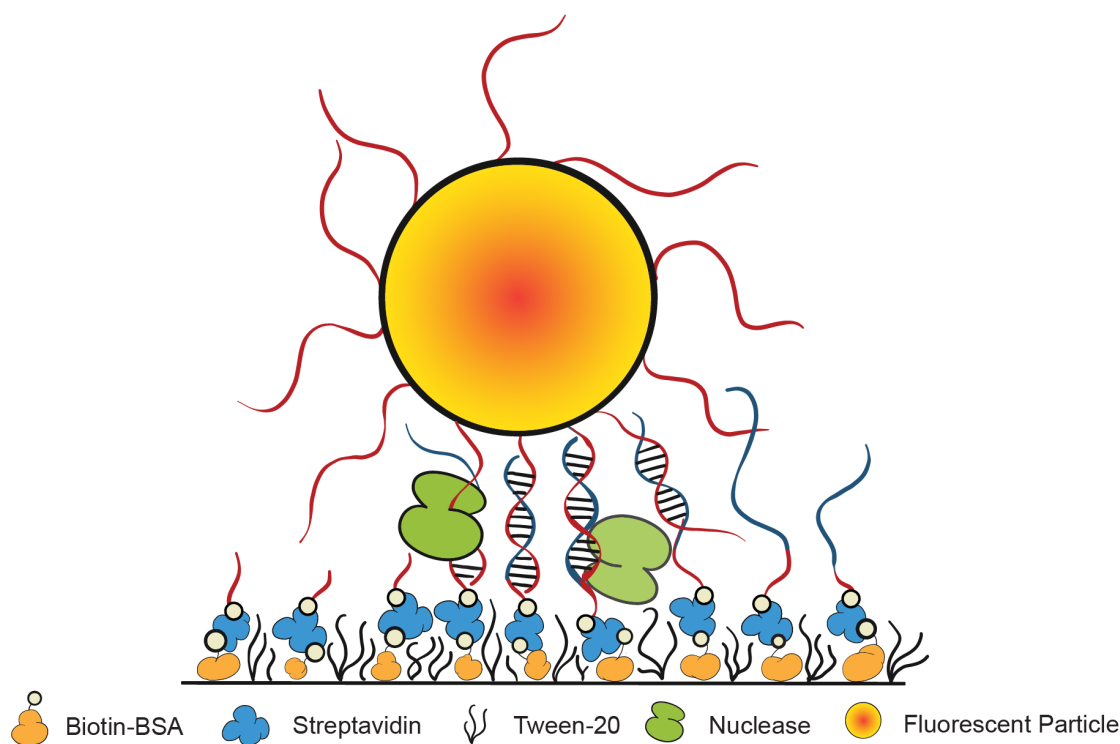


Figure 6.1. Scheme for 2-D DNA transport system. Multiple walker strands (red) are attached to a fluorescent particle. The particle is immobilized onto the imaging surface through the complementary binding of DNA walker legs with RNA fuels (blue) on surface. Multiple legs on the particle can bind to surface fuel simultaneously. The RNA fuels are grafted onto the surface through biotin-streptavidin interaction (orange-blue). The surface is passivated by BSA and DDS/Tween 20 as described in Chapter 5. Nuclease (green) cleaves the formed walker/fuel duplex, driving the walker legs to associate with intact fuel strands.

The walking mechanism using a single walker as is shown in Figure 6.2. We have shown in previous chapters that DNAzyme could achieve enzymatic cleavage at

specific position. In this chapter, we use ribonuclease (RNase) H to cleave the surface bound RNA so that the upper arm of the DNA walker strand on the particle surface becomes available for association with the next intact fuel (Figure 6.2a state (i) to (ii)). After association with the next available fuel (iii), the walker migrates gradually from the consumed fuel to the intact fuel through branch migration (Figure 6.2 state (iii) to (iv)).

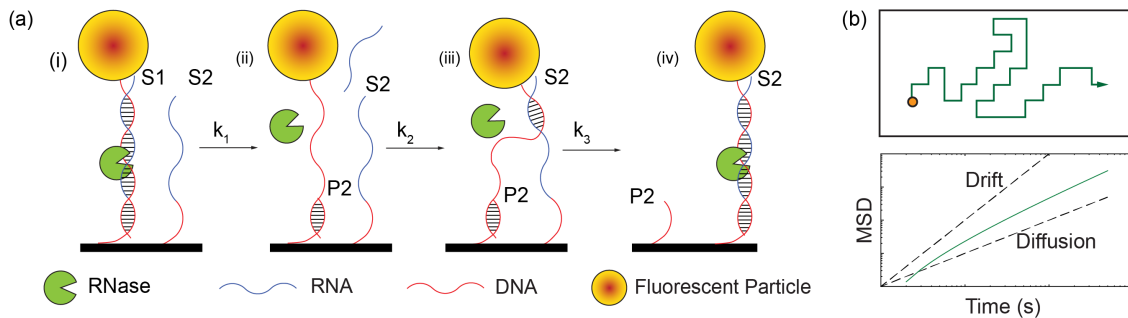


Figure 6.2. 2-D transport mechanism. **(a)** Mechanism for enzymatic DNA walker. Fluorescent particles decorated with DNA walker strands associate with RNA fuel strands on particle surface. RNase H then cleaves the RNA strands and frees part of the walker leg (state (i) to (ii)) for binding with the next available fuel (state (ii) to (iii)). After association with the next fuel, the walker detaches from the consumed fuel and gradually migrates to the intact fuel (state (iii) to (iv)). **(b)** Schematic and scaling feature of a 2-D self-avoiding walking. The walker avoids its own path, thus is biased away from random diffusion (dashed line), demonstrating super-diffusive behavior. The scaling of the walker MSD follows $t * \log(t)$ (green line).

As discussed in previous chapters, such an enzymatic reaction based walker could achieve 1-D active walking through a “Burnt-bridge” mechanism. For a 2-D system, such mechanism allow realization of a so-called “self-avoiding” walking (Figure 6.2a) [204]. This mechanism achieves active transport by prohibiting the walker from crossing its own path. As the randomness of walking is reduced due to the constraint of maintaining “self-avoiding” status, the walker demonstrates super-diffusive

behavior and explore larger area as compared to a typical 2-D random walk. The MSD scaling feature of the walker is theoretically computed to follow $t * \log(t)$ [205].

6.3 Methods

6.3.1 Walker System Synthesis

Materials All nucleotides are purchased from IDT and used without further purifications. The detailed sequence information can be found in Table Table 6.1. RNase H and EXO III and their corresponding reaction buffers are purchased from New England Biolabs. Fluorescent polystyrene (fPS) particles (680 nm emission) and streptavidin coated quantum dots (SA-QD, 705 nm emission) are purchased from ThermoFisher. PEG-500 is purchased from Layson Bio Inc. All other reagents are purchased from Sigma-Aldrich. All solution samples and buffers (MES: 50mM, pH 6.0; PBS: 50mM phosphate, pH 7.4) are prepared in deionized water.

Particle functionalization DNA walker strands modified with amine groups are grafted onto fPS particles through surface carboxyl groups. The particle concentration is kept at 0.02 g ml^{-1} in pH 6.0 MES buffer to avoid aggregation. DNA concentration is 100-folds (20 nm particle) or 100000-folds (200 nm particle) higher to PS particle concentration during synthesis. 5 mM EDC is added to the solution to activate carboxyl groups for direct reaction with primary amine on DNA strands. The mixture is incubated in dark for 2 hr. The solution is then washed by centrifugation at $20000 \times g$ for 30 mins. The supernatant is then discarded and the functionalized PS particles in the pellets are redispersed in $1 \times$ PBS buffer. The washing process is repeated 3 times. The surface DNA density on a fPS particle is converted from the concentration ratio from the purified solution. DNA and particle concentrations are measured by their respective absorption peaks at 260 nm and 660 nm using Perkin Elmer Lambda 950 UV-VIS spectrometer.

Fuel immobilization RNA fuels are immobilized onto glass coverslip surface through either biotin-avidin interaction or cross-linking with epoxy-silane. Coverslips

Table 6.1.
Sequence information for DNA walkers and RNA fuels.

Item	sequence ^a
13/0 Walker	5'- /5AmMC6/TTT TTT ATC GGT CAG GCT T -3'
13/7 Walker	5'- /5AmMC6/ TTT TTT ATC GGT CAG GCT TAG TCG TG -3'
8/0 Walker	5'- /5AmMC6/TTT TTT TCA GGC TT -3'
8/7 Walker	5'- /5AmMC6/TTT TTT TCA GGC TTA GTC GTG-3'
15/15 Walker	5'- /5AmMC6/TT TTT GCA TCG GTC AGG CTT A GTC GTG GGA GTT AA -3'
RNA fuel	5'- /5Biosg/TTT TTT TTT TGC CCC TTA ACT CCC ACG ACT rArArG rCrCrU rGrArC rCrGrA rUrGrC -3'
EXO III fuel	5'- /5Biosg/ TTT TTT AAG CCT GAC CGA T -3'
Inhibitor	5'- TTT TAG CAT CTT TGG GGG C -3'
Activator	5'- TGA CCG ATG CTA AAA -3'
RNAse FRET	5' ATC GGT CAG GCT TAG TCG TGT T /3IABkFQ/ -3' 5'- /56-FAM/ TTC ACG ACT rArArG rCrCrU rGrArC rCrGrA rU -3'
EXO III FRET	5'- /5IABkFQ/ AAG CCT GAC CGA T -3' 5'- ATC CGG TCA GGC TT /iFluorT/TTT TTT TT -3'

^arN represents RNA base.

are first cleaned by the same procedure as described in Chapter 5 and assembled into fluid channels. For immobilizing biotin modified RNA fuel strands, coverslips were first silanized with DDS. Biotinylated BSA (2 mg ml^{-1}) was then deposited onto the silanized coverslip surface. After incubation for 5 min and washing by $1\times$ PBS buffer, Tween20 (0.2 vol%) was then deposited to passivate the surface. Next, streptavidin (1 mg ml^{-1}) was conjugated to surface bound BSA-biotin to serve as anchors for biotin-RNA fuels.

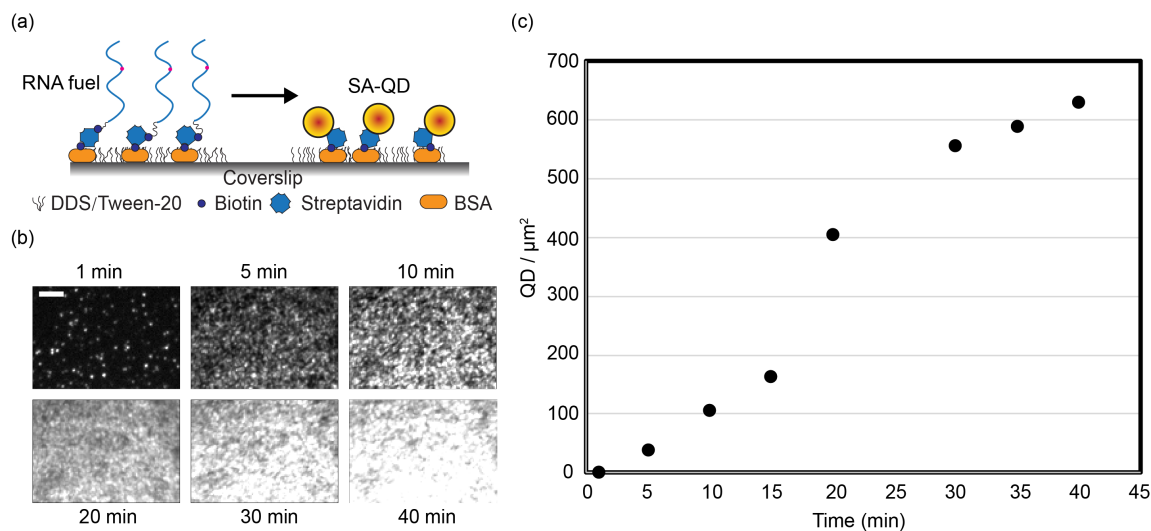


Figure 6.3. Characterization of RNA fuel density. (a) Schematic of surface characterization method. All anchoring sites for RNA fuels are labeled with SA-QDs for fluorescence measurement. (b) Fluorescence intensity of SA-QDs conjugated onto the surface over time. (c) The density increases as a function of time.

The RNA fuel density on coverslip is characterized using streptavidin capped QD (SA-QD). After biotinylated BSA after Tween 20 passivation, SA-QD were directly conjugated onto the surface (Figure 6.3 a). To quantify the fuel density, fluorescence from a single SA-QD was first estimated using sparsely labeled surface. The fuel surface was then incubated with high concentration SA-QD solution and the fluorescence intensity was recorded over time (Figure 6.3 b). The fuel density is computed using

the number of SA-QDs divided by surface area (254 nm per pixel). The saturated density value is used as the fuel density (Figure 6.3 c).

6.3.2 Imaging DNA Walking and Data Analysis

The movement of DNA walkers were imaged using the same optical setup as described in Chapter 5. A solid state diode laser (658 nm, 150 mW, Laserglow Inc) is used to excite fPS particles at a power intensity of 45 W cm^{-2} . Typical images are acquired every 200 ms for 1 hr. The acquired images of a fPS walker particle can achieve > 10000 photons with a background noise level of ~ 10 photons.

The recorded images are processed in ImageJ. The centroids of each fPS were first localized and the localization accuracy is estimated to be around 1.5 nm [192]. Microscope stage drift was corrected by computing the translocation of stationary fPSs and translate each image with this distance. The centroids of a fPS in consecutive frames were linked and clustered into one trajectory, which were then used to compute the MSD. The MSD from all individual trajectories were averaged to produce the ensemble averaged MSD, which was then fitted to the power law form $MSD = At^\alpha$. The particle velocity distribution was obtained from its displacement in every 20 s. Walking yields are computed by categorizing the trajectories based on the rules presented in Table 6.2.

6.3.3 Simulation of 2-D DNA Walking

The simulation for 2-D DNA walking is based on the same mechanism as discussed in Chapter 5. However, since multiple DNA walkers could be attached on the fPS and compete for available fuels on a 2-D surface, additional simulation mechanisms were developed to account for this effect. When a simulation is initiated, the walker is first subjected to generate the length for the current step on a 2-D grid (Figure 6.4) based on a pre-defined probability distribution. After the stepping length is determined, the walker generates stepping time τ for all the four directions. The stochastic stepping

time τ is generated by assuming the three reaction steps depicted in Figure 6.2a have similar rate, which follows a Gamma distribution (See Chapter 5 for details). The rate k for each direction depends on whether the next grid position has an intact or consumed fuel. If the next position has been visited by the walker before, the stepping time for this direction will be much slower due to a 100-folds slower rate k . The walker proceeds to the direction which has the smallest stepping time τ , thus biasing away from its own path and travels in a “self-avoiding” fashion.

Simulation for multi-legged walker was performed by grouping single legs together and keeping them close to a centroid (Figure 6.4 b). Each leg will step based on the previously described mechanism. However, a prescribed number of “lead” legs are randomly assigned to the group of legs which were allowed to step first based on their surrounding fuel density. After stepping of the lead legs, the centroid position was updated and the experienced rate value k for the remaining legs were adjusted to reflect both the fuel density and centroid position. A higher k value is assigned towards the direction of centroid. After the stepping of the follower legs, the centroid position will be updated again and reflected in the k value for the surrounding grid positions. The MSD of the multi-legged walker as shown in Figure 6.4 has a initial diffusive walking phase followed by a transition region to the $t * \log(t)$ scaling.

6.3.4 Regulation of 2-D DNA Walking

For the inhibition of DNA motor function, walker decorated fPS are first flown into the channel as in regular walking experiments. Before the addition of RNase H, a 30 μL aliquot of 100 μM inhibitor strands was added in the channel and incubated for 15 min. The inhibitor strands were then thoroughly washed by 200 μL 1 \times PBS buffer. Walking experiments were then performed and imaged with the same procedure as regular walking tests. For the activation of DNA motor function after inhibition, 30 μL of 100 μM activator strands were added to the channel after inhibitor strands were washed out by 1 \times PBS. The activator induced strand displacement reaction was

(a) Single-legged walker

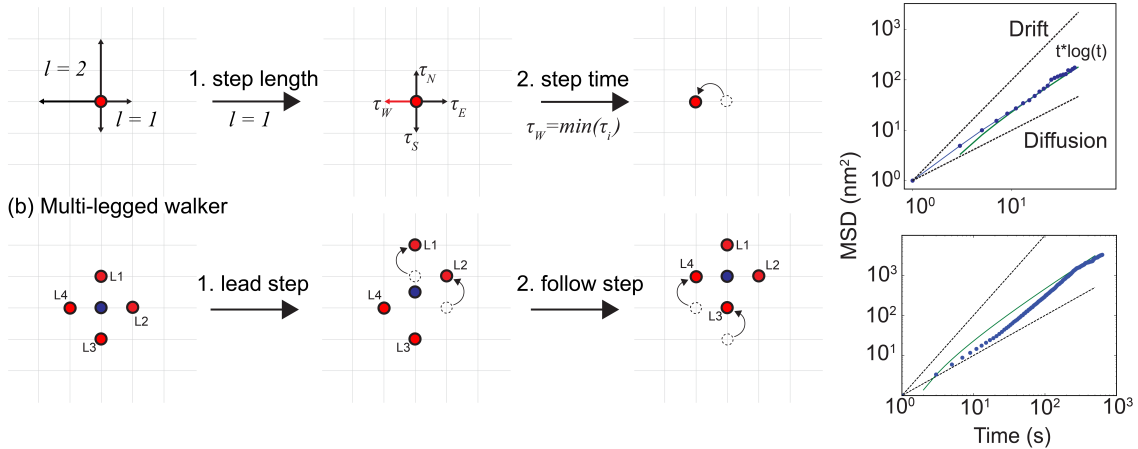


Figure 6.4. 2-D DNA walker simulation. **(a)** Simulation of a single-legged walker. The walker determines length l and time τ during a single step based on a user defined probability distribution. The direction of walker stepping is determined by the smallest stepping time τ . The MSD of such single legged walker shows super-diffusive feature and follows the scaling of $t * \log(t)$. **(b)** simulation of a 4-legged walker. The four legs are shown in red and the centroid of the walker is shown in blue. Two types of leg behaviors (lead or follow) are randomly assigned to the four legs. If two legs are assigned as lead legs (L1 and L2), they step based on the same scheme as described in **(a)** and centroid position is recomputed based on the current positions of the four legs. The two remaining legs (L3 and L4) will be assigned a biased rate towards the position of the centroid when stepping, thus will have the tendency to follow the centroid. The centroid position will be updated again after all the legs are moved. The MSD of 4-legged walker shows diffusive behaviors but ultimately converges to the scaling feature of $t * \log(t)$.

allowed to continue for 30 min before washing with 200 μ M 1 \times PBS. Regular walking measurement was then performed.

6.4 Results

6.4.1 Nuclease Powered 2-D DNA Walking

The DNA walker decorated fPS particles are conjugated onto 2-D surface through complementary binding with RNA fuels immobilized onto the surface. The DNA walker has a length of 13-nt that are complementary to RNA fuels. The surface bound fPS particles are stable and do not show significant movement in the absence of nuclease is present. Upon addition of RNase H into the channel, the DNA walkers on fPS particles are activated and starts traveling on the surface. Time-lapse imaging of the fPS particle movement and high-accuracy localization of the particle centroid reveal its trajectory with a temporal resolution of 200 ms (Figure 6.5 a). The walking mechanism behind such movement is studied by obtaining MSD from the particle moving trajectory. As described in previous chapters, the MSD can be fitted to a power law form At^α with its exponent α containing information about underlying walking mechanism. Briefly, for α smaller than 1, the motion is typically restricted in a confined space. If the α is close to 1, the motion is diffusive and its MSD scales linearly with time. For α larger than 1, the motion is super-diffusive and the MSD scales faster than random diffusion. When α is close to 2, the motion is typically driven by active force and has a constant velocity. In the case of DNA walker powered 2-D “self-avoiding” walking, the walker MSD is super-diffusion and should scale with $t * \log(t)$ (Figure 6.5b, green curve) [205]. The experimental data in Figure 6.5b shows a MSD that follows diffusive scaling at short time scales and only converges to $t * \log(t)$ scaling at longer time scales with scaling exponent $\alpha \sim 1.3$. The observed initial diffusive motion is a result of multi-valency in the walker system [204]. For a 200 nm particle, multiple DNA walker legs bind to the surface RNAs. The dissociation and association of each leg with consumed or intact fuels happen stochastically, thus

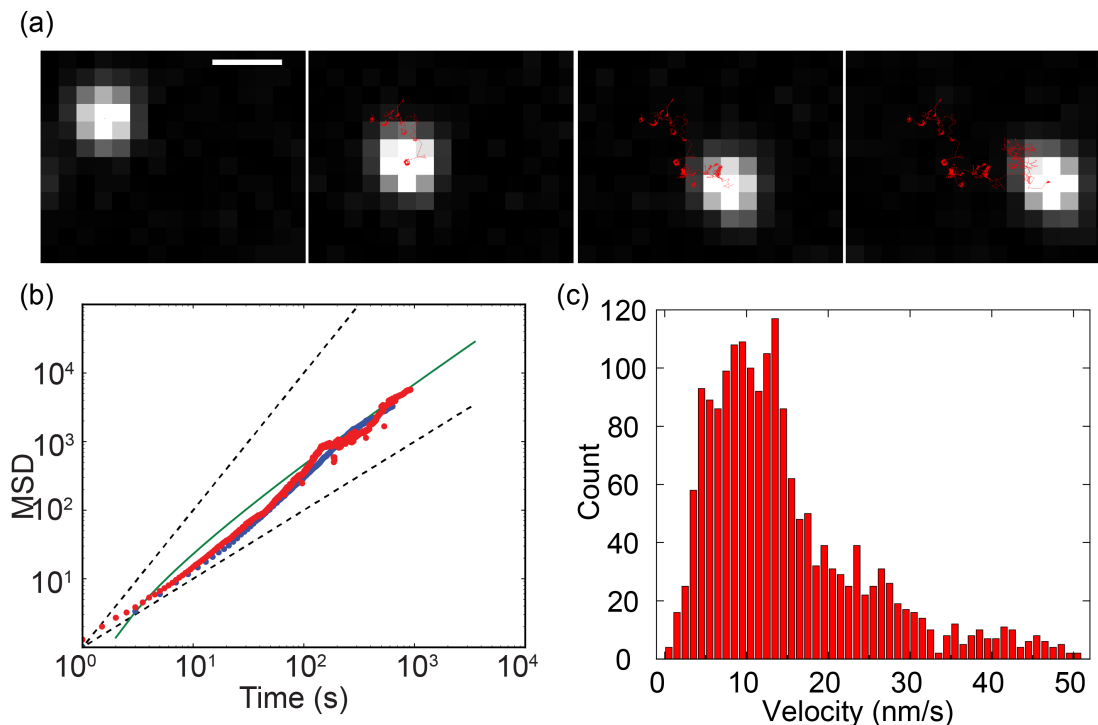


Figure 6.5. DNA powered walking in 2-D surface. **(a)** Time-lapse images of a fPS particle powered by DNA walkers. The trajectories of the walker are plotted in red. The total time for the movement is 20 min. The scale bar is 1 μm . **(b)** Ensemble averaged MSD of 2-D walkers. The MSD (red) follows the expected behavior of a multi-legged walker traveling in a “self-avoiding” fashion. MSD of simulated 2-D walkers are also plotted in blue for comparison. Dashed lines represent diffusive (bottom) or drift (top) motions. **(c)** Velocity distribution of the walker shown in **(a)**. The average velocity of the walker is approximately 15 nm s^{-1} .

creating random diffusion of the fPS at short time scale. This multi-valency effect reduces the effective fuel concentration locally for any single leg, thus reduces the effect of “self-avoiding” diffusion. However, at longer time scales, all the legs will ultimately diffuse away from its previous locations as all the fuels are consumed, thus giving rise to the expected $t * \log(t)$ scaling of MSD. To confirm this analysis, we performed a multi-valency simulation based on the proposed walking mechanism. The behavior of a 4-legged walker is simulated with similar kinetics. The simulation

clearly shows the observed diffusive motion at short time scale and the transition to the “self-avoiding” scaling.

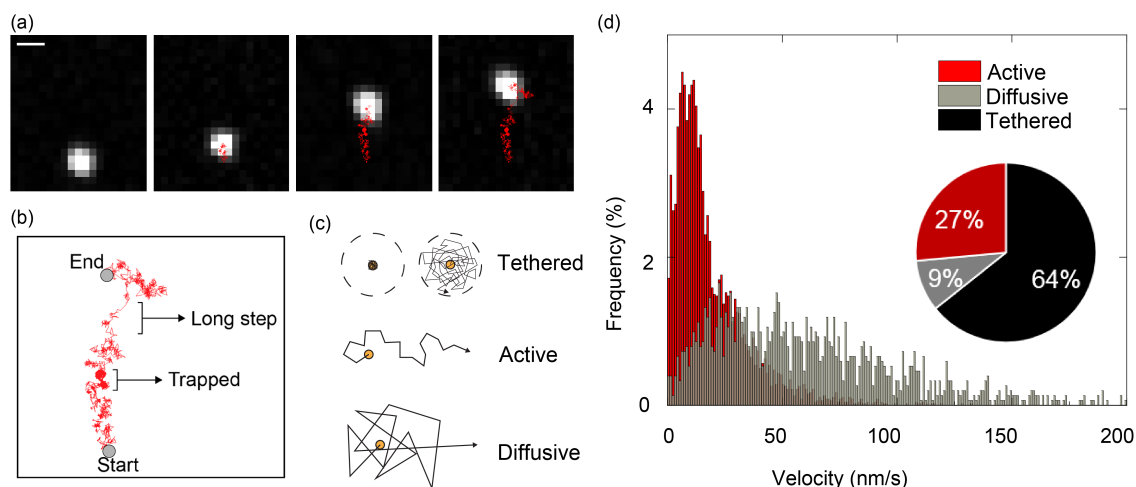


Figure 6.6. Characteristics of different walking modes. **(a)** Time-lapse images of a 200 nm moving FPS particle. **(b)** The trajectory of the walker shown in **(a)**. Regions showing distinctly different motility characteristics from typical walking are labeled. **(c)**. Scheme of different walking modes. Tethered walkers have typically less than 100 nm total displacement. Active walkers follow the expected “self-avoiding” behavior and travel processively over long distance. Diffusive walkers are less processive compared to active walkers, thus traveling randomly. **(d)** The velocity distribution and walking yield of active and diffusive walkers. Diffusive walkers have a much wider distribution as compared to the processive active walkers. The yield of a DNA walker with 13/0 configuration is shown in the pie chart.

The velocity of the walker is determined by computing the FPS centroid displacement in every 20 s. This time scale falls into the transition region of the walker to self-avoiding motion, thus allowing us to estimate the instantaneous velocity without being significantly biased by the tethered diffusive motion and experimental uncertainties at short time scale. Figure 6.5c shows the velocity distribution of a typical walker moving in “self-avoiding” fashion. The average velocity of the walker is $\sim 15 \text{ nm s}^{-1}$. However, the distribution of walker velocity has a large tail extending to 50 nm s^{-1} , which is more than three times faster than the average velocity. This heavy

tail in the velocity distribution is not a result of localization error as fPS has extremely stable fluorescence and can be localized to ≤ 10 nm accuracy. Thus, different walking mechanisms may have contributed to the fPS translocation which results in different walker motility. Figure 6.6a shows the time-lapse images and trajectory of a typical walker. The trajectory of the motion is analyzed in detail and different walking modes are identified from the trajectory (Figure 6.6). Three distinctive walking modes, tethered, active and diffusive walking, are observed. For tethered motion, the fPS spent significantly extended period of time attached to a small region (< 100 nm) along its trajectory. The MSD scaling exponent for the walker in this region drops well below 0.4 and the walker velocity is greatly reduced to ≤ 2 nm s⁻¹. This state of motion is a result of the walker being trapped in a region where no available fuels are present. The walker performs tethered diffusion until it reaches to the edge of such a region and finds intact fuel. In contrast to the slow motion in a trapped state, the walker also demonstrates long distance stepping, showing a significantly increased velocity. The MSD of the walker in this state shows diffusive scaling and the velocity of the walker are widely dispersed, ranging from several nanometer to hundreds of nanometers per second (Figure 6.6d). We postulate that this diffusive behavior is a result of the walker temporarily dissociates from the surface RNA and randomly re-attach to the surface again. To quantify the fractions of particles moving in each mode, we categorized the walkers in different walking modes based on its travel distance, velocity and MSD scaling exponent α (See Table 6.2). The percentage of active walkers are computed and used as the walking yield (Figure 6.6). Based on the velocity distribution and active walker fraction, we then explored different parameters' impact on walker motility, processivity and yields.

Control experiments were also performed to confirm that the walker is indeed driven by RNase H (Figure 6.7). The effects of Tween 20, RNA fuel and RNase H on the walking activity were tested. Tween 20 passivates the surface inhibition effect on RNase H. Without the Tween 20 layer on the RNA surface, the fPS particle adsorbed non-specifically and no walking was observed. The translocation of the

Table 6.2.
Criteria for categorizing different walking modes using MSD.

Mode	Criteria
Tethered	root MSD < 100 nm or $\alpha < 0.4$
Diffusive	root MSD > 100 nm and $0.4 < \alpha < 1.1$
Active	root MSD > 100 nm and $1.1 < \alpha < 2$

fPS also requires both RNA fuel and RNase H. When RNA portion in the fuel was replaced by DNA, no active walking was observed. Similarly, when RNase H was not added to the imaging channel, all fPS particles formed stable linkage onto the surface through base-pairing without significant movement over time.

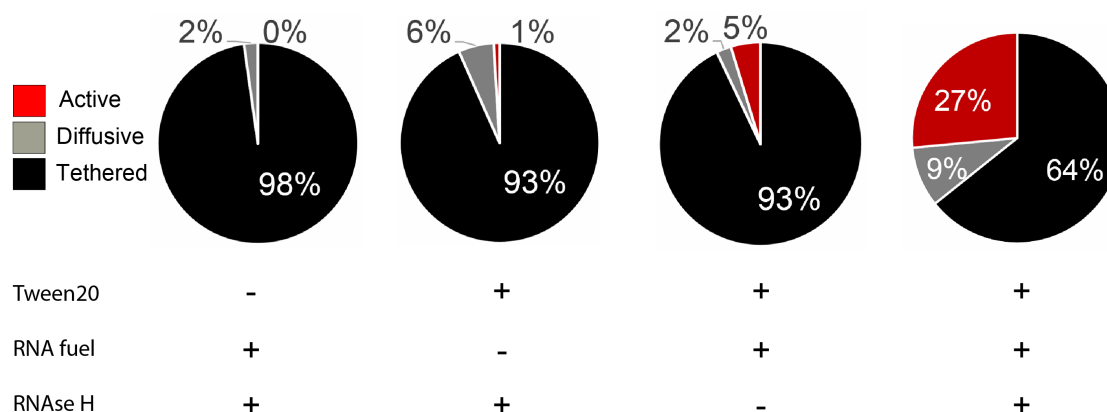


Figure 6.7. Negative control for enzymatic walking process. The Effects of Tween 20, RNA fuel and RNase H were examined. The plus and minus signs indicate whether certain molecules are present (+) or not (-). For the case of RNA fuel, the negative control was performed by replacing the RNA portion in the fuel to DNA with the same sequence.

6.4.2 Effect of Walker Valence

The first parameter we tested is the valence of walkers decorated on the fPS. The walking of 20 nm and 200 nm diameter particles are compared in Figure 6.8. To estimate the valence of the 200 nm fPS, we quantified the concentration ratio of DNA strands and fPS particle in stock solution. Based on a ratio of 2000 to DNA strands per fPS, we obtained the particle surface walker density of ~ 1 walker per 10×10 nm². Since surface fuels have a lower density compared to walker, the density of fuel and the walker trajectory path eventually determines the valence of a particular walker. Analysis of typical walker path reveals a path width of approximately 200 nm. With the surface RNA fuel density, we can calculate the valence of the particles to be close to 30. Based on the same calculation method, a 20 nm fPS particle has a valence of only one or two. Figure 6.8a shows the velocity distribution of the two different walkers. 20 nm fPS has a much higher number of moving steps (reflected in the total counts) and a wider distribution compared to 200 nm fPS due to less valence. This result is consistent with our expectation as the low valence should render 20 nm particles less processive during walking. On the other hand, the 20 nm particles' low valence allows RNase H to activate the walkers with less turnovers, thus increasing the total fraction of moving particles and achieving a higher yield (Figure 6.8b). Except for their difference in processivity and yields, both 20 nm and 200 nm particles travel in “self-avoiding” motion with similar motility.

6.4.3 Effect of Walker Strand Length

Besides the valence effect, we also explored the effect of DNA walker strand length. The walker results presented so far are based on strand with 13/0-nt configuration, which has 13-nt upper arm that binds to the RNA fuel but no lower arm for binding to the DNA. To examine processivity improvements, we designed sequence with a longer lower arm of 7-nt (13/7). A longer lower arm will serve as a “cleat” that prevents complete dissociation of the walker from surface fuels, thus increasing its

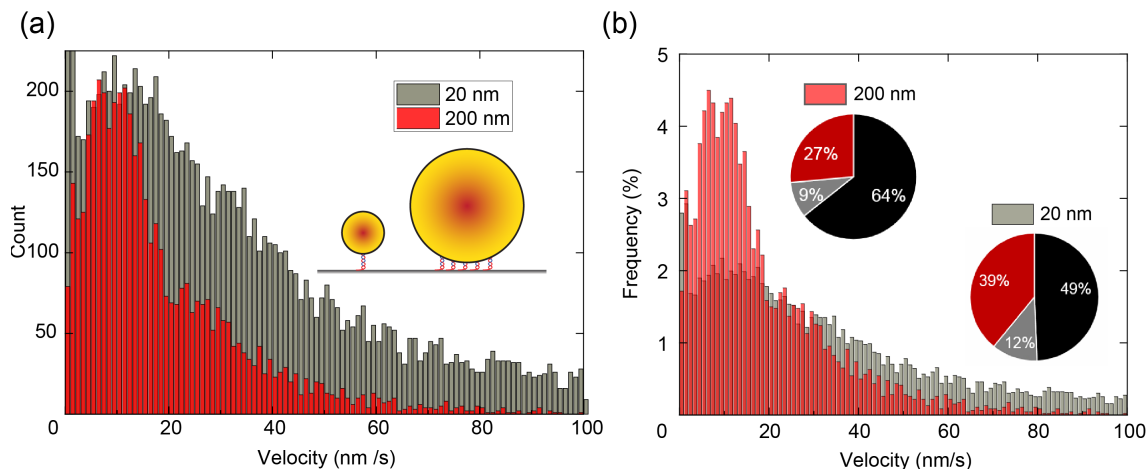


Figure 6.8. Valence effect on DNA walking. **(a)** The velocity distribution (counts) of walkers with different valences. For low valence 20 nm walkers there is a much wider distribution as compared to 200 nm walkers. The velocity at the peak of the distribution is similar to that of the 200 nm walkers at $\sim 15 \text{ nm s}^{-1}$. **(b)** The same distribution plotted in frequency and corresponding walker yields (pie chart). Low-valence 20 nm particles show a smaller portion of tethered walking, although they are less processive compared to high-valence 200-nm particle.

processivity. However, the inclusion of such lower arm could impact walker velocity as additional double strands need to be opened before particle migration. To test improvements on walker velocity, walker with a shorter upper arm (8/0-nt) is used. Figure 6.9a shows the velocity distribution of 13/7-nt walker as compared to 13/0-nt walker. As expected, the processivity of the walker is indeed improved as shown in the absence of the heavy tail in the distribution. The impact of the additional lower arm strand decreased the average walker velocity from $\sim 15 \text{ nm s}^{-1}$ to $\sim 10 \text{ nm s}^{-1}$. The yield of the walker is not significantly affected by the inclusion of the lower arm. Figure 6.9b shows the result of the 8/0-nt configured walkers. No significant impact on velocity and processivity is observed in these two cases. Due to the shorter length of complementary arm, higher portion of fPS indeed gets activated by the RNase H, which results in a higher walking yield. Based on the result of the 13/7-nt and 8/0-nt

armed walkers, we conclude that the inclusion of a lower arm and a shorter upper arm could potentially achieve high yield, high processivity 2-D walking.

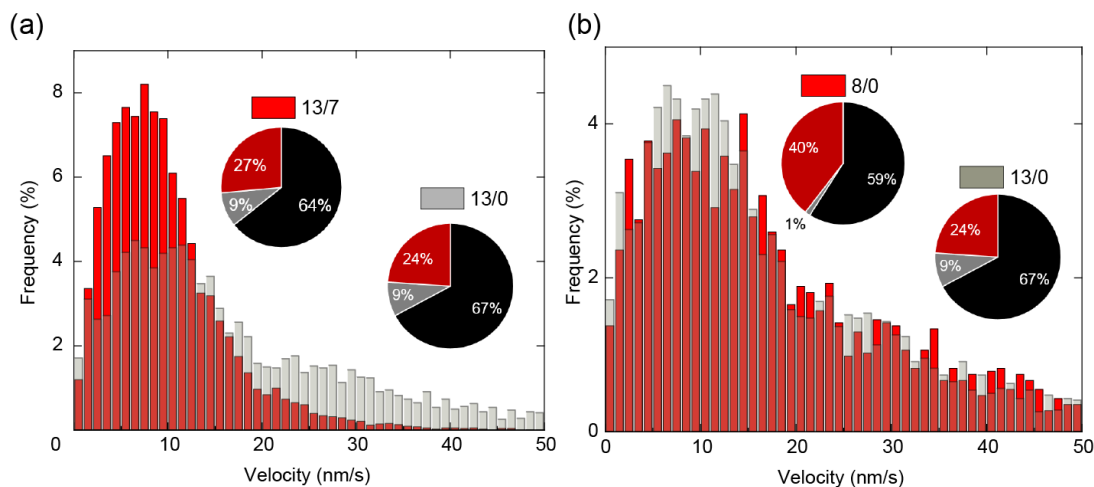


Figure 6.9. Walker length effect on 200 nm fPS. **(a)** Velocity distribution comparison of 13/7 and 13/0 configurations. Longer lower arm will ensure the walker travel more processively, thus having a narrower traveling velocity distribution. Both configurations have similar average velocity and yields. **(b)** Velocity distribution comparison of 8/0 and 13/0 configurations. Shorter upper arm increased the walking yield, but maintains a similar average velocity and processivity.

The length effects are less prominent in low-valence 20-nm fPS particles as shown in Figure 6.10. The velocity distributions of both 13/0 and 13/7 walkers show a heavy tail towards large displacement and a velocity peak at $\sim 15 \text{ nm s}^{-1}$. The 7-nt lower arm has little effect on stabilizing the 20-nm particles on the surface for processive walking, which indicates factors other than walker strand length, such as fuel density and valence, play a more important role in determining walker processivity. We further extracted an even longer lower arm with 15/15 configuration. Similar results in walker velocity distribution is observed in terms of processivity and average motility. However, this type of strand configuration significantly decreased the walking yield as the 15-nt binding onto surface DNA anchor is stable enough to slow down the migration after RNase H cleavage. Based on this observation, we can conclude that

the lower arm dissociation from the cleaved fuel does not affect the walker motility, but impacts the overall yield of walking. In fact, we discover that the fuel density on the surface, instead of the walker length, ultimately limits the walker motility and processivity. More detailed discussion will be provided in the Discussion section.

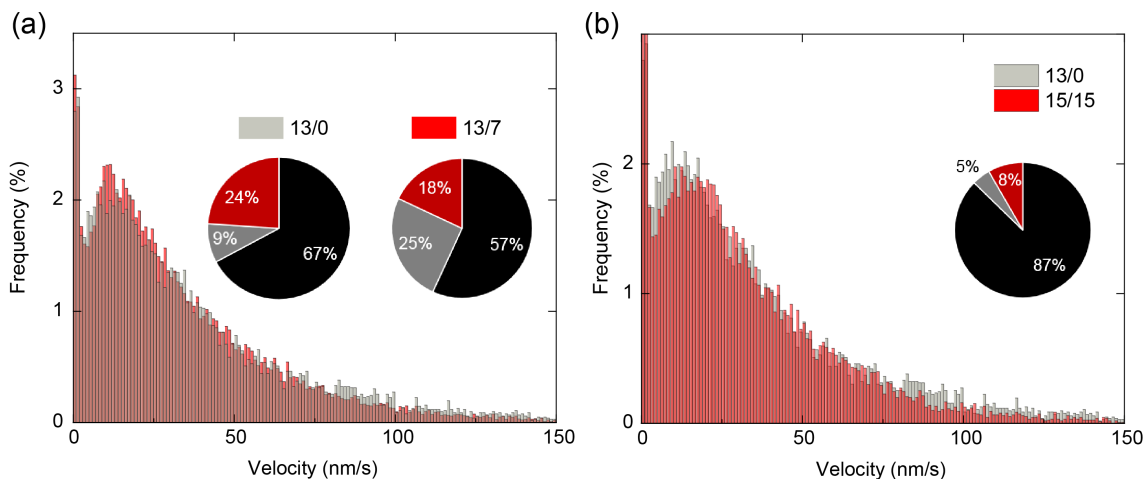


Figure 6.10. Walker length effect on 20 nm fPS. **(a)** Velocity distribution and yields of 13/7 and 13/0 configured walkers. Both walkers have similar motility and processivity, although the 13/7 walker appears to have a higher yield. **(b)** Velocity distribution and yields of 13/0 and 15/15 configured walkers. The 15/15 walker has a significantly lower yield compared to that of 13/0 walker, but the average velocity and distribution remain similar.

6.4.4 Inhibition and Activation of Walking

The on/off switch of walker motility is achieved using hairpin structured fuel and signaling oligonucleotides. As shown in Figure 6.11a, part of the fuel strand is used for the regulation (green) of motor functions (blue). A short oligonucleotide regulation strand functioning as a “glue” connects the upper and lower regulation strand, thus shielding RNA fuel which is initially exposed for walker consumption (Figure 6.11b first step). The short oligonucleotide strand turns off the walker strands’ motor function, thus is termed “inhibitor”. A 5-nt toehold on the inhibitor strand allows

strand displacement by an “activator” strand which fully complements the inhibitor strand. The removal of “inhibitor” strand thus recovers the motor function of the walker strand (Figure 6.11b second step). Figure 6.11c shows the walking yields of the system under different regulation states. When inhibitor signals are introduced, the DNA driven self-avoiding motion is significantly reduced from $\sim 30\%$ to only 1%. On the contrary, when the activators are added to remove inhibitor strands, the walking fraction recovers back to its typical value.

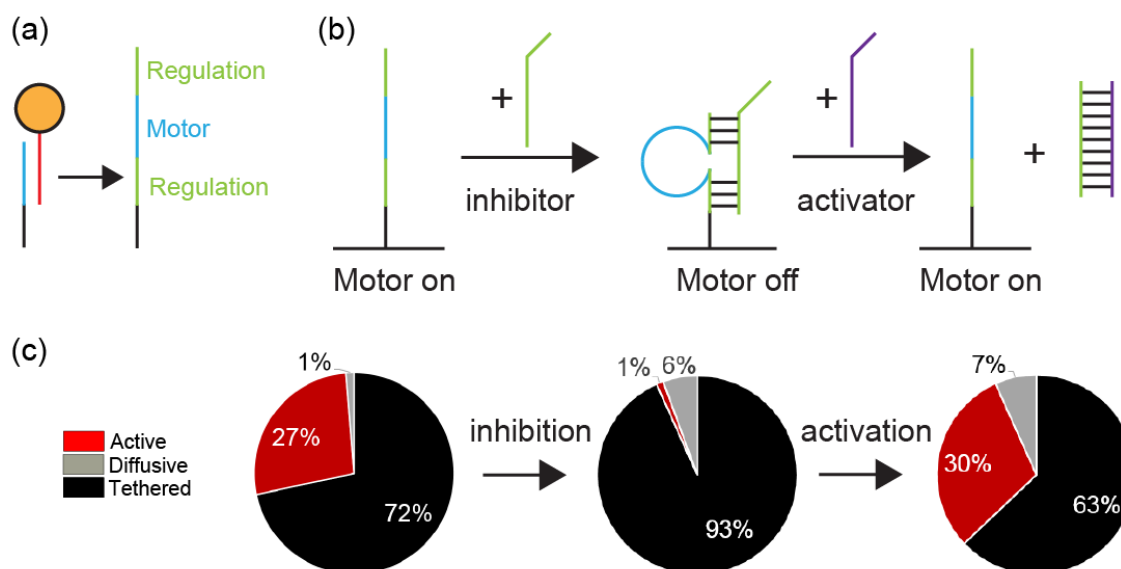


Figure 6.11. Scheme for motor function regulation. **(a)** Scheme showing the additional regulation region on the fuel strand. Green represents regulation region, blue represents motor function part and black represents anchor region. **(b)** Scheme showing the regulation of motor function using hairpin structured fuel and oligonucleotide signals. First step: the RNA fuel is sequestered in the hairpin conformation induced by the inhibitor strand, which turns off motor function; Second step: the addition of activator strand leads to the complete displacement of the inhibitor from the fuel strand, thus recovering the DNA walkers’ motor function. **(c)** Summary of walking yields when motor functions are inhibited and activated.

6.5 Discussion

6.5.1 Energy Efficiency of DNA based Transport

Motor proteins are highly efficient molecular machines that convert chemical energy into mechanical output [206]. To determine how efficient synthetic motors could utilize chemical energy, we computed the power efficiency of the DNA walker based transport system. The power efficiency of a walker can be defined as [207]:

$$\eta = \frac{\text{Mechanical Power Output}}{\text{Chemical Power Input}} = \frac{P_{mech}}{P_{chem}} \quad (6.1)$$

For fPS particle driven by DNA walkers, only the drag force by its surrounding viscous medium is applied. Thus, the mechanical power output can be calculated by [9]:

$$P_{mech} = F_{drag}v = C_d v^2 \quad (6.2)$$

Here v is the velocity of the particle, F_{drag} is the drag force and C_d is the drag coefficient. For a spherical particle, the Stokes-Einstein equation gives:

$$D = \frac{k_B T}{C_d} \quad (6.3)$$

where D is the diffusion coefficient, k_B is the Boltzmann constant, and T is the temperature. The diffusion coefficient D can be experimentally determined from diffusing particles on the imaging surface without RNase H. For 2-D Brownian motion, $MSD = 4Dt$. We measured the D value experimentally ($D \sim 5000 \text{ nm}^2\text{s}^{-1}$) and computed the mechanical power on a single to be $P_{mech} \sim 8 \times 10^{-23} \text{ W}$.

The chemical power input into the system is determined by multiple parameters, including the walker velocity v , trajectory width d , surface fuel density ρ , the number of cleavage site N on RNA fuel and the free energy released by a single phosphodiester bond ϵ :

$$P_{chem} = \frac{vd\rho N\epsilon}{N_{av}} \quad (6.4)$$

here N_{av} is the Avogadro's number. Using experimentally determined value of $v = 10 \text{ nm s}^{-1}$, $d = 200 \text{ nm}$, $\rho = \frac{1}{40^2} \text{ nm}^{-2}$, $\epsilon = 5.3 \text{ kcal kmol}^{-1}$ [208] and assuming $N =$

5, the value of chemical power input could be estimated as $P_{chem} \sim 2.1 \times 10^{-19}$ W. The walker efficiency can thus be determined to be approximately 3.8×10^{-4} . This efficiency value falls into the same range as other synthetic nanomotors [207], but is much lower when compared to estimated values (60%) for protein motors [209].

6.5.2 Rate-limiting Step in Walker Translocation

We explored multiple parameters that could affect walker motility, processivity and yields. This allows us to extract the rate-limiting reaction steps for the current system. For the walking mechanism depicted in Figure 6.2, three reaction steps (cleavage, association and dissociation) are proposed. However, walker valence should also be considered for the accurate prediction of reaction rates. The rate of RNase H enabled cleavage of RNA fuels and the subsequent dissociation of fragmented RNAs (k_1) depends on the RNase concentration, reaction conditions such as pH, and the minimum number of fuels to be hydrolyzed for movement. We experimentally determined the cleavage rate of RNase H in our experimental condition to be 0.6 s^{-1} , which is an order of magnitude faster than the reaction constant of strand migration and dissociation obtained from previous chapters (See Chapter 4 for detail). The rate of particle association with the next available fuel (k_2) depends on both the association rate ($10^6 \sim 10^7 \text{ M}^{-1} \text{ s}^{-1}$), minimum number of newly associated legs for the particle to move and the fuel density. The rate of the dissociation or branch migration (k_3) depends on the dissociation strand length and the minimum number of legs to be dissociated for the walker to move. The relative ratio of the corresponding reaction rates determines what modes are dominant during fPS particle translocation. For example, when the cleavage and dissociation rate is larger than the association rate, more long distance diffusive walking and a large velocity distribution will be observed.

To identify the rate-limiting reaction steps, we analyzed the effect of different parameters on the walker motility. To test if the enzymatic cleavage and the dissociation of the upper arm is the rate-limiting step, we performed experiments with

higher RNase H concentration and used faster exonuclease (EXO III) [210]. However, even with a 10-fold higher RNase H concentration and 100-fold faster cleavage rate of EXO III, no significant increase in velocity is observed. Moreover, a shorter upper arm in 8/0 configured walker also has no improvement on walker motility. Thus the enzymatic cleavage is unlikely to be the rate-limiting step. On the other hand, inclusion of a longer lower arm also does not slow down the walker as shown in the 13/0 *vs.* 13/7 case in Figure 6.9. These observations suggest that the association of the walker strand with the next available fuels is the rate limiting step. This conclusion indicates that the high reaction constant of complementary nucleotide strands association is affected by the low density of available fuels on the surface.

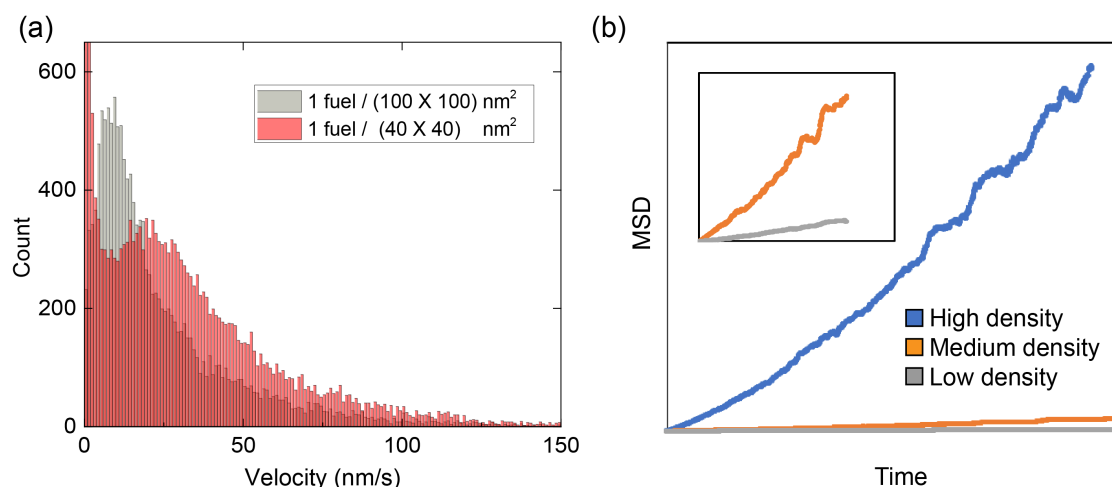


Figure 6.12. Increased walker motility in high density fuel surface. **(a)** Velocity distribution of 13/0 configured walkers traveling on two surfaces with different fuel density. Walkers moving on a high density surface shows an average velocity of around 25 nm s^{-1} as compared to 15 nm s^{-1} of walkers on low fuel density surface. **(b)** Simulation results of walkers moving on a high density and low density surface. The scaling of walker MSD shows significant difference for walkers in different density conditions. The inset in **(b)** shows an enlarged image of the same medium and low density walker MSD.

Upon further analysis of the surface fuel density, we noticed that the passivation agent Tween 20 could significantly affect the final fuel density. Tween 20 is used to prevent non-specific adsorption of fPS particles onto the surface and inhibition of RNase H. RNA fuels were grafted onto such surface through biotin-streptavidin interaction and could achieve a maximum density of roughly 1 fuel strand per $40 \times 40 \text{ nm}^2$ (Figure 6.3). However, excessive Tween 20 incubation on RNA decorated surface could degrade the surface density to as low as ~ 1 fuel per $200 \times 200 \text{ nm}^2$, thus lowering the reaction rate of walker association. To achieve a balance between good degree of surface passivation and fuel density, we minimized the content of Tween 20 on the surface so that the maximum number of fuel density could be achieved. DNA walkers (13/0) traveling on this surface has a significantly increased “self-avoiding” motion speed at $\sim 25 \text{ nm s}^{-1}$ (Figure 6.12). The effect of fuel density could also be simulated in our simulation platform. As shown in Figure 6.12b, the MSD of a multi-legged walker on high density fuel surface has a much faster scaling constant as compared to walkers on medium and low fuel density surfaces (Figure 6.12b inset). These results confirm that the association with the next available strand is indeed the rate-limiting step in our setup.

6.6 Conclusions

In this work, we developed a DNA walker powered 2-D transport scheme that shows super-diffusive behavior. Enzymatic cleavage of RNA fuels by RNase H is used to power the movement. The DNA powered transport follows “self-avoiding” motion. We explored design parameters such as valence and walker strand length, and evaluated the walker based on its motility, processivity and walking yields. Different walking modes are discussed based on the underlying mechanisms. By comparing the effects of different design parameters, we identified the rate-limiting reaction step in the proposed walking scheme.

The ability to program microscopic motion systems for desired functions is essential for various applications. This work provides a DNA based solution and offers useful insights on the design principles. More importantly, the ability to control different working modes serve as the basis for programming more complex functions and behaviors. For example, the activation of walker behavior upon the binding of signal molecules could potentially enable complex behaviors such as chemotaxis that are only observed in living systems. We will continue to improve this 2-D transport system to provide a robust system with excellent programmability.

7. CONCLUSIONS AND FUTURE WORKS

7.1 Conclusions

In this thesis, oligonucleotides and optical nanomaterials are used as building materials for synthetic nanosystems. The rich chemistry of DNA allows diverse interface chemistry between nucleotides and nanomaterials. The π interactions between DNA nitrogenous bases and SWCNT sidewall are used to solubilize and functionalize carbon nanotubes. The phosphorothioation of DNA backbone is used to terminate particle growth and immobilize strands on nanocrystal surface. The programmability of DNA strands offer broad engineering space for creating functional nanosystems with novel properties. The molecular recognition capability of DNA aptamers and substrate hydrolysis property of DNazymes are exploited for constructing optical molecular probes and DNA walkers.

For DNA aptamer enabled molecular recognition, aptamer stands are used to control the interaction of SWCNT surface with porphyrins. The interaction between aptamer-SWCNT complex and different porphyrin species enable direct modulation of SWCNT optical signals. Based on the optical responses, two interaction mechanisms between porphyrins and DNA aptamer functionalized SWCNT are identified. A multiplexed optical detection scheme is developed for the quantification of four biologically important porphyrin species [13].

For molecular walker systems, a DNzyme functionalized nanoparticle is demonstrated to actively move along a RNA decorated nanotube track powered by the hydrolysis of RNA fuels and DNA strand displacement [35]. The integration of optical nanomaterials with the walker system enables real-time optical tracking of walker translocation. Localization based sub-diffraction imaging scheme on the walker system reveals the number of rate-limiting intermediate reactions during a single DNzyme

turnover [182]. A detailed kinetic model that illustrates the impact of different design parameters on walker motility is proposed. Design principles based on walker kinetics are extracted for the rational design of DNAzyme powered walkers with desired properties. A DNAzyme walker traveling with a speed of $\sim 1 \text{ nm s}^{-1}$ and over $\sim 5 \text{ }\mu\text{m}$ is demonstrated to show the effectiveness of the design principles [182].

To achieve more versatile molecular transport, a multivalent DNA walker assembly is introduced using nuclease as power source. Multiple walker legs working collectively could transport a nanoparticle super-diffusively in 2-D, following “self-avoiding” scaling feature. The velocity distribution and MSD scaling reveals three 2-D motion components, tethered, diffusive and self-avoiding. The transition between these motion types can be tuned by sequence design and valence.

Besides the motor functions, various regulation mechanisms are explored to control DNA walker activities. Incorporation of photoisomerizable molecules such as azobenzene into the walker strand could effectively perturb base-pairing and cleavage rates. Using such molecules, UV/visible light illumination can be used as a remote signal to activate/inhibit walker activity. Chemical signals such as short oligonucleotides or small molecules can also serve as activator/inhibitor for DNA walker activity. Deactivation of fuel strand by forming hairpin through an inhibitor strand prevents nuclease or DNAzyme from providing power for walking.

7.2 Future Works

Current researches in the DNA walker community are largely focused on how nucleotides’ programmability could be exploited for walking mechanisms. The studies presented in this thesis provide novel tools and engineering methods to study walker systems integrated with nanomaterials. With such capabilities, several challenges can be addressed in future studies. At single molecule level, more efficient DNA walking mechanism with higher motility needs to be developed. Typical protein motors could achieve a power efficiency of 60%, compared to the $<0.1\%$ power efficiency of

synthetic motor systems [207]. A more efficient walking scheme could harvest more energy from both designed reactions and thermal fluctuation in the surrounding, thus potentially improving both walker efficiency and motility. Moreover, mechanisms that are different from “Burnt-bridge” or “Self-avoiding” are desirable for more versatile applications.

At system level, methods to coordinate the collective behaviors of large number of DNA walkers need to be developed. Natural molecular motors are built on similar biochemical mechanisms, but evolve into various families and self-assemble into distinct structures to accomplish specific tasks [211]. The mechanisms and understandings elucidated in this work could be used as a tool box for powering and controlling DNA based synthetic systems. The ability to integrate multiple motors and regulation mechanisms could enable coordination between walkers. With such engineering insights, complex motion patterns and behaviors only observed in living systems, such as chemotaxis and swarming, can be encoded into synthetic nanosystems using DNA.

REFERENCES

REFERENCES

- [1] Q. H. Wang, K. Kalantar-Zadeh, A. Kis, J. N. Coleman, and M. S. Strano, "Electronics and optoelectronics of two-dimensional transition metal dichalcogenides," *Nature Nanotechnology*, vol. 7, no. 11, pp. 699–712, 2012.
- [2] K. Welsher, Z. Liu, S. P. Sherlock, J. T. Robinson, Z. Chen, D. Daranciang, and H. Dai, "A route to brightly fluorescent carbon nanotubes for near-infrared imaging in mice," *Nature Nanotechnology*, vol. 4, no. 11, pp. 773–780, 2009.
- [3] Y. Shirasaki, G. J. Supran, M. G. Bawendi, and V. Bulović, "Emergence of colloidal quantum-dot light-emitting technologies," *Nature Photonics*, vol. 7, no. 1, pp. 13–23, 2013.
- [4] I. L. Medintz, H. T. Uyeda, E. R. Goldman, and H. Mattoussi, "Quantum dot bioconjugates for imaging, labelling and sensing," *Nature Materials*, vol. 4, no. 6, pp. 435–446, 2005.
- [5] J. H. Choi, K. H. Chen, and M. S. Strano, "Aptamer-capped nanocrystal quantum dots: a new method for label-free protein detection," *Journal of the American Chemical Society*, vol. 128, no. 49, pp. 15 584–15 585, 2006.
- [6] F. Zhang, J. Nangreave, Y. Liu, and H. Yan, "Structural DNA nanotechnology: state of the art and future perspective," *Journal of the American Chemical Society*, vol. 136, no. 32, pp. 11 198–11 211, 2014.
- [7] F. A. Aldaye, A. L. Palmer, and H. F. Sleiman, "Assembling materials with DNA as the guide," *Science*, vol. 321, no. 5897, pp. 1795–1799, 2008.
- [8] D. Y. Zhang and G. Seelig, "Dynamic DNA nanotechnology using strand-displacement reactions," *Nature Chemistry*, vol. 3, no. 2, pp. 103–113, 2011.
- [9] D. Boal, *Mechanics of the Cell*. Cambridge University Press, 2001.
- [10] B. Yurke, A. J. Turberfield, A. P. Mills, F. C. Simmel, and J. L. Neumann, "A DNA-fuelled molecular machine made of DNA," *Nature*, vol. 406, no. 6796, pp. 605–608, 2000.
- [11] Y. Chen, M. Wang, and C. Mao, "An autonomous DNA nanomotor powered by a DNA enzyme," *Angewandte Chemie International Edition*, vol. 43, no. 27, pp. 3554–3557, 2004.
- [12] F. C. Simmel and B. Yurke, "A DNA-based molecular device switchable between three distinct mechanical states," *Applied Physics Letters*, vol. 80, no. 5, pp. 883–885, 2002.
- [13] J. Pan, H. Zhang, T.-G. Cha, H. Chen, and J. Choi, "Multiplexed optical detection of plasma porphyrins using DNA aptamer-functionalized carbon nanotubes," *Analytical Chemistry*, vol. 85, no. 17, pp. 8391–8396, 2013.

- [14] T.-G. Cha, B. A. Baker, M. D. Sauffer, J. Salgado, D. Jaroch, J. L. Rickus, D. M. Porterfield, and J. H. Choi, "Optical nanosensor architecture for cell-signaling molecules using DNA aptamer-coated carbon nanotubes," *ACS Nano*, vol. 5, no. 5, pp. 4236–4244, 2011.
- [15] X. Chen and A. D. Ellington, "Shaping up nucleic acid computation," *Current Opinion Biotechnology*, vol. 21, no. 4, pp. 392–400, 2010.
- [16] Y. Benenson, "Biomolecular computing systems: principles, progress and potential," *Nature Review Genetics*, vol. 13, no. 7, pp. 455–468, 2012.
- [17] P. Yin, H. Yan, X. G. Daniell, A. J. Turberfield, and J. H. Reif, "A unidirectional DNA walker that moves autonomously along a track," *Angewandte Chemie International Edition*, vol. 43, no. 37, pp. 4906–4911, 2004.
- [18] J. S. Shin and N. A. Pierce, "A synthetic DNA walker for molecular transport," *Journal of the American Chemical Society*, vol. 126, no. 35, pp. 10 834–10 835, 2004.
- [19] W. B. Sherman and N. C. Seeman, "A precisely controlled DNA biped walking device," *Nano Letters*, vol. 4, no. 7, pp. 1203–1207, 2004.
- [20] J. Bath, S. J. Green, and A. J. Turberfield, "A free-running DNA motor powered by a nicking enzyme," *Angewandte Chemie International Edition*, vol. 44, no. 28, pp. 4358–4361, 2005.
- [21] Y. Tian, Y. He, Y. Chen, P. Yin, and C. Mao, "A DNzyme that walks processively and autonomously along a one-dimensional track," *Angewandte Chemie International Edition*, vol. 44, no. 28, pp. 4355–4358, 2005.
- [22] P. Yin, A. J. Turberfield, and J. H. Reif, "Designs of autonomous unidirectional walking DNA devices," in *DNA Computing.DNA2004.Lecture Notes in Computer Science*, C. Ferretti, G. Mauri, and C. Zandron, Eds. Berlin, Heidelberg: Springer, 2005, vol. 3384, pp. 410–425.
- [23] P. Yin, A. J. Turberfield, S. Sahu, and J. H. Reif, "Design of an autonomous DNA nanomechanical device capable of universal computation and universal translational motion," in *DNA Computing.DNA2004.Lecture Notes in Computer Science*, C. Ferretti, G. Mauri, and C. Zandron, Eds. Berlin, Heidelberg: Springer, 2005, vol. 3384, pp. 426–444.
- [24] R. Pei, S. K. Taylor, D. Stefanovic, S. Rudchenko, T. E. Mitchell, and M. N. Stojanovic, "Behavior of polycatalytic assemblies in a substrate-displaying matrix," *Journal of the American Chemical Society*, vol. 128, no. 39, pp. 12 693–12 699, 2006.
- [25] S. Venkataraman, R. M. Dirks, P. W. K. Rothmund, E. Winfree, and N. A. Pierce, "An autonomous polymerization motor powered by DNA hybridization," *Nature Nanotechnology*, vol. 2, no. 8, pp. 490–494, 2007.
- [26] Z. Wang, "Synergic mechanism and fabrication target for bipedal nanomotors," *Proceedings of the National Academy of Sciences of the United States of America*, vol. 104, no. 46, pp. 17 921–17 926, 2007.

- [27] S. J. Green, J. Bath, and A. J. Turberfield, "Coordinated chemomechanical cycles: a mechanism for autonomous molecular motion," *Physical Review Letters*, vol. 101, no. 23, p. 238101, 2008.
- [28] P. Yin, H. M. Choi, C. R. Calvert, and N. A. Pierce, "Programming biomolecular self-assembly pathways," *Nature*, vol. 451, no. 7176, pp. 318–22, 2008.
- [29] A. J. Genot, D. Y. Zhang, J. Bath, and A. J. Turberfield, "Remote toehold: a mechanism for flexible control of DNA hybridization kinetics," *Journal of the American Chemical Society*, vol. 133, no. 7, pp. 2177–2182, 2011.
- [30] T. Omabegho, R. Sha, and N. C. Seeman, "A bipedal DNA Brownian motor with coordinated legs," *Science*, vol. 324, no. 5923, pp. 67–71, 2009.
- [31] H. Gu, J. Chao, S.-J. Xiao, and N. C. Seeman, "A proximity-based programmable DNA nanoscale assembly line," *Nature*, vol. 465, no. 7295, pp. 202–205, 2010.
- [32] J. Bath, S. J. Green, K. E. Allen, and A. J. Turberfield, "Mechanism for a directional, processive, and reversible DNA motor," *Small*, vol. 5, no. 13, pp. 1513–1516, 2009.
- [33] K. Lund, A. J. Manzo, N. Dabby, N. Michelotti, A. Johnson-Buck, J. Nangreave, S. Taylor, R. Pei, M. N. Stojanovic, N. G. Walter, E. Winfree, and H. Yan, "Molecular robots guided by prescriptive landscapes," *Nature*, vol. 465, no. 7295, pp. 206–210, 2010.
- [34] S. F. Wickham, J. Bath, Y. Katsuda, M. Endo, K. Hidaka, H. Sugiyama, and A. J. Turberfield, "A DNA-based molecular motor that can navigate a network of tracks," *Nature Nanotechnology*, vol. 7, no. 3, pp. 169–173, 2012.
- [35] T.-G. Cha, J. Pan, H. R. Chen, J. Salgado, X. Li, C. D. Mao, and J. H. Choi, "A synthetic DNA motor that transports nanoparticles along carbon nanotubes," *Nature Nanotechnology*, vol. 9, no. 1, pp. 39–43, 2014.
- [36] S. J. Green, D. Lubrich, and A. J. Turberfield, "DNA hairpins: fuel for autonomous DNA devices," *Biophysical Journal*, vol. 91, no. 8, pp. 2966–2975, 2006.
- [37] J. H. Reif and S. Sahu, "Autonomous programmable DNA nanorobotic devices using DNazymes," *Theoretical Computer Science*, vol. 410, no. 15, pp. 1428–1439, 2009.
- [38] M. You, Y. Chen, X. Zhang, H. Liu, R. Wang, K. Wang, K. R. Williams, and W. Tan, "An autonomous and controllable light-driven DNA walking device," *Angewandte Chemie International Edition*, vol. 124, no. 10, pp. 2507–2510, 2012.
- [39] R. A. Muscat, J. Bath, and A. J. Turberfield, "Small molecule signals that direct the route of a molecular cargo," *Small*, vol. 8, no. 23, pp. 3593–3597, 2012.
- [40] Z. G. Wang, J. Elbaz, and I. Willner, "DNA machines: Bipedal walker and stepper," *Nano Letters*, vol. 11, no. 1, pp. 304–309, 2010.

- [41] I. Y. Loh, J. Cheng, S. R. Tee, A. Efremov, and Z. Wang, "From bistate molecular switches to self-directed track-walking nanomotors," *ACS Nano*, vol. 8, no. 10, pp. 10 293–10 304, 2014.
- [42] D. Liu and S. Balasubramanian, "A proton fuelled DNA nanomachine," *Angewandte Chemie International Edition*, vol. 42, no. 46, pp. 5734–5736, 2003.
- [43] F. C. Simmel, "Processive motion of bipedal DNA walkers," *ChemPhysChem*, vol. 10, no. 15, pp. 2593–2597, 2009.
- [44] M. Liu, R. Hou, J. Cheng, I. Y. Loh, S. Sreelatha, J. N. Tey, J. Wei, and Z. Wang, "Autonomous synergic control of nanomotors," *ACS Nano*, vol. 8, no. 2, pp. 1792–1803, 2014.
- [45] S. F. Wickham, M. Endo, Y. Katsuda, K. Hidaka, J. Bath, H. Sugiyama, and A. J. Turberfield, "Direct observation of stepwise movement of a synthetic molecular transporter," *Nature Nanotechnology*, vol. 6, no. 3, pp. 166–169, 2011.
- [46] R. Masoud, R. Tsukanov, T. E. Tomov, N. Plavner, M. Liber, and E. Nir, "Studying the structural dynamics of bipedal DNA motors with single-molecule fluorescence spectroscopy," *ACS Nano*, vol. 6, no. 7, pp. 6272–6283, 2012.
- [47] A. Rajendran, M. Endo, K. Hidaka, and H. Sugiyama, "Direct and real-time observation of rotary movement of a DNA nanomechanical device," *Journal of the American Chemical Society*, vol. 135, no. 3, pp. 1117–1123, 2013.
- [48] N. Kodera, D. Yamamoto, R. Ishikawa, and T. Ando, "Video imaging of walking myosin v by high-speed atomic force microscopy," *Nature*, vol. 468, no. 7320, pp. 72–76, 2010.
- [49] T. E. Tomov, R. Tsukanov, M. Liber, R. Masoud, N. Plavner, and E. Nir, "Rational design of DNA motors: fuel optimization through single-molecule fluorescence," *Journal of the American Chemical Society*, vol. 135, no. 32, pp. 11 935–11 941, 2013.
- [50] M. Liber, T. E. Tomov, R. Tsukanov, Y. Berger, and E. Nir, "A bipedal DNA motor that travels back and forth between two DNA origami tiles," *Small*, vol. 11, no. 5, pp. 568–575, 2014.
- [51] R. Tsukanov, T. E. Tomov, M. Liber, Y. Berger, and E. Nir, "Developing DNA nanotechnology using single-molecule fluorescence," *Accounts of Chemical Research*, vol. 47, no. 6, pp. 1789–1798, 2014.
- [52] A. Yildiz, M. Tomishige, R. D. Vale, and P. R. Selvin, "Kinesin walks hand-over-hand," *Science*, vol. 303, no. 5658, pp. 676–678, 2004.
- [53] A. Yildiz, J. N. Forkey, S. A. McKinney, T. Ha, Y. E. Goldman, and P. R. Selvin, "Myosin v walks hand-over-hand: single fluorophore imaging with 1.5-nm localization," *Science*, vol. 300, no. 5628, pp. 2061–2065, 2003.

- [54] E. Toprak, C. Kural, and P. R. Selvin, "Super-accuracy and super-resolution: Getting around the diffraction limit," in *Single Molecule Tools, Part B: Super-Resolution, Particle Tracking, Multiparameter, and Force Based Methods*, ser. Methods in Enzymology, N. G. Walter, Ed. Academic Press, 2010, vol. 475, chapter 1, pp. 1–26.
- [55] M. Hoffman, J. Sheung, and P. Selvin, "Fluorescence imaging with one nanometer accuracy: In vitro and in vivo studies of molecular motors," in *Single Molecule Enzymology*, ser. Methods in Molecular Biology, G. I. Mashanov and C. Batters, Eds. Humana Press, 2011, vol. 778, chapter 4, pp. 33–56.
- [56] N. Michelotti, C. de Silva, A. E. Johnson-Buck, A. J. Manzo, and N. G. Walter, "A bird's eye view: Tracking slow nanometer-scale movements of single molecular nano-assemblies," in *Single Molecule Tools, Part B: Super-Resolution, Particle Tracking, Multiparameter, and Force Based Methods*, ser. Methods in Enzymology, N. G. Walter, Ed. Academic Press, 2010, vol. 475, chapter 6, pp. 121–148.
- [57] S. Bretschneider, C. Eggeling, and S. W. Hell, "Breaking the diffraction barrier in fluorescence microscopy by optical shelving," *Physical Review Letters*, vol. 98, no. 21, p. 218103, 2007.
- [58] H. Deschout, F. C. Zancchi, M. Mlodzianoski, A. Diaspro, J. Bewersdorf, S. T. Hess, and K. Braeckmans, "Precisely and accurately localizing single emitters in fluorescence microscopy," *Nature Methods*, vol. 11, no. 3, pp. 253–266, 2014.
- [59] A. Yildiz and P. R. Selvin, "Fluorescence imaging with one nanometer accuracy: application to molecular motors," *Accounts of Chemical Research*, vol. 38, no. 7, pp. 574–582, 2005.
- [60] B. Huang, "Super-resolution optical microscopy: multiple choices," *Current Opinion in Chemical Biology*, vol. 14, no. 1, pp. 10–14, 2010.
- [61] B. Huang, H. Babcock, and X. Zhuang, "Breaking the diffraction barrier: super-resolution imaging of cells," *Cell*, vol. 143, no. 7, pp. 1047–1058, 2010.
- [62] S. W. Hell, "Microscopy and its focal switch," *Nature Methods*, vol. 6, no. 1, pp. 24–32, 2009.
- [63] M. Bates, B. Huang, G. T. Dempsey, and X. W. Zhuang, "Multicolor super-resolution imaging with photo-switchable fluorescent probes," *Science*, vol. 317, no. 5845, pp. 1749–1753, 2007.
- [64] G. Donnert, J. Keller, C. A. Wurm, S. O. Rizzoli, V. Westphal, A. Schonle, R. Jahn, S. Jakobs, C. Eggeling, and S. W. Hell, "Two-color far-field fluorescence nanoscopy," *Biophysical Journal*, vol. 92, no. 8, pp. L67–L69, 2007.
- [65] H. Shroff, C. G. Galbraith, J. A. Galbraith, H. White, J. Gillette, S. Olenych, M. W. Davidson, and E. Betzig, "Dual-color superresolution imaging of genetically expressed probes within individual adhesion complexes," *Proceedings of the National Academy of Sciences of the United States of America*, vol. 104, no. 51, pp. 20 308–20 313, 2007.

- [66] B. Huang, S. A. Jones, B. Brandenburg, and X. W. Zhuang, "Whole-cell 3d storm reveals interactions between cellular structures with nanometer-scale resolution," *Nature Methods*, vol. 5, no. 12, pp. 1047–1052, 2008.
- [67] M. Bates, T. R. Blosser, and X. W. Zhuang, "Short-range spectroscopic ruler based on a single-molecule optical switch," *Physical Review Letters*, vol. 94, no. 10, p. 108101, 2005.
- [68] M. Bossi, J. Folling, V. N. Belov, V. P. Boyarskiy, R. Medda, A. Egner, C. Eggeling, A. Schonle, and S. W. Hell, "Multicolor far-field fluorescence nanoscopy through isolated detection of distinct molecular species," *Nano Letters*, vol. 8, no. 8, pp. 2463–2468, 2008.
- [69] M. Heilemann, S. van de Linde, M. Schuttpelz, R. Kasper, B. Seefeldt, A. Mukherjee, P. Tinnefeld, and M. Sauer, "Subdiffraction-resolution fluorescence imaging with conventional fluorescent probes," *Angewandte Chemie International Edition*, vol. 47, no. 33, pp. 6172–6176, 2008.
- [70] M. Andresen, A. C. Stiel, J. Folling, D. Wenzel, A. Schonle, A. Egner, C. Eggeling, S. W. Hell, and S. Jakobs, "Photoswitchable fluorescent proteins enable monochromatic multilabel imaging and dual color fluorescence nanoscopy," *Nature Biotechnology*, vol. 26, no. 9, pp. 1035–1040, 2008.
- [71] B. Huang, M. Bates, and X. W. Zhuang, "Super-resolution fluorescence microscopy," *Annual Review of Biochemistry*, vol. 78, pp. 993–1016, 2009.
- [72] A. Small and S. Stahlheber, "Fluorophore localization algorithms for super-resolution microscopy," *Nature Methods*, vol. 11, no. 3, pp. 267–279, 2014.
- [73] N. Chenouard, I. Smal, F. De Chaumont, M. Maška, I. F. Sbalzarini, Y. Gong, J. Cardinale, C. Carthel, S. Coraluppi, M. Winter *et al.*, "Objective comparison of particle tracking methods," *Nature Methods*, vol. 11, no. 3, pp. 281–289, 2014.
- [74] R. B. Weisman, "Fluorimetric characterization of single-walled carbon nanotubes," *Analytical and Bioanalytical Chemistry*, vol. 396, no. 3, pp. 1015–1023, 2010.
- [75] R. B. Weisman and S. M. Bachilo, "Dependence of optical transition energies on structure for single-walled carbon nanotubes in aqueous suspension: an empirical katura plot," *Nano Letters*, vol. 3, no. 9, pp. 1235–1238, 2003.
- [76] R. B. Weisman, S. M. Bachilo, and D. Tsyboulski, "Fluorescence spectroscopy of single-walled carbon nanotubes in aqueous suspension," *Applied Physics A*, vol. 78, no. 8, pp. 1111–1116, 2004.
- [77] A. A. Boghossian, J. Zhang, P. W. Barone, N. F. Reuel, J.-H. Kim, D. A. Heller, J.-H. Ahn, A. J. Hilmer, A. Rwei, J. R. Arkalgud *et al.*, "Near-infrared fluorescent sensors based on single-walled carbon nanotubes for life sciences applications," *ChemSusChem*, vol. 4, no. 7, pp. 848–863, 2011.
- [78] M. J. O'Connell, S. M. Bachilo, C. B. Huffman, V. C. Moore, M. S. Strano, E. H. Haroz, K. L. Rialon, P. J. Boul, W. H. Noon, C. Kittrell *et al.*, "Band gap fluorescence from individual single-walled carbon nanotubes," *Science*, vol. 297, no. 5581, pp. 593–596, 2002.

- [79] F. Wang, G. Dukovic, L. E. Brus, and T. F. Heinz, "The optical resonances in carbon nanotubes arise from excitons," *Science*, vol. 308, no. 5723, pp. 838–841, 2005.
- [80] S. M. Bachilo, M. S. Strano, C. Kittrell, R. H. Hauge, R. E. Smalley, and R. B. Weisman, "Structure-assigned optical spectra of single-walled carbon nanotubes," *Science*, vol. 298, no. 5602, pp. 2361–2366, 2002.
- [81] H. Kataura, Y. Kumazawa, Y. Maniwa, I. Umez, S. Suzuki, Y. Ohtsuka, and Y. Achiba, "Optical properties of single-wall carbon nanotubes," *Synthetic Metals*, vol. 103, no. 1, pp. 2555–2558, 1999.
- [82] J. Lefebvre, D. G. Austing, J. Bond, and P. Finnie, "Photoluminescence imaging of suspended single-walled carbon nanotubes," *Nano Letters*, vol. 6, no. 8, pp. 1603–1608, 2006.
- [83] J. Crochet, M. Clemens, and T. Hertel, "Quantum yield heterogeneities of aqueous single-wall carbon nanotube suspensions," *Journal of the American Chemical Society*, vol. 129, no. 26, pp. 8058–8059, 2007.
- [84] F. Wang, G. Dukovic, L. E. Brus, and T. F. Heinz, "Time-resolved fluorescence of carbon nanotubes and its implication for radiative lifetimes," *Physical Review Letters*, vol. 92, no. 17, p. 177401, 2004.
- [85] P. W. Barone, R. S. Parker, and M. S. Strano, "In vivo fluorescence detection of glucose using a single-walled carbon nanotube optical sensor: design, fluorophore properties, advantages, and disadvantages," *Analytical Chemistry*, vol. 77, no. 23, pp. 7556–7562, 2005.
- [86] D. A. Heller, S. Baik, T. E. Eurell, and M. S. Strano, "Single-walled carbon nanotube spectroscopy in live cells: towards long-term labels and optical sensors," *Advanced Materials*, vol. 17, no. 23, pp. 2793–2799, 2005.
- [87] P. Cherukuri, S. M. Bachilo, S. H. Litovsky, and R. B. Weisman, "Near-infrared fluorescence microscopy of single-walled carbon nanotubes in phagocytic cells," *Journal of the American Chemical Society*, vol. 126, no. 48, pp. 15 638–15 639, 2004.
- [88] L. J. Carlson and T. D. Krauss, "Photophysics of individual single-walled carbon nanotubes," *Accounts of Chemical Research*, vol. 41, no. 2, pp. 235–243, 2008.
- [89] A. Hartschuh, H. N. Pedrosa, L. Novotny, and T. D. Krauss, "Simultaneous fluorescence and raman scattering from single carbon nanotubes," *Science*, vol. 301, no. 5638, pp. 1354–1356, 2003.
- [90] S. Diao, G. Hong, A. L. Antaris, J. L. Blackburn, K. Cheng, Z. Cheng, and H. Dai, "Biological imaging without autofluorescence in the second near-infrared region," *Nano Research*, vol. 8, no. 9, pp. 3027–3034, Sep 2015.
- [91] G. Hong, A. L. Antaris, and H. Dai, "Near-infrared fluorophores for biomedical imaging," *Nature Biomedical Engineering*, vol. 1, p. 0010, 2017.
- [92] A. M. Smith, M. C. Mancini, and S. Nie, "Bioimaging: second window for in vivo imaging," *Nature nanotechnology*, vol. 4, no. 11, pp. 710–711, 2009.

- [93] J. H. Choi, F. T. Nguyen, P. W. Barone, D. A. Heller, A. E. Moll, D. Patel, S. A. Boppart, and M. S. Strano, "Multimodal biomedical imaging with asymmetric single-walled carbon nanotube/iron oxide nanoparticle complexes," *Nano Letters*, vol. 7, no. 4, pp. 861–867, 2007.
- [94] U. Resch-Genger, M. Grabolle, S. Cavaliere-Jaricot, R. Nitschke, and T. Nann, "Quantum dots versus organic dyes as fluorescent labels," *Nature Methods*, vol. 5, no. 9, pp. 763–775, 2008.
- [95] R. Rossetti, S. Nakahara, and L. Brus, "Quantum size effects in the redox potentials, resonance raman spectra, and electronic spectra of cds crystallites in aqueous solution," *The Journal of Chemical Physics*, vol. 79, no. 2, pp. 1086–1088, 1983.
- [96] I. Rasnik, S. A. McKinney, and T. Ha, "Nonblinking and long-lasting single-molecule fluorescence imaging," *Nature Methods*, vol. 3, no. 11, pp. 891–893, 2006.
- [97] J. J. Li, Y. A. Wang, W. Guo, J. C. Keay, T. D. Mishima, M. B. Johnson, and X. Peng, "Large-scale synthesis of nearly monodisperse CdSe/CdS core/shell nanocrystals using air-stable reagents via successive ion layer adsorption and reaction," *Journal of the American Chemical Society*, vol. 125, no. 41, pp. 12 567–12 575, 2003.
- [98] A. M. Smith, A. M. Mohs, and S. Nie, "Tuning the optical and electronic properties of colloidal nanocrystals by lattice strain," *Nature Nanotechnology*, vol. 4, no. 1, pp. 56–63, 2009.
- [99] P. Frantsuzov, M. Kuno, B. Janko, and R. A. Marcus, "Universal emission intermittency in quantum dots, nanorods and nanowires," *Nature Physics*, vol. 4, no. 7, pp. 519–522, 2008.
- [100] S. Kim, B. Fisher, H.-J. Eisler, and M. Bawendi, "Type-II quantum dots: CdTe/CdSe (core/shell) and CdSe/ZnTe (core/shell) heterostructures," *Journal of the American Chemical Society*, vol. 125, no. 38, pp. 11 466–11 467, 2003.
- [101] T. D. Krauss and J. J. Peterson, "Bright future for fluorescence blinking in semiconductor nanocrystals," *The Journal of Physical Chemistry Letters*, vol. 1, no. 9, pp. 1377–1382, 2010.
- [102] B. Mahler, P. Spinicelli, S. Buil, X. Quelin, J.-P. Hermier, and B. Dubertret, "Towards non-blinking colloidal quantum dots," *Nature Materials*, vol. 7, no. 8, pp. 659–664, 2008.
- [103] W. Gao and J. Wang, "Synthetic micro/nanomotors in drug delivery," *Nanoscale*, vol. 6, no. 18, pp. 10 486–10 494, 2014.
- [104] A. Chałupniak, E. Morales-Narváez, and A. Merkoçi, "Micro and nanomotors in diagnostics," *Advanced Drug Delivery Reviews*, vol. 95, pp. 104–116, 2015.
- [105] V. V. Singh and J. Wang, "Nano/micromotors for security/defense applications. a review," *Nanoscale*, vol. 7, no. 46, pp. 19 377–19 389, 2015.
- [106] F. Li, T.-G. Cha, J. Pan, A. Ozcelikkale, B. Han, and J. H. Choi, "DNA walker-regulated cancer cell growth inhibition," *ChemBioChem*, vol. 17, no. 12, pp. 1138–1141, 2016.

- [107] F. Dannenberg, M. Kwiatkowska, C. Thachuk, and A. J. Turberfield, "DNA walker circuits: computational potential, design, and verification," *Natural Computing*, vol. 14, no. 2, pp. 195–211, 2015.
- [108] V. C. Moore, M. S. Strano, E. H. Haroz, R. H. Hauge, R. E. Smalley, J. Schmidt, and Y. Talmon, "Individually suspended single-walled carbon nanotubes in various surfactants," *Nano Letters*, vol. 3, no. 10, pp. 1379–1382, 2003.
- [109] M. Zheng, A. Jagota, M. S. Strano, A. P. Santos, P. Barone, S. G. Chou, B. A. Diner, M. S. Dresselhaus, R. S. McLean, G. B. Onoa, G. G. Samsonidze, E. D. Semke, M. Usrey, and D. J. Walls, "Structure-based carbon nanotube sorting by sequence-dependent DNA assembly," *Science*, vol. 302, no. 5650, pp. 1545–1548, 2003.
- [110] Z. Deng, A. Samanta, J. Nangreave, H. Yan, and Y. Liu, "Robust DNA-functionalized core/shell quantum dots with fluorescent emission spanning from UV–VIS to near-IR and compatible with DNA-directed self-assembly," *Journal of the American Chemical Society*, vol. 134, no. 42, pp. 17 424–17 427, 2012.
- [111] N. Ma, E. H. Sargent, and S. O. Kelley, "One-step DNA-programmed growth of luminescent and biofunctionalized nanocrystals," *Nature Nanotechnology*, vol. 4, no. 2, pp. 121–125, 2009.
- [112] A. Samanta, Z. Deng, and Y. Liu, "Aqueous synthesis of glutathione-capped CdTe/CdS/ZnS and CdTe/CdSe/ZnS core/shell/shell nanocrystal heterostructures," *Langmuir*, vol. 28, no. 21, pp. 8205–8215, 2012.
- [113] P. W. Barone, S. Baik, D. A. Heller, and M. S. Strano, "Near-infrared optical sensors based on single-walled carbon nanotubes," *Nature Materials*, vol. 4, no. 1, pp. 86–92, 2005.
- [114] W. W. Yu, L. Qu, W. Guo, and X. Peng, "Experimental determination of the extinction coefficient of CdTe, CdSe, and CdS nanocrystals," *Chemistry of Materials*, vol. 15, no. 14, pp. 2854–2860, 2003.
- [115] B. Hua, K. Y. Han, R. Zhou, H. Kim, X. Shi, S. C. Abeysirigunawardena, A. Jain, D. Singh, V. Aggarwal, S. A. Woodson, and H. Taekjip, "An improved surface passivation method for single-molecule studies," *Nature Methods*, vol. 11, no. 12, pp. 1233–1236, 2014.
- [116] M. Gouterman, "Spectra of porphyrins," *Journal of Molecular Spectroscopy*, vol. 6, no. 1, pp. 138–163, 1961.
- [117] M. Gouterman, L. C. Snyder, and G. H. Wagniere, "Spectra of porphyrins .2. 4 orbital model," *Journal of Molecular Spectroscopy*, vol. 11, no. 2, pp. 108–127, 1963.
- [118] S. M. Nimjee, C. P. Rusconi, and B. A. Sullenger, "Aptamers: an emerging class of therapeutics," *Annual Review of Medicine*, vol. 56, no. 1, pp. 555–583, 2005.
- [119] Y. F. Li, C. R. Geyer, and D. Sen, "Recognition of anionic porphyrins by DNA aptamers," *Biochemistry*, vol. 35, no. 21, pp. 6911–6922, 1996.
- [120] K. Kaasik and C. C. Lee, "Reciprocal regulation of haem biosynthesis and the circadian clock in mammals," *Nature*, vol. 430, no. 6998, pp. 467–471, 2004.

- [121] K. M. Kadish, K. M. Smith, and R. Guilard, *The porphyrin handbook*. San Diego: Academic Press, 2000.
- [122] P. Ponka, "Cell biology of heme," *American Journal of the Medical Sciences*, vol. 318, no. 4, pp. 241–256, 1999.
- [123] W. T. Morgan, A. Smith, and P. Koskelo, "The interaction of human-serum albumin and hemopexin with porphyrins," *Biochimica Et Biophysica Acta*, vol. 624, no. 1, pp. 271–285, 1980.
- [124] R. S. Day, N. R. Pimstone, and L. Eales, "Diagnostic value of blood-plasma porphyrin methyl-ester profiles produced by quantitative TLC," *International Journal of Biochemistry*, vol. 9, no. 12, pp. 897–904, 1978.
- [125] J. Westerlund, M. Pudek, and W. E. Schreiber, "A rapid and accurate spectrofluorometric method for quantification and screening of urinary porphyrins," *Clinical Chemistry*, vol. 34, no. 2, pp. 345–351, 1988.
- [126] A. C. Deacon and G. H. Elder, "Front line tests for the investigation of suspected porphyria," *Journal of Clinical Pathology*, vol. 54, no. 7, pp. 500–507, 2001.
- [127] K. Kostarelos, A. Bianco, and M. Prato, "Promises, facts and challenges for carbon nanotubes in imaging and therapeutics," *Nature Nanotechnology*, vol. 4, no. 10, pp. 627–633, 2009.
- [128] Z. Liu, S. Tabakman, K. Welscher, and H. J. Dai, "Carbon nanotubes in biology and medicine: In vitro and in vivo detection, imaging and drug delivery," *Nano Research*, vol. 2, no. 2, pp. 85–120, 2009.
- [129] M. S. Strano, M. Zheng, A. Jagota, G. B. Onoa, D. A. Heller, P. W. Barone, and M. L. Usrey, "Understanding the nature of the DNA-assisted separation of single-walled carbon nanotubes using fluorescence and raman spectroscopy," *Nano Letters*, vol. 4, no. 4, pp. 543–550, 2004.
- [130] J. H. Choi and M. S. Strano, "Solvatochromism in single-walled carbon nanotubes," *Applied Physics Letters*, vol. 90, no. 22, p. 223114, 2007.
- [131] X. Tu, S. Manohar, A. Jagota, and M. Zheng, "DNA sequence motifs for structure-specific recognition and separation of carbon nanotubes," *Nature*, vol. 460, no. 7252, pp. 250–253, 2009.
- [132] H. M. So, K. Won, Y. H. Kim, B. K. Kim, B. H. Ryu, P. S. Na, H. Kim, and J. O. Lee, "Single-walled carbon nanotube biosensors using aptamers as molecular recognition elements," *Journal of the American Chemical Society*, vol. 127, no. 34, pp. 11 906–11 907, 2005.
- [133] H. Y. Zhang, B. A. Baker, T.-G. Cha, M. D. Sauffer, Y. J. Wu, N. Hinkson, M. A. Bork, C. M. McShane, K. S. Choi, D. R. McMillin, and J. H. Choi, "DNA oligonucleotide templated nanohybrids using electronic type sorted carbon nanotubes for light harvesting," *Advanced Materials*, vol. 24, no. 40, pp. 5447–5451, 2012.

- [134] F. D'Souza, S. K. Das, M. E. Zandler, A. S. D. Sandanayaka, and O. Ito, "Bionano donor-acceptor hybrids of porphyrin, ssDNA, and semiconductive single-wall carbon nanotubes for electron transfer via porphyrin excitation," *Journal of the American Chemical Society*, vol. 133, no. 49, pp. 19 922–19 930, 2011.
- [135] D. J. F. Chinnapen and D. Sen, "Hemin-stimulated docking of cytochrome c to a hemin-DNA aptamer complex," *Biochemistry*, vol. 41, no. 16, pp. 5202–5212, 2002.
- [136] G. S. Collier, J. M. Pratt, C. R. Dewet, and C. F. Tshabalala, "Studies on hemin in dimethyl sulfoxide-water mixtures," *Biochemical Journal*, vol. 179, no. 2, pp. 281–289, 1979.
- [137] C. Rimington, "Spectral-absorption coefficients of some porphyrins in the Soret-band region," *Biochemical Journal*, vol. 75, no. 3, pp. 620–623, 1960.
- [138] N. R. Kallenbach, R. I. Ma, and N. C. Seeman, "An immobile nucleic-acid junction constructed from oligonucleotides," *Nature*, vol. 305, no. 5937, pp. 829–831, 1983.
- [139] P. W. K. Rothmund, "Folding DNA to create nanoscale shapes and patterns," *Nature*, vol. 440, no. 7082, pp. 297–302, 2006.
- [140] Y. Ke, L. L. Ong, W. M. Shih, and P. Yin, "Three-dimensional structures self-assembled from DNA bricks," *Science*, vol. 338, no. 6111, pp. 1177–1183, 2012.
- [141] R. Penchovsky and R. R. Breaker, "Computational design and experimental validation of oligonucleotide-sensing allosteric ribozymes," *Nature Biotechnology*, vol. 23, no. 11, pp. 1424–1433, 2005.
- [142] G. Seelig, D. Soloveichik, D. Y. Zhang, and E. Winfree, "Enzyme-free nucleic acid logic circuits," *Science*, vol. 314, no. 5805, pp. 1585–1588, 2006.
- [143] M. N. Stojanovic, S. Semova, D. Kolpashchikov, J. Macdonald, C. Morgan, and D. Stefanovic, "Deoxyribozyme-based ligase logic gates and their initial circuits," *Journal of the American Chemical Society*, vol. 127, no. 19, pp. 6914–6915, 2005.
- [144] D. Y. Zhang, A. J. Turberfield, B. Yurke, and E. Winfree, "Engineering entropy-driven reactions and networks catalyzed by DNA," *Science*, vol. 318, no. 5853, pp. 1121–1125, 2007.
- [145] L. P. Feng, S. H. Park, J. H. Reif, and H. Yan, "A two-state DNA lattice switched by DNA nanoactuator," *Angewandte Chemie International Edition*, vol. 42, no. 36, pp. 4342–4346, 2003.
- [146] H. Yan, X. P. Zhang, Z. Y. Shen, and N. C. Seeman, "A robust DNA mechanical device controlled by hybridization topology," *Nature*, vol. 415, no. 6867, pp. 62–65, 2002.
- [147] B. Chakraborty, R. J. Sha, and N. C. Seeman, "A DNA-based nanomechanical device with three robust states," *Proceedings of the National Academy of Sciences of the United States of America*, vol. 105, no. 45, pp. 17 245–17 249, 2008.

- [148] J. Cheng, S. Sreelatha, R. Hou, A. Efremov, R. Liu, J. R. C. van der Maarel, and Z. Wang, "Bipedal nanowalker by pure physical mechanisms," *Physical Review Letters*, vol. 109, no. 23, p. 238104, 2012.
- [149] Y. He and D. R. Liu, "Autonomous multistep organic synthesis in a single isothermal solution mediated by a DNA walker," *Nature Nanotechnology*, vol. 5, no. 11, pp. 778–782, 2010.
- [150] T. E. Ouldridge, R. L. Hoare, A. A. Louis, J. P. K. Doye, J. Bath, and A. J. Turberfield, "Optimizing DNA nanotechnology through coarse-grained modeling: A two-footed DNA walker," *ACS Nano*, vol. 7, no. 3, pp. 2479–2490, 2013.
- [151] C. Wang, Y. Tao, G. Song, J. Ren, and X. Qu, "Speeding up a bidirectional DNA walking device," *Langmuir*, vol. 28, no. 41, pp. 14 829–14 837, 2012.
- [152] S. W. Santoro and G. F. Joyce, "Mechanism and utility of an RNA-cleaving DNA enzyme," *Biochemistry*, vol. 37, no. 38, pp. 13 330–13 342, 1998.
- [153] N. Srinivas, T. E. Ouldridge, P. Sulc, J. M. Schaeffer, B. Yurke, A. A. Louis, J. P. K. Doye, and E. Winfree, "On the biophysics and kinetics of toehold-mediated DNA strand displacement," *Nucleic Acids Research*, vol. 41, no. 22, pp. 10 641–10 658, 2013.
- [154] S. Kou, B. J. Cherayil, W. Min, B. P. English, and X. S. Xie, "Single-molecule michaelis-menten equations," *The Journal of Physical Chemistry B*, vol. 109, no. 41, pp. 19 068–19 081, 2005.
- [155] M. Schnitzer and S. Block, "Statistical kinetics of processive enzymes," *Cold Spring Harbor Symposia on Quantitative Biology*, vol. 60, no. 1, pp. 793–802, 1995.
- [156] L. P. Reynaldo, A. V. Vologodskii, B. P. Neri, and V. I. Lyamichev, "The kinetics of oligonucleotide replacements," *Journal of Molecular Biology*, vol. 297, no. 2, pp. 511–520, 2000.
- [157] S. W. Santoro and G. F. Joyce, "A general purpose RNA-cleaving DNA enzyme," *Proceedings of the National Academy of Sciences of the United States of America*, vol. 94, no. 9, pp. 4262–4266, 1997.
- [158] A. K. Brown, J. Li, C. M. B. Pavot, and Y. Lu, "A lead-dependent DNzyme with a two-step mechanism," *Biochemistry*, vol. 42, no. 23, pp. 7152–7161, 2003.
- [159] A. R. Feldman, E. K. Y. Leung, A. J. Bennet, and D. Sen, "The RNA-cleaving bipartite DNzyme is a distinctive metalloenzyme," *ChemBiochem*, vol. 7, no. 1, pp. 98–105, 2006.
- [160] D. Y. Zhang and E. Winfree, "Control of DNA strand displacement kinetics using toehold exchange," *Journal of the American Chemical Society*, vol. 131, no. 47, pp. 17 303–17 314, 2009.
- [161] M. B. Scheible, G. Pardatscher, A. Kuzyk, and F. C. Simmel, "Single molecule characterization of DNA binding and strand displacement reactions on lithographic DNA origami microarrays," *Nano Letters*, vol. 14, no. 3, pp. 1627–1633, 2014.

- [162] A. Johnson-Buck, J. Nangreave, S. Jiang, H. Yan, and N. G. Walter, "Multifactorial modulation of binding and dissociation kinetics on two-dimensional DNA nanostructures," *Nano Letters*, vol. 13, no. 6, pp. 2754–2759, 2013.
- [163] J. SantaLucia, "A unified view of polymer, dumbbell, and oligonucleotide DNA nearest-neighbor thermodynamics," *Proceedings of the National Academy of Sciences of the United States of America*, vol. 95, no. 4, pp. 1460–1465, 1998.
- [164] J. SantaLucia and D. Hicks, "The thermodynamics of DNA structural motifs," *Annual Review Biophysics and Biomolecular Structure*, vol. 33, no. 1, pp. 415–440, 2004.
- [165] J. Pan, F. Li, T.-G. Cha, H. Chen, and J. H. Choi, "Recent progress on DNA based walkers," *Current Opinion in Biotechnology*, vol. 34, pp. 56–64, 2015.
- [166] T.-G. Cha, B. A. Baker, J. Salgado, C. J. Bates, K. H. Chen, A. C. Chang, M. C. Akatay, J. H. Han, M. S. Strano, and J. H. Choi, "Understanding oligonucleotide-templated nanocrystals: growth mechanisms and surface properties," *ACS Nano*, vol. 6, no. 9, pp. 8136–8143, 2012.
- [167] J. C. F. Lam, S. O. Kwan, and Y. F. Li, "Characterization of non-8-17 sequences uncovers structurally diverse RNA-cleaving deoxyribozymes," *Molecular Biosystems*, vol. 7, no. 7, pp. 2139–2146, 2011.
- [168] D. Y. Zhang, S. X. Chen, and P. Yin, "Optimizing the specificity of nucleic acid hybridization," *Nature Chemistry*, vol. 4, no. 3, pp. 208–214, 2012.
- [169] I. G. Panyutin and P. Hsieh, "The kinetics of spontaneous DNA branch migration," *Proceedings of the National Academy of Sciences of the United States of America*, vol. 91, no. 6, pp. 2021–2025, 1994.
- [170] J. G. Duguid, V. A. Bloomfield, J. M. Benevides, and G. J. Thomas, "Raman spectroscopy of DNA-metal complexes .2. the thermal denaturation of DNA in the presence of Sr^{2+} , Ba^{2+} , Mg^{2+} , Ca^{2+} , Mn^{2+} , Co^{2+} , Ni^{2+} , and Cd^{2+} ," *Biophysical Journal*, vol. 69, no. 6, pp. 2623–2641, 1995.
- [171] R. Owczarzy, B. G. Moreira, Y. You, M. A. Behlke, and J. A. Walder, "Predicting stability of DNA duplexes in solutions containing magnesium and monovalent cations," *Biochemistry*, vol. 47, no. 19, pp. 5336–5353, 2008.
- [172] R. Owczarzy, Y. You, B. G. Moreira, J. A. Manthey, L. Huang, M. A. Behlke, and J. A. Walder, "Effects of sodium ions on DNA duplex oligomers: improved predictions of melting temperatures," *Biochemistry*, vol. 43, no. 12, pp. 3537–3554, 2004.
- [173] S.-i. Nakano, M. Fujimoto, H. Hara, and N. Sugimoto, "Nucleic acid duplex stability: influence of base composition on cation effects," *Nucleic Acids Research*, vol. 27, no. 14, pp. 2957–2965, 1999.
- [174] G. Zimmerman, L. Y. Chow, and U. J. Paik, "The photochemical isomerization of azobenzene," *Journal of the American Chemical Society*, vol. 80, no. 14, pp. 3528–3531, 1958.
- [175] M. You, F. Huang, Z. Chen, R.-W. Wang, and W. Tan, "Building a nanostructure with reversible motions using photonic energy," *ACS Nano*, vol. 6, no. 9, pp. 7935–7941, 2012.

- [176] J. A. Phillips, H. P. Liu, M. B. O'Donoghue, X. L. Xiong, R. W. Wang, M. X. You, K. Sefah, and W. H. Tan, "Using azobenzene incorporated DNA aptamers to probe molecular binding interactions," *Bioconjugate Chemistry*, vol. 22, no. 2, pp. 282–288, 2011.
- [177] Y. Liu and D. Sen, "Light-regulated catalysis by an RNA-cleaving deoxyribozyme," *Journal of Molecular Biology*, vol. 341, no. 4, pp. 887–892, 2004.
- [178] Z.-J. Tan and S.-J. Chen, "Nucleic acid helix stability: effects of salt concentration, cation valence and size, and chain length," *Biophysical Journal*, vol. 90, no. 4, pp. 1175–1190, 2006.
- [179] M. J. Schnitzer and S. M. Block, "Kinesin hydrolyses one ATP per 8-nm step," *Nature*, vol. 388, no. 6640, pp. 386–390, 1997.
- [180] C. Jung, P. Allen, and A. Ellington, "A stochastic DNA walker that traverses a microparticle surface," *Nature Nanotechnology*, vol. 11, no. 2, pp. 157–163, 2015.
- [181] Y. Yang, M. A. Goetzfried, K. Hidaka, M. You, W. Tan, H. Sugiyama, and M. Endo, "Direct visualization of walking motions of photocontrolled nanomachine on the DNA nanostructure," *Nano Letters*, vol. 15, no. 10, pp. 6672–6676, 2015.
- [182] T.-G. Cha, J. Pan, H. Chen, H. N. Robinson, X. Li, C. Mao, and J. H. Choi, "Design principles of DNA enzyme-based walkers: Translocation kinetics and photoregulation," *Journal of the American Chemical Society*, vol. 137, no. 29, pp. 9429–9437, 2015.
- [183] D. Roxbury, J. Mittal, and A. Jagota, "Molecular-basis of single-walled carbon nanotube recognition by single-stranded DNA," *Nano Letters*, vol. 12, no. 3, pp. 1464–1469, 2012.
- [184] C. Y. Khripin, N. Arnold-Medabalimi, and M. Zheng, "Molecular-crowding-induced clustering of DNA-wrapped carbon nanotubes for facile length fractionation," *ACS Nano*, vol. 5, no. 10, pp. 8258–8266, 2011.
- [185] A. D. Edelstein, M. A. Tsuchida, N. Amodaj, H. Pinkard, R. D. Vale, and N. Stuurman, "Advanced methods of microscope control using μ manager software," *Journal of Biological Methods*, vol. 1, no. 2, p. e10, 2014.
- [186] A. J. Lee, X. Wang, L. J. Carlson, J. A. Smyder, B. Loesch, X. Tu, M. Zheng, and T. D. Krauss, "Bright fluorescence from individual single-walled carbon nanotubes," *Nano Letters*, vol. 11, no. 4, pp. 1636–1640, 2011.
- [187] R. Zhang, E. Rothenberg, G. Fruhwirth, P. D. Simonson, F. Ye, I. Golding, T. Ng, W. Lopes, and P. R. Selvin, "Two-photon 3d FIONA of individual quantum dots in an aqueous environment," *Nano Letters*, vol. 11, no. 10, pp. 4074–4078, 2011.
- [188] L. Cognet, D. A. Tsyboulski, and R. B. Weisman, "Subdiffraction far-field imaging of luminescent single-walled carbon nanotubes," *Nano Letters*, vol. 8, no. 2, pp. 749–753, 2008.

- [189] P. Thevenaz, U. E. Ruttimann, and M. Unser, "A pyramid approach to sub-pixel registration based on intensity," *Image Processing, IEEE Transactions on*, vol. 7, no. 1, pp. 27–41, 1998.
- [190] M. J. Rust, M. Bates, and X. Zhuang, "Sub-diffraction-limit imaging by stochastic optical reconstruction microscopy (storm)," *Nature Methods*, vol. 3, no. 10, pp. 793–796, 2006.
- [191] D. L. Floyd, S. C. Harrison, and A. M. Van Oijen, "Analysis of kinetic intermediates in single-particle dwell-time distributions," *Biophysical Journal*, vol. 99, no. 2, pp. 360–366, 2010.
- [192] R. E. Thompson, D. R. Larson, and W. W. Webb, "Precise nanometer localization analysis for individual fluorescent probes," *Biophysical Journal*, vol. 82, no. 5, pp. 2775–2783, 2002.
- [193] M. Zheng, A. Jagota, E. D. Semke, B. A. Diner, R. S. McLean, S. R. Lustig, R. E. Richardson, and N. G. Tassi, "DNA-assisted dispersion and separation of carbon nanotubes," *Nature Materials*, vol. 2, no. 5, pp. 338–342, 2003.
- [194] E. S. Jeng, P. W. Barone, J. D. Nelson, and M. S. Strano, "Hybridization kinetics and thermodynamics of DNA adsorbed to individually dispersed single-walled carbon nanotubes," *Small*, vol. 3, no. 9, pp. 1602–1609, 2007.
- [195] N. Gal, D. Lechtman-Goldstein, and D. Weihs, "Particle tracking in living cells: a review of the mean square displacement method and beyond," *Rheologica Acta*, vol. 52, no. 5, pp. 425–443, 2013.
- [196] M. J. Saxton and K. Jacobson, "Single-particle tracking: applications to membrane dynamics," *Annual Review of Biophysics and Biomolecular Structure*, vol. 26, no. 1, pp. 373–399, 1997.
- [197] K. Ritchie, X.-Y. Shan, J. Kondo, K. Iwasawa, T. Fujiwara, and A. Kusumi, "Detection of non-Brownian diffusion in the cell membrane in single molecule tracking," *Biophysical Journal*, vol. 88, no. 3, pp. 2266–2277, 2005.
- [198] A. Caspi, R. Granek, and M. Elbaum, "Enhanced diffusion in active intracellular transport," *Physical Review Letters*, vol. 85, no. 26, pp. 5655–5658, 2000.
- [199] B. P. English, W. Min, A. M. Van Oijen, K. T. Lee, G. Luo, H. Sun, B. J. Cherayil, S. Kou, and X. S. Xie, "Ever-fluctuating single enzyme molecules: Michaelis-menten equation revisited," *Nature Chemical Biology*, vol. 2, no. 2, pp. 87–94, 2006.
- [200] K. Svoboda, P. P. Mitra, and S. M. Block, "Fluctuation analysis of motor protein movement and single enzyme kinetics," *Proceedings of the National Academy of Sciences of the United States of America*, vol. 91, no. 25, pp. 11 782–11 786, 1994.
- [201] K. J. D. Vos, A. J. Grierson, S. Ackerley, and C. C. Miller, "Role of axonal transport in neurodegenerative diseases," *Annual Review of Neuroscience*, vol. 31, no. 1, pp. 151–173, 2008.

- [202] D. E. Harris, S. S. Work, R. K. Wright, N. R. Alpert, and D. M. Warshaw, "Smooth, cardiac and skeletal muscle myosin force and motion generation assessed by cross-bridge mechanical interactions in vitro," *Journal of Muscle Research & Cell Motility*, vol. 15, no. 1, pp. 11–19, 1994.
- [203] S. Hahn, "Structure and mechanism of the RNA polymerase II transcription machinery," *Nature Structural & Molecular Biology*, vol. 11, no. 5, pp. 394–403, 2004.
- [204] K. Yehl, A. Mugler, S. Vivek, Y. Liu, Y. Zhang, M. Fan, E. R. Weeks, and K. Salaita, "High-speed DNA-based rolling motors powered by rna^h," *Nature Nanotechnology*, vol. 11, no. 2, pp. 184–190, 2016.
- [205] G. Slade, "Self-avoiding walks," *The Mathematical Intelligencer*, vol. 16, no. 1, pp. 29–35, 1994.
- [206] C. Bustamante, D. Keller, and G. Oster, "The physics of molecular motors," *Accounts of Chemical Research*, vol. 34, no. 6, pp. 412–420, 2001.
- [207] W. Wang, T.-Y. Chiang, D. Velegol, and T. E. Mallouk, "Understanding the efficiency of autonomous nano-and microscale motors," *Journal of the American Chemical Society*, vol. 135, no. 28, pp. 10 557–10 565, 2013.
- [208] K. S. Dickson, C. M. Burns, and J. P. Richardson, "Determination of the free-energy change for repair of a DNA phosphodiester bond," *Journal of Biological Chemistry*, vol. 275, no. 21, pp. 15 828–15 831, 2000.
- [209] S. M. Block, "Kinesin: What gives?" *Cell*, vol. 93, no. 1, pp. 5 – 8, 1998.
- [210] X. Qu, D. Zhu, G. Yao, S. Su, J. Chao, H. Liu, X. Zuo, L. Wang, J. Shi, L. Wang *et al.*, "An exonuclease III-powered, on-particle stochastic DNA walker," *Angewandte Chemie International Edition*, vol. 56, no. 7, pp. 1855–1858, 2017.
- [211] R. D. Vale, "The molecular motor toolbox for intracellular transport," *Cell*, vol. 112, no. 4, pp. 467 – 480, 2003.

VITA

VITA

Jing Pan obtained bachelor's degree on energy and power engineering from Xi'an Jiaotong University (China). He earned his Ph.D from the School of Mechanical Engineering at Purdue University in Dr. Jong Hyun Choi's lab. His research focuses on developing synthetic molecular machines using DNA nanotechnology. He has published 10+ papers in peer-reviewed journals including *Nature Nanotechnology* and *Science Advances*. His work has received broad media coverage. Jing Pan has received multiples scholarships and awards, including the highest graduate honor at Xi'an Jiaotong University and Chinese Government Award for Outstanding Students Abroad.

PUBLICATIONS

Journal Papers

1. Pan, J.; Cha, T.-G.; Li, F.; Chen, H.; Bragg, N. A.; Choi, J. H. Visible/Near-Infrared Subdiffraction Imaging Reveals the Stochastic Nature of DNA Walkers. *Science Advances* 2017, *3*, e1601600.
2. Pan, J.; Li, F.; Choi, J.H. Single-Wall Carbon Nanotubes as Optical Probes for Bio-Sensing and Imaging. *Journal of Materials Chemistry B* 2017, *5*, 6511–6522 .
3. Li, F.; Cha, T.-G.; Pan, J.; Ozcelikkale, A.; Han, B.; Choi, J. H. DNA Walker-Regulated Cancer Cell Growth Inhibition. *ChemBioChem* 2016, *17*, 1138–1141.
4. Chen, H.; Zhang, H.; Pan, J.; Cha, T.-G.; Li, S.; Andr  sson, J.; Choi, J. H. Dynamic and Progressive Control of DNA Origami Conformation by Modulating DNA Helicity with Chemical Adducts. *ACS Nano* 2016, *10*, 4989–4996.
5. Li, F.; Chen, H.; Pan, J.; Cha, T.-G.; Medintz, I. L.; Choi, J. H. A DNzyme-Mediated Logic Gate for Programming Molecular Capture and Release on DNA Origami. *Chemical Communications* 2016, *52*, 8369–8372.
6. Pan, J.; Li, F.; Cha, T.-G.; Chen, H.; Choi, J. H. Recent Progress on DNA Based Walkers. *Current Opinion in Biotechnology* 2015, *34*, 56–64.
7. Pan, J.*; Cha, T.-G.*; Chen, H.; Robinson, H. N.; Li, X.; Mao, C.; Choi, J. H. Design Principles of DNA Enzyme-Based Walkers: Translocation Kinetics and Photoregulation. *Journal of the American Chemical Society* 2015, *137*, 9429–9437. (*Equal contribution)
8. Zhang, H.; Pan, J.; Ghimire, S.; Bork, M. A.; Riccitelli, M. M.; McMillin, D. R.; Choi, J. H. Regeneration of Light-Harvesting Complexes via Dynamic Replacement

- of Photodegraded Chromophores. *ACS Applied Materials & Interfaces* 2015, 7, 7833–7837.
9. Kang, Z.; Yan, X.; Zhang, Y.; Pan, J.; Shi, J.; Zhang, X.; Liu, Y.; Choi, J. H.; Porterfield, D. M. Single-Stranded DNA Functionalized Single-Walled Carbon Nanotubes for Microbiosensors via Layer-by-Layer Electrostatic Self-Assembly. *ACS Applied Materials & Interfaces* 2014, 6, 3784–3789.
 10. Cha, T.-G.; Pan, J.; Chen, H.; Salgado, J.; Li, X.; Mao, C.; Choi, J. H. A Synthetic DNA Motor That Transports Nanoparticles Along Carbon Nanotubes. *Nature Nanotechnology* 2014, 9, 39–43.
 11. Chen, H.; Cha, T.-G.; Pan, J.; Choi, J. H. Hierarchically Assembled DNA Origami Tubules with Reconfigurable Chirality. *Nanotechnology* 2013, 24, 435601.
 12. Pan, J.; Zhang, H.; Cha, T.-G.; Chen, H.; Choi, J. H. Multiplexed Optical Detection of Plasma Porphyrins Using DNA Aptamer-Functionalized Carbon Nanotubes. *Analytical Chemistry* 2013, 85, 8391–8396.

Book Chapters

1. Pan, J.; Cha, T.-G.; Chen, H.; Li, F.; Choi, J. H. DNA Walkers as Transport Vehicles of Nanoparticles Along a Carbon Nanotube Track. *3D DNA Nanostructure: Methods and Protocols* 2017, 269–280.
2. Pan, J.; Cha, T.-G.; Chen, H.; Choi, J. H. Carbon nanotube-based optical platforms for biomolecular detection. *Carbon Nanotubes and Graphene for Photonic Applications*; Yamashita, S.; Saito, Y.; Choi, J. H., Eds.; Elsevier Inc, 2013.